A STUDY OF BLISTER TESTS FOR FILM ADHESION MEASUREMENT AND FRACTURE EFFICIENCY OF TESTS FOR ADHESIVE BONDS

by

Yeh-Hung Lai

Dissertation submitted to the Faculty of the

Virginia Polytechnic Institute and State University

in partial fulfillment of the requirements for the degree of

DOCTOR OF PHILOSOPHY

in

Engineering Mechanics

APPROVED:

David A Dillard

D. A. Dillard, Chairman

Siegfried Holzer

S. M. Holzer

C. W. Smith

Layne T. Watson

L. T. Watson

James Wightman

J. P. Wightman

April, 1994

Blacksburg, Virginia

A Study of Blister Tests for Film Adhesion Measurement and Fracture Efficiency of Tests for Adhesive Bonds

by

Yeh-Hung Lai

Committee Chairman: David A Dillard

Department of Engineering Science and Mechanics

Abstract

A novel concept, the fracture efficiency, is proposed in this dissertation as a performance index of fracture specimen designs for adhesive bonds. Evaluated based on a simple quantity, the fracture efficiency parameter, the fracture efficiency represents how much crack driving force a certain specimen design can produce along the bondline for a given maximum non-singular stress in the adherends. In this dissertation, a study of membrane peeling specimens shows that various existing test geometries have little difference in the fracture efficiency. Furthermore, the study shows that it is unlikely to develop new membrane peeling tests with high fracture efficiency. Therefore, gross inelastic energy dissipation in the film specimen may occur when using the membrane peeling tests, and may result in large errors in the film adhesion measurement when only elastic material response is considered in the analysis. As a result, the use of a backing material for film adhesion measurement is suggested because of the significant increase in the fracture efficiency when a proper backing material is used. Besides the use as one of the guidelines for fracture specimen designs, it is also demonstrated in this dissertation that the fracture efficiency parameter can also be used to help one determine the validity of a measured bond fracture strength.

The study of fracture efficiency leads to new analyses of several existing fracture test geometries, and contributes to a better understanding of the standard blister, island

blister, peninsula blister, peel, and cracked lap shear tests. It is found that the island blister and peninsula blister tests can produce very high energy release rates at low pressures by using a small island radius or a small peninsula width. However, these so called "high energy release rate" tests also induce localized high stress concentrations near the debond front and therefore, yielding or rupturing may still unavoidable in such specimens. The significant localized inelastic effect on the measurement of the bond fracture strength is also demonstrated in the peninsula blister experiment for an adhesive tape specimen subjected to a relatively low pressure load. Another important conclusion drawn from the analyses of various membrane peeling tests is that the existing membrane blister tests are special cases of the peel test if compared very near the debond front.

Besides analyses for membrane peeling specimens, this dissertation also reports a new closed form solution for the cracked lap shear specimen using a geometrically nonlinear beam-column approach. Excellent agreement for energy release rates has been shown between the closed form solution and geometrically nonlinear finite element analyses. The study also discusses how to design a cracked lap shear specimen of constant energy release rate and high fracture efficiency.

Table of Contents

List of Figures

List of Tables

Acknowledgments

I would like to express my sincere gratitude to Prof. Dave Dillard, who as advisor, offered his continual guidance and support in both technical contributions of this dissertation and my professional development. His patience and encouragement during the difficult time before the start of this dissertation topic are greatly appreciated.

I would also like to thank my advisory committee members, Professor C. W. Smith, Professor J. P. Wightman, Professor, S. M. Holzer, and Professor L. T. Watson, for their valuable comments.

In addition, I wish to acknowledge:

- the financial support of National Science Foundation's Science and Technology Center on High Performance Polymeric Adhesives and Composites, Center for Adhesive and Sealant Science, and ALCOA Foundation.
- the valuable comments Dr. Brian Love made.
- my colleagues in the ESM adhesion science group, Dr. Yeou-Shin Chang, Dr. Greg Anderson, Dwayne Rakestraw, Hari Parvatareddy, Tsouno Chang, Jack Lesko, Mark Taylor, Paige Clifton, and Bao Yong for their help, and most importantly, their friendship over the years. Among them, Tsouno's help on metal polishing and Dwayne's help on the cracked lap shear tests deserve special thanks.
- the staff of the Center for Adhesive and Sealant Science, Virginia, Katy, and Kim for their help.
- the staff of the Material Response Group, Sheila, Paula, and Melba.

Finally, my family deserve special acknowledgments. My beloved wife, Hsiaohsi, is greatly appreciated for her consistent encouragement, understanding , patience, and love

throughout my doctoral study. I would also like to thank my parents for their inspiration and support. Two new family members, Brian and Kelly, who joined this family at the time when this research topic started, are also appreciated for the joy they brought. They made this two-year period especially wonderful.

Chapter 1. Introduction

1.1 Motivations and Objectives

Over the years, a large number of test geometries have been devised for evaluating the strength of adhesive bonds failing in the adhesive or along the interface. The use of fracture mechanics has provided a rational basis for design of adhesive joints and evaluation of bond fracture strength. One important characteristic in these tests is the ability to debond the specimen without causing rupture or gross yielding in the adherends. Among the various material systems, film adhesion measurement especially requires tests that are capable of producing high energy release rates at relatively low stresses in the films and coatings, since most films and coatings have relatively strong adhesion and low load bearing capacity due to the small thickness. (A film has a thickness smaller than 0.25mm (Brinson, 1990). A coating has a thickness larger than 0.25mm (Mittal, 1978).) Many tests have been developed to measure the bond fracture strength of films and coatings over the years. Although some of them claim to have the property of high energy release rates, careful examination reveals that these claims are not supported by rigorous analysis. The original motivation of the current study was to investigate whether high energy release rates could be obtained by changing the test geometries so that failure in the films, primarily by gross yielding and rupturing, could be prevented.

Specific objectives are as follows:

(1) To propose and investigate a novel concept, the fracture efficiency, to evaluate the performance of fracture specimen designs for adhesive bonds.

(2) To analyze several existing fracture test geometries and study their fracture efficiencies.

(3) To design and construct an improved experimental setup and procedure for the peninsula blister test.

1.2 Fracture Tests for Measuring Bond Fracture Strength

Over the years, the specimens that have been devised for measuring the strength of adhesive bonds based on the fracture mechanics can be grouped into three categories: laminated beam specimens, peel and blister specimens, and miscellaneous specimens. These specimens will be described briefly in the following sections.

Laminated Beam Specimens

Laminated beam specimens are the simplest of the three categories and provide a wide range of fracture mode mixity by applying different loading conditions and using different adherend thickness ratios. This category as shown in Fig 1.1 includes the double cantilever beam (DCB), tapered DCB, mode III DCB, mixed mode I-III DCB, wedge DCB, end notched flexure, end notched cantilever, mixed mode flexure, cracked lap shear, four point bend specimens, and double torsion specimens. It should be noted that the mode mixity in the laminated beam specimens is often assessed based on the assumption that the bondline is much thinner or less stiffer than the adherends, so that the adhesive layer can be ignored. Therefore, the mode mixity of a laminated beam specimen mentioned in the literature is a "far field" quantity, not a "near field" quantity. The relationship between the far field and near field mode mixity has been studied by Suo and Hutchinson (1989) and Fleck *et al.* (1991).

The double cantilever beam specimen, perhaps the simplest and most used beam specimen, was first introduced for fracture toughness testing of adhesives by Ripling and

Mostovoy (1975). Although the DCB specimen is most often used as a mode I fracture specimen by using the same thickness and material in both adherends, this specimen can produce a surprisingly wide range of mode mixity by changing the bending stiffnesses of the adherends (Mangalgiri *et al.*, 1987; Fig. 1.1(a)), the loading conditions (Chai, H, 1988; Fig. 1.1(b)), or orienting the crack plane to the direction of the applied load (Ripling *et al.*, 1988; Fig. 1.1(c)). When loaded by a fixed displacement using a wedge instead of a fixed load at the ends of the adherends, the configuration is known as a wedge test and is useful for measuring environmental assisted crack growth (McMillan, 1981; Fig. 1.1(d)). Alternatively, one could maintain a constant displacement with a load frame for the same purpose. When energy release rates independent of crack length are preferred, one could apply pure bending moments at the ends of adherends (Osborne, 1966; Fig. 1.1(e)) or taper the adherend thicknesses or widths (Ripling and Mostovoy, 1975; Fig. 1.1(f)) to obtain the so called "constant energy release rate tests". A novel loading arrangement was recently proposed by Dillard *et al.* (1993) to permit nearly constant energy release rate testing of untapered double cantilever beam specimens.

The specimens mentioned in the previous paragraph are subjected to loads at the ends of the adherends. If one applies a three point bend load to the DCB specimen instead of an end load (Fig. 1.1(g)), the mode II fracture resistance can be obtained. The specimen is called the "end notched flexure specimen" and has been used in composite materials (Russell and Street, 1982 and 1985) and structural adhesives (Ripling *et al.*, 1971; Mall and Kochar, 1986; Chai and Mall, 1988) research. Mode II loading can also be obtained by applying a shear load (Fig. 1.1(h)) at one end and clamping the other (Russell and Street, 1987; Moussiaux *et al.*, 1987). The specimen is called the end notched cantilever beam specimen. If the three point bending configuration is modified so that one of the reactions is moved to the other adherend as seen is Fig. 1.1(i), the specimen becomes the mixed mode flexure (MMF) specimen with fracture in mode I and mode II (Russell and Street, 1985; Chai and Mall, 1988). If loaded axially instead of transversely, the specimen becomes a cracked lap shear (CLS; Fig. 1.1(j)) specimen which

has a mode II dominant mixture. After the specimen was proposed by Brussat and Chiu (1978), it has been used extensively (Mall *et al.*, 1984; John and Mall, 1985; Mall *et al.*, 1987; Mall and Yun, 1987). If the specimen is sufficiently long, constant energy release rates can be obtained over a portion of the specimen. It has been found that the results are rather sensitive to how the boundary conditions are interpreted (Everett and Johnson, 1985; Lin and Liechti, 1987). To properly determine the mode mixity and the energy release rate, geometrical nonlinearity of the specimen should be considered (Johnson, 1987). A constant mixed mode energy release rate can also be obtained through a four point bend configuration as shown in Fig. 1.1(k) (Charalambides *et al.*, 1989). To obtain mode I constant energy release rates, one may also use the double torsion specimen as shown in Fig. 1.1(l). Strictly speaking, the double torsion specimen is not a beam type specimen, since there is no bending moment or axial force in the specimen. However, since one can not distinguish it from the rest of the laminated beam specimens from its appearance except for the loading conditions, it may as well be categorized as one member of the laminated beam specimens. It is the torsional loading condition of the double torsion specimen that makes it unique among laminated beam specimens (Outwater and Gerry, 1969; Cho and Gent, 1985; and Gent, 1987).

Peel and Blister Specimens

The peel and blister specimens are useful for films or flexible adherends. These specimens generally involve the mechanism of "peeling" one adherend from the substrate. Both peel and blister specimens have variations shown in Figs.1.2 and 1.3.

The most general configuration of the peel specimen is shown in Fig. 1.2(a), which involves a force (peel force) applied at an arbitrary angle (peel angle). The test geometry is unique in that the load and peel angle are controlled independently. Several ASTM (American Society for Testing and Materials) standard peel tests have been established, which include the T-peel test (Fig. 1.2 (b), ASTM D1876-72), the floating roller peel

resistant test (Fig. 1.2(c), ASTM D3167-73T), and the 180° peel test (Fig. 1.2(d), ASTM D903-49). The T-peel test is useful for studying adhesion between flexible adherends. The floating roller peel setup offers a convenient way to maintain constant peel angle and a constant curvature in the peeled strip. The setup is useful in that it can be gripped in a conventional tensile load frame. The 180° peel test is easy to perform provided that one of the adherends is flexible enough so that it can essentially be folded back on itself. Other variations of peel tests include the symmetric peel test (Fig. 1.2(e), Gent and Hamed, 1977) and the pull-off test (Fig. 1.2(f), Gent and Kaang, 1986; Gent, 1987). The symmetrical arrangement of the symmetric peel test is designed to adjust the degree of bending of the peeled strips by varying the distance between applied load and the substrates. The pull-off test is useful for adhesion measurement of adhesive tapes. Although a small pull-off angle was assumed in the derivation of the energy release rate, it was found that a pull-off angle of up to 25° produced good agreement between the theoretical analysis and experiments (Gent, 1987).

Blister specimens consist of a layer of material adhering or bonded to the substrate except for the initial debonded portion where loading is applied. The load is often applied by pressure loading. Because of the pressure loading which eliminates the mechanical contact between the grips and the specimens, the blister specimens are useful for delaminating films and coatings. The blister test was originally proposed by Dannenberg (1961) for measuring the adhesion of coatings (Fig. 1.3(a)). The thickness of the blister can range from very thin (membranes; Gent and Lewandowski, 1987; Jeong, 1992; Allen and Senturia, 1988 and 1989; Lai and Dillard, 1993) to moderate (plates; Williams *et al.*, 1955, 1958, 1969, 1970, 1972, 1978; Updike, 1976; Lai and Dillard, 1990a and 1990b; Dillard and Bao, 1991) to very thick (semi-infinite medium; Mossakovskii and Rybka, 1964). Blister specimens are quite versatile and have been used in a number of configurations. The standard blister (Fig. 1-3(b)) is quite compatible with environmental exposures because the pressurizing medium is contained within the blister region. For circular versions of the blister specimen, the axisymmetric shape minimizes problems

associated with edge effects of finite width specimens, and diffusion perpendicular to the debond front eliminates spurious effects from environmental exposure. One of the disadvantages with the standard blister is that the energy release rate increases with the debond radius, thus making accurate evaluation of the debond radius essential and resulting in an unstable fracture specimen. To minimize this problem, the constrained blister was introduced (Fig. 1.3(c)). The test geometry was proposed by Dillard and Chang (1987), Chang, Lai and Dillard (1989), and independently by Napolitano *et al.* (1988), and analyzed by Lai and Dillard (1990a, 1990b). While the constrained blister specimen is a constant energy release rate specimen only under limiting cases, it does significantly reduce the dependence of the energy release rate on debond radius. For durability studies, one may also use the strip blister specimen (Fig. 1.3(d)) proposed by Dillard et al (1988). Similar to the Boeing wedge test in the laminated beam specimen category, the strip blister specimen is loaded under a constant displacement, although other loading scenarios are possible and applications other than determining the durability are possible.

To obtain a high energy release rate at relatively low pressure, the island blister (Fig. 1.3(e)) was proposed by Allen and Senturia (1988, 1989) for measuring the adhesion of polyimide films. Allen and Senturia reported that the island blister geometry was successfully employed to debond prestressed polyimide films, while the standard blister geometry resulted in film rupture of similar bonds. Although the island blister test is capable of producing high energy release rates, the debonding process is unstable. To have a stable debonding process while retaining the advantage of the high energy release rate, the peninsula blister (Fig. 1.3(f)) was introduced by Dillard *et al.*, (1990, 1991). Energy release rates for both membrane and plate solutions were derived, indicating that the test geometry of this specimen results in a truly constant energy release rate over a relatively large test section. Both the peninsula and the island blister specimens derive a high energy release rate from the fact that the debond front is confined to a very small

length. A moderate increase in compliance is produced by a relatively small increase in debond area, thereby causing large energy release rates at relatively low pressure.

Miscellaneous Specimens

The fracture test specimens that do not belong to the previous two categories are grouped together as miscellaneous specimens, which include compact tension, compact shear, cone, and Brazil nut sandwich specimens as shown in Fig. 1.4.

Although the compact tension and compact shear specimens (Figs. 1.4(a) and 1.4(b)) are not as widely used as the laminated beam specimens, they have some advantages such as the minimized use of adhesive due to the compact geometry and wide range of mode mixity from a single specimen when subjected to biaxial loading (Mai and Vipond, 1978; Anandarajah and Vardy, 1984; Arah *et al.*, 1989).

The cone test specimen consists of a conical plug bonded to a conical hole, as shown in Fig. 1.4(c). The geometry is capable of producing various amounts of mode I, II, and III components by applying tensile or torsional loads with different cone angles (Anderson *et al.*, 1977).

The Brazil nut sandwich specimen was proposed by Wang and Suo (1990) as shown in Fig. 1.4(d). The specimen is capable of producing various mode mixity by changing the compression angle, θ. The specimen allows one to generate sizable toughness data with a small amount of specimen and is especially useful for brittle materials.

1.3 Overview of Dissertation

Chapter 2 of this dissertation will discuss the membrane solutions for the standard and island blister geometries. The stress distributions, displacements, and energy release rates will be discussed. The effects of the prestress will also be investigated. Chapter 3 will discuss the derivation and results of the energy release rate for the peninsula blister

specimen. The comparison of the peninsula, island, and standard blister specimens will be made. Chapter 4 will compare the peel test with one of its variations and several blister tests. Specific attention will be focused on the mechanisms of "peeling" of films and coatings near the debond front for membrane peeling tests of different geometries subjected to various loading conditions. Chapter 5 will propose a new quantity - the fracture efficiency parameter. This parameter will then be used to compare the "fracture efficiency" of various test geometries. The limitations of membrane peeling tests for films and coatings will be discussed. In Chapter 6, a closed form solution for energy release rates based on a beam-column nonlinear analysis for the cracked lap shear specimen will be derived and discussed. The results from the analytical and finite element analyses will be compared. The closed form solution will also be used to explain anomalous fatigue test results using the cracked lap shear specimen. Chapter 7 will discuss experimental aspects of blister tests. The bond fracture strength of adhesive tape will be measured using the peninsula blister test. Finally, the conclusions which can be drawn from this dissertation will be presented in Chapter 8. Appendix A will list the expressions for unknown coefficients in the solution of the cracked lap shear problem. Appendix B will tabulate the finite element result for some cracked lap shear specimens found in the literature. Appendix C will discuss a proposed experimental technique to determine the bond fracture strength of films and coatings by accounting for the plastic and viscoelastic effects. In Appendix D, a metal polishing technique will be proposed to fabricate the blister and peel specimens for thin polymeric films on aluminum substrates. Appendix E will have a detailed description of the experimental setup and testing procedure for the peninsula blister test. Appendix F will propose a simple procedure to measure the Young's modulus and prestress in films and coatings using the peninsula blister fixture.

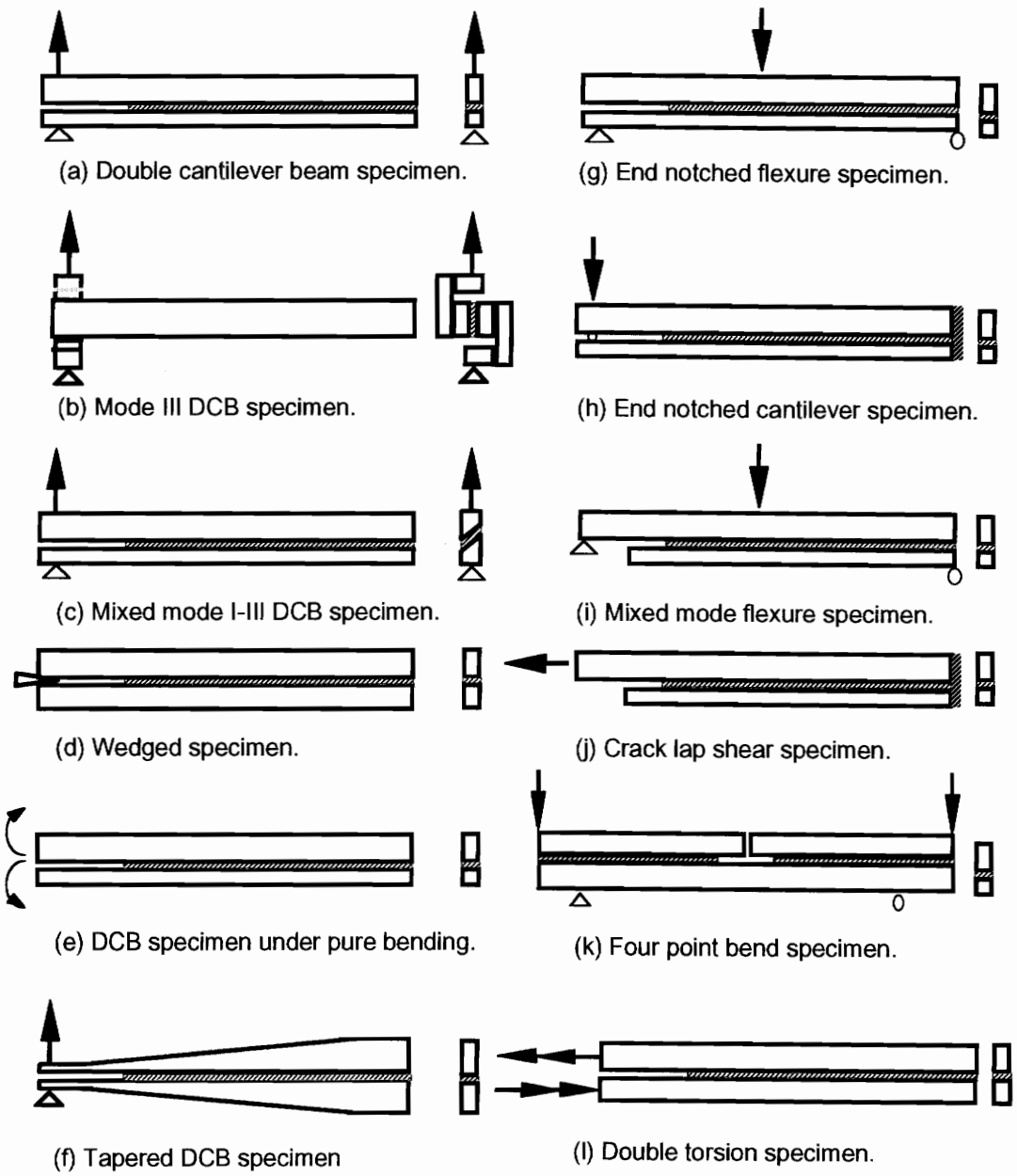

Figure 1.1 Illustrations of various laminated beam specimens.

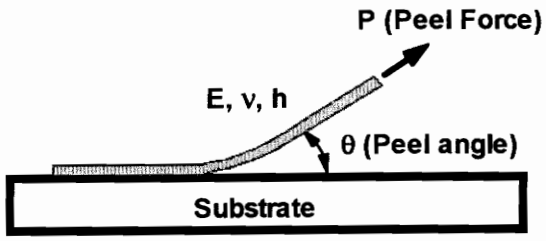

(a) Peel test.

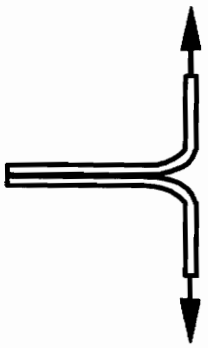

(b) T-peel test.

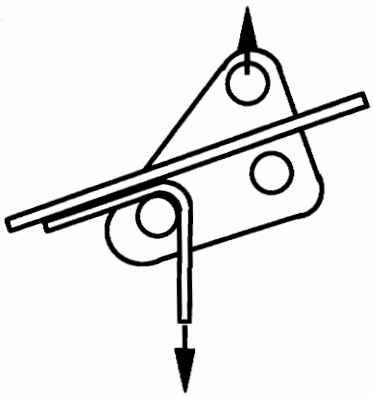

(c) Floating roller peel resistant test.

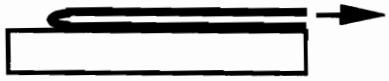

(d) 180° peel test.

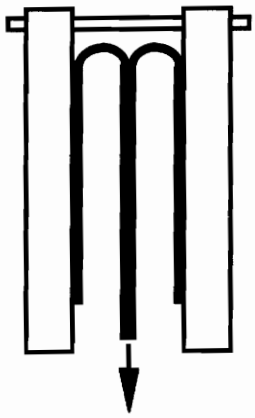

(e) Symmetrical peel test.

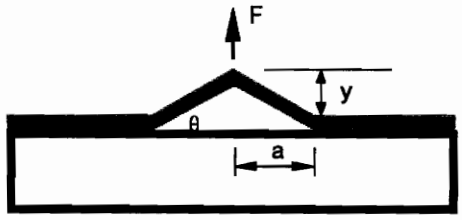

(f) Pull-off test.

Figure 1.2 Illustrations of various peel tests and variations.

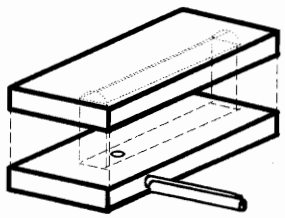

(a) Dannenberg's blister specimen.

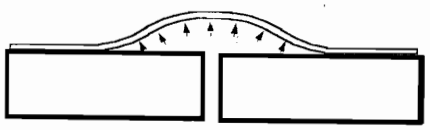

(b) Standard blister specimen.

(c) Constrained blister specimen.

(d) Strip blister specimen.

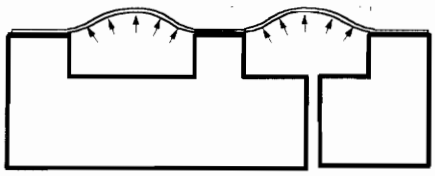

(e) Island blister specimen.

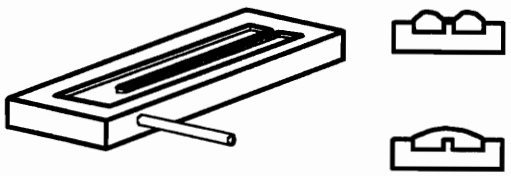

(f) Peninsula blister specimen.

Figure 1.3 Illustrations of various blister specimens.

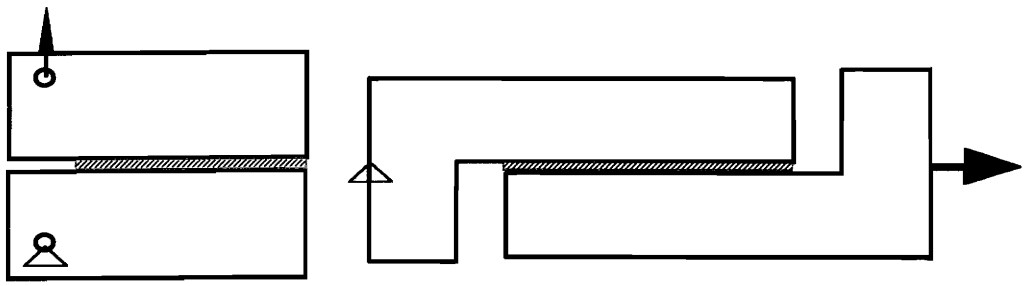

(a) Compact tension specimen.

(a) Compact shear specimen.

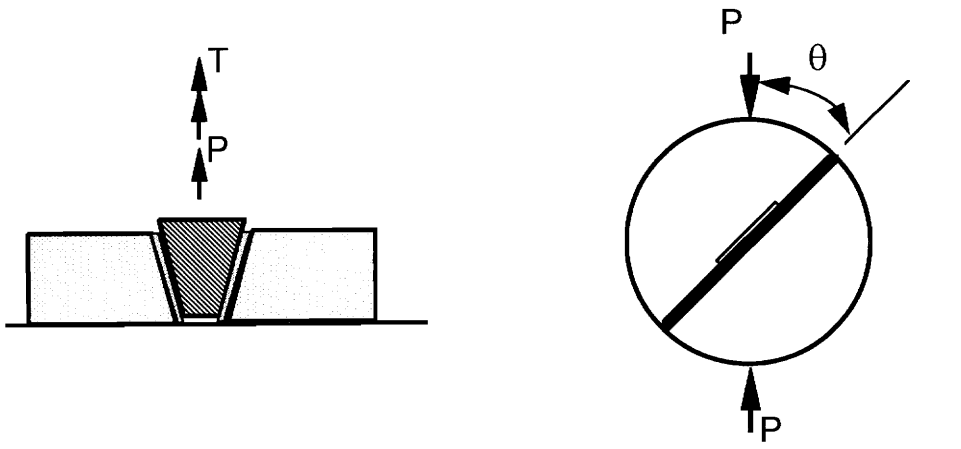

(c) Cone test.

(d) Brazil nut sandwiches specimen.

Figure 1.4 Illustrations of several miscellaneous specimens.

Chapter 2. Membrane Solutions for Circular Blister

2.1 Introduction

The blister test was originally proposed by Dannenberg (1961) for measuring the adhesion of coatings. To have better control over the debond growth, he confined the blister to form in a narrow groove, thereby resulting in a constant energy release rate specimen. Williams (1969) used a circular debond to measure the fracture energy of elastomeric materials adhesively bonded to a rigid substrate. Plate solutions for blister geometry have been analyzed by many, including Williams *et al.* (1955, 1958, 1970, 1972, 1978) and Updike (1976). Blister tests have been applied to a wide variety of adhesive systems, including paints, coatings (Dannenberg, 1961), bonded plates (Fernando and Kinloch, 1990), pressure sensitive adhesive tapes (Gent and Lewandowski, 1987), elastomer (Lotfipour *et al.*, 1991), polymer-polymer adhesion (Chu and During, 1992), polyimide to silicone (Jeong, 1992), and even adhesion to ice (Jiang and Penn, 1990). Blister specimens are quite versatile and have been applied in a number of configurations. The standard blister (Fig. 2-1) is quite compatible with environmental exposures because the pressurizing medium is contained within the blister region. For circular versions of the blister specimen, the axisymmetric shape minimizes problems associated with edge effects of finite width specimens, and diffusion perpendicular to the debond front eliminates spurious effects for environmental exposure. One of the disadvantages with the standard blister is that the energy release rate increases with the debond radius, thus making accurate evaluation of the debond radius essential and resulting in an unstable fracture specimen. To minimize this problem, the constrained blister was introduced (Fig. 2-2). The test geometry was proposed by Dillard and Chang (1987) and independently by

Napolitano *et al.*(1988) and analyzed by Lai and Dillard (1990a, 1990b). While the constrained blister is a constant energy release rate specimen only under limiting cases, it does significantly reduce the dependence of the energy release rate on debond radius.

To obtain a high energy release rate at relatively low pressure, the island blister (Fig. 2-3) was proposed by Allen and Senturia (1988, 1989) for measuring adhesion of polyimide films. Allen and Senturia reported that the island blister geometry was successfully employed to debond prestressed polyimide films, while the standard blister test geometry resulted in film rupture of similar bonds. Although the island blister test is capable of producing high energy release rates, the debonding process is unstable. To have a stable debonding process while retaining the advantage of a high energy release rate, the peninsula blister (Fig. 2-4) was introduced by Dillard *et al.* (1990, 1991). Energy release rates for both membrane and plate solutions were derived, indicating that the test geometry of this specimen results in a truly constant energy release rate over a relatively large test section. Both the peninsula and the island blister specimens derive high energy release rates from the fact that the debond front is confined to a very small length. A moderate increase in compliance is produced by a relatively small increase in debond area, thereby causing large energy release rates.

Because the two geometries were able to produce high energy release rates at low pressures, they were characterized as "high energy release rate" tests. However, since one can always apply high loads to obtain high energy release rates for a given test geometry, whether a certain test geometry has the high energy release rate property should not be judged based on the basis of the magnitude of the applied load. Instead, a true high energy release rate test should be one that is capable of producing high energy release rates at low adherend stresses so that the test geometry is able to debond the specimen without causing gross yielding or even rupturing in the adherends. This should apparently be the criterion for a more efficient fracture test geometry.

In recent years, two circular versions of the blister geometries, the standard and island blisters, have received increasing attention due to their applications for film adhesion measurement. In spite of the increasing use of these two blister geometries for films and coatings, solutions for energy release rates exist only for some simple cases, such as no-prestress solutions for the standard blister (Gent and Lewandowski, 1987) and prestress dominant solutions for the island blister (Allen and Senturia, 1988, 1989).

In this chapter, the membrane solutions for the standard and island blister geometries will be derived. The membrane is assumed to be homogeneous, isotropic and linear elastic. An arbitrary magnitude of prestress will be considered. The ranges where no-prestress and dominant prestress solutions are applicable will be identified. Based on the data from the above solution, an approximate solution of energy release rate for the standard blister will be proposed and discussed.

2.2 Mathematical Formulations and Solutions for Circular Blisters

For a circular membrane of which the cross section is shown in Fig. 2.5, the constitutive equations at the middle surface are (Kao, 1971):

$$N_r = \frac{Eh}{(1-\nu^2)}(\bar{\varepsilon}_r + \nu\bar{\varepsilon}_\theta) + \bar{\sigma}_0 h, \tag{2.1-1}$$

$$N_\theta = \frac{Eh}{(1-\nu^2)}(\bar{\varepsilon}_\theta + \nu\bar{\varepsilon}_r) + \bar{\sigma}_0 h, \tag{2.1-2}$$

where $\bar{\sigma}_0$ is the prestress in the membrane,

N_r is the meridian stress resultant,

N_θ is the circumferential stress resultant,

h is the thickness of the membrane,

$\bar{\varepsilon}_r$ is the meridian strain,

$\bar{\varepsilon}_\theta$ is the circumferential strain,

E is the Young's modulus of the membrane,

and ν is the Poisson's ratio of the membrane.

It should be noted that N_r and ε_r are not the radial stress resultant and radial strain, but rather are allowed to rotate with the middle surface. The prestress may arise during the curing process due to a mismatch of thermal expansion coefficient, shrinkage due to cure reaction, moisture or solvent induced swelling of film, etc.

The meridian strain is given by the following relation in terms of the displacements:

$$\begin{aligned}\bar{\varepsilon}_r &= \sqrt{(1+\frac{d\bar{u}}{dr})^2+\left(\frac{d\bar{w}}{dr}\right)^2}-1 \\ &= \frac{d\bar{u}}{dr}+\frac{1}{2}\left(\frac{d\bar{w}}{dr}\right)^2-\frac{1}{2}\left(\frac{d\bar{u}}{dr}\right)^2-\frac{d\bar{u}}{dr}\left(\frac{d\bar{w}}{dr}\right)^2-\left(\frac{d\bar{u}}{dr}\right)^3+...\end{aligned} \tag{2.2}$$

Assuming $\frac{d\bar{u}}{dr}$ and $\frac{d\bar{w}}{dr}$ are small and $\left(\frac{d\bar{u}}{dr}\right)^2 << \left(\frac{d\bar{w}}{dr}\right)^2$, we have

$$\bar{\varepsilon}_r \approx \frac{d\bar{u}}{dr}+\frac{1}{2}\left(\frac{d\bar{w}}{dr}\right)^2. \tag{2.3}$$

The circumferencial strain is simply

$$\bar{\varepsilon}_\theta = \frac{\bar{u}+r}{r}-1=\frac{\bar{u}}{r}, \tag{2.4}$$

where $\bar{u}$ and $\bar{w}$ are the displacement of a point at the middle surface of the membrane in the radial and the out of plane directions, respectively.

Equilibrium equations in the meridian direction and transverse direction are

$$(rN_r)_{,r} = N_\theta, \tag{2.5-1}$$

and

$$\frac{1}{r}(rN_r\bar{w}_{,r})+p=0, \tag{2.5-2}$$

where the comma denotes partial differentiation with respect to the indices which follow.

Substituting the equations for strain/displacement relations, Eqs. (2.3) and (2.4), into the constitutive equations, Eqs. (2.1), and then into the equilibrium equations, Eqs.(2.5), we can obtain the governing equations for a circular membrane as

$$3\overline{w}_{,rr}\,\overline{w}_{,r}^{2}+\frac{\overline{w}_{,r}^{3}}{r}+2\overline{w}_{,rr}\left(\overline{u}_{,r}+\nu\frac{\overline{u}}{r}+\frac{1-\nu^{2}}{E}\overline{\sigma}_{0}\right)+2\overline{w}_{,r}\left(\overline{u}_{,rr}+\frac{\overline{u}_{,r}}{r}(1+\nu)+\frac{1-\nu^{2}}{E}\frac{\overline{\sigma}_{0}}{r}\right)+2\frac{1-\nu^{2}}{Eh}p=0, \tag{2.6-1}$$

$$\overline{u}_{,rr}+\frac{\overline{u}_{,r}}{r}-\frac{\overline{u}}{r^{2}}+\overline{w}_{,r}\,\overline{w}_{,rr}+\frac{1-\nu}{2}\frac{\overline{w}_{,r}^{2}}{r}=0. \tag{2.6-2}$$

By introducing the nondimensional variables, x, w, u, σ_0, σ_r, and σ_θ, defined as

$$x=\frac{r}{R}, \tag{2.7-1}$$

$$w=\frac{\overline{w}}{R}\left(\frac{pR}{Eh}\right)^{-1/3}, \tag{2.7-2}$$

$$u=\frac{\overline{u}}{R}\left(\frac{pR}{Eh}\right)^{-2/3}, \tag{2.7-3}$$

$$\sigma_0=\frac{\overline{\sigma}_0}{E}\left(\frac{pR}{Eh}\right)^{-2/3}, \tag{2.7-4}$$

$$\sigma_r=\frac{\overline{\sigma}_r}{E}\left(\frac{pR}{Eh}\right)^{-2/3}, \tag{2.7-5}$$

and

$$\sigma_\theta=\frac{\overline{\sigma}_\theta}{E}\left(\frac{pR}{Eh}\right)^{-2/3}, \tag{2.7-6}$$

Eqs. (2.6) can be rewritten as

$$3w_{,xx}\,w_{,x}^{2}+\frac{w_{,x}^{3}}{x}+2w_{,xx}\left(u_{,x}+\nu\frac{u}{x}+(1-\nu^{2})\sigma_0\right)+2w_{,x}\left(u_{,xx}+\frac{u_{,x}}{x}(1+\nu)+(1-\nu^{2})\frac{\sigma_0}{x}\right)+2(1-\nu^{2})=0, \tag{2.8-1}$$

$$u_{,xx} + \frac{u_{,x}}{x} - \frac{u}{x^2} + w_{,x}\, w_{,xx} + \frac{1-\nu}{2}\frac{w_{,x}^2}{x} = 0. \qquad (2.8\text{-}2)$$

Nondimensional membrane stresses are given by

$$\sigma_r = \frac{1}{(1-\nu^2)}\left(u_{,x} + \frac{1}{2}w_{,x}^2 + \nu\frac{u}{x}\right) + \sigma_0 \qquad (2.9\text{-}1)$$

and

$$\sigma_\theta = \frac{1}{(1-\nu^2)}\left(\frac{u}{x} + \nu u_{,x} + \frac{\nu}{2}w_{,x}^2\right) + \sigma_0. \qquad (2.9\text{-}2)$$

From Eqs.(2.8), note that one set of solutions $\{w, u, \sigma_r, \sigma_\theta, \varepsilon_r, \varepsilon_\theta\}$ exists for each set of $\{\nu, \sigma_0,$ boundary conditions$\}$. It should also be noted that solving Eqs. (2.8) does not require knowledge of pressure, Young's modulus, thickness, or size of the outermost radius. The only geometric parameters involved are those in the boundary conditions. For the island blister test, this is the nondimensional island radius a. For the constrained blister test, this is the nondimensional constraint height. For the standard blister test, there is no geometric parameter involved when solving the nondimensional equations, Eqs.(2.8).

The volume under the deformed membrane can be presented in two different forms, true volume $\overline{V}$, and nondimensional volume B, which are expressed as

$$\overline{V} = 2\pi\int \overline{w} r dr, \qquad (2.10\text{-}1)$$

$$B = 2\pi\int w x dx. \qquad (2.10\text{-}2)$$

Since the closed form solutions for Eqs. (2.8) are not available, a nonlinear relaxation technique proposed by Kao and Perrone (1971), which is an iterative approach used in conjunction with finite difference approximations, will be used to solve the above nonlinear equations. Although the closed form solution is not available, only a minimal numerical effort is needed to determine the effects of each parameter on the nondimensional form of the governing equations, Eqs.(2.8).

The boundary conditions for the standard blister geometry are

$$w_{,x} = u = 0 \text{ at } x = 0, \tag{2.11-1}$$

$$w = u = 0 \text{ at } x = 1. \tag{2.11-2}$$

The solutions w(x) and u(x) depend only on Poisson's ratio ν and the nondimensional prestress σ_0. There is no geometric parameter involved for the nondimensional solution. For the case without prestress, i.e., $\sigma_0 = 0$, the solutions w(x) and u(x) and therefore σ_r and σ_θ, depend only on Poisson's ratio.

The boundary conditions for the island blister geometry are

$$w = u = 0 \text{ at } x = a, \tag{2.12-1}$$

$$w = u = 0 \text{ at } x = 1. \tag{2.12-2}$$

The solutions w(x) and u(x) depend only on Poisson's ratio ν, nondimensional island radius a, and the nondimensional prestress σ_0. For the case without prestress, i.e., σ_0=0, the solution w and u and therefore σ_r and σ_θ, depend only on the Poisson's ratio and the nondimensional island radius.

2.3 Energy Release Rate

2.3.1 Generalized Compliance Approach

If the generalized force P, and generalized displacement V, of a system satisfy

$$\left(\frac{V}{C}\right)^n = P, \tag{2.13}$$

where C is the generalized compliance, then the energy release rate can be expressed as (Chang *et al.*, 1989)

$$G = \frac{n}{n+1} P^{\frac{n+1}{n}} \frac{\partial C}{\partial A}. \tag{2.14}$$

where A is the debond area.

2.3.2 Energy Release Rate for Various Circular Blister Geometries

The energy release rate can be obtained from the following energy balance equation with an infinitesimal debond area growth δA:

$$G\delta A = \delta W - \delta U + \delta Z, \tag{2.15}$$

where

δA is the change of the debond area,

δW is the change of the external work,

δU is the change of the strain energy,

and δZ is the plastic and viscoelastic energy dissipation during the debonding process.

Since most of the current fracture mechanics practice in the testing and analysis of adhesively bonded joints is limited to linear elastic fracture mechanics methods, the derivation of the energy release rate in the current study will be similarly constrained. Therefore, it is assumed that the energy dissipation due to bulk viscoelastic and plastic effects may be neglected, so that the following energy balance equation will be used throughout all derivations of the energy release rate:

$$G\delta A = \delta W - \delta U. \tag{2.16}$$

Standard Blister Test

By using the energy balance equation Eq. (2.16) the energy release rate for the standard blister test with an arbitrary magnitude of prestress can be obtained as

$$G=\frac{(pR)^{4/3}}{3(Eh)^{1/3}}\left\{\frac{1}{\pi}\left[5B-\sigma_0\frac{\partial B}{\partial\sigma_0}\right]-\left(5-\sigma_0\frac{\partial}{\partial\sigma_0}\right)\right.$$
$$\left.\int_0^1\left[\left((\sigma_r-\sigma_0)^2-2\nu(\sigma_r-\sigma_0)(\sigma_\theta-\sigma_0)+(\sigma_\theta-\sigma_0)^2\right)+2(1-\nu)\sigma_0(\sigma_r+\sigma_\theta-2\sigma_0)\right]xdx\right\} \tag{2.17}$$

The quantities in the first bracket of Eq. (2.17) correlate the variation in the applied work and the ones in the integration correlate the variation in the strain energy. For the case without prestress, one can simply substitute zero for σ_0 and obtain the energy release rate without prestress. Alternately, one can obtain the energy release rate for a membrane without prestress using the compliance approach, Eq. (2.14), since the power form in Eq. (2.14) can be found for this case. The energy release rate can be expressed as

$$G=\frac{5B}{4\pi}\frac{(pR)^{4/3}}{(Eh)^{1/3}}. \tag{2.18}$$

It should be noted that the compliance approach can not be used when prestress is not zero, since the power form in Eq. (2.14) is not valid in the case with prestress.

Island Blister Test

Similarly, the energy release rate for the island blister test with an arbitrary magnitude of prestress can be obtained as

$$G=\frac{(pR)^{4/3}}{2a(Eh)^{1/3}}\left\{\frac{1}{\pi}\frac{\partial B}{\partial a}-\right.$$
$$\left.\frac{\partial}{\partial a}\int_a^1\left[\left((\sigma_r-\sigma_0)^2-2\nu(\sigma_r-\sigma_0)(\sigma_\theta-\sigma_0)+(\sigma_\theta-\sigma_0)^2\right)+2(1-\nu)\sigma_0(\sigma_r+\sigma_\theta-2\sigma_0)\right]xdx\right\} \tag{2.19}$$

where $$a=\frac{R_{island}}{R}. \tag{2.20}$$

For the case without prestress, one can simply substitute zero for σ_0 and obtain the normalized energy release rate without prestress. On the other hand, one can obtain G for the case without prestress using the generalized compliance approach as

$$G = \frac{(pR)^{4/3}}{(Eh)^{1/3}} \frac{3}{8\pi} \frac{\partial B}{a \partial a}. \tag{2.21}$$

2.4 Mixed Mode Delamination for Films and Coatings

The fundamental problem that underlies many aspects of the mechanics of film delamination has been analyzed by Suo and Hutchinson (1990, 1992) and is illustrated in Fig.2.6. Any arbitrary set of loads that may act to cause the film to debond can be represented by a single force, N, per unit width, acting along the mid-plane of the film, and a bending moment, M, per unit width, provided that the crack tip is sufficiently far removed from the edge of the sample or from other points of application of the loads.

In Suo and Hutchinson's analysis, bending moment has been considered, while the membrane analysis in Sections 2.2 and 2.3 neglects the bending effect. The relationship between membrane analysis and Suo and Hutchinson's analysis will be discussed in Section 2.4.2.

2.4.1 Energy Release Rate and Mode Mixity

For a plane geometry, assuming that the substrate is infinitely thick and both the substrate and film are isotropic elastic solids, Suo and Hutchinson (1990, 1992) found that the energy release rate at the tip of the crack is given by

$$G = (N^2 + 12M^2 / h^2) / 2\hat{E}_1 h, \tag{2.22}$$

where h is the film thickness,

$\hat{E}_1 = E_1$ in plane stress case,

$\hat{E}_1 = E_1/(1-\nu_1^2)$ in plane strain case,

E_1 is Young's modulus of the film,

and ν_1 is Poisson's ratio of the film.

Suo and Hutchinson also showed that a measure of the mode mixity at the crack tip is defined as

$$\tan\psi = \frac{\mathrm{Im}(Kh^{i\varepsilon})}{\mathrm{Re}(Kh^{i\varepsilon})} = \frac{K_{II}}{K_I} = \frac{\sqrt{12}M\cos\omega + hN\sin\omega}{-\sqrt{12}M\sin\omega + hN\cos\omega}, \tag{2.23}$$

where K is the complex stress intensity factor and is given by $K = K_I + iK_{II}$,

K_I is the mode I stress intensity factor,

K_{II} is the mode II stress intensity factor,

ψ is the phase angle,

ε is a bimaterial parameter given by $\varepsilon = \frac{1}{2\pi}\ln\frac{1-\beta}{1+\beta}$. (2.24)

ω is a function of Dundur's parameters α and β, and the film thickness h. ω has been tabulated by Suo and Hutchinson (1990). The Dundur's parameters are given by

$$\alpha = (\hat{E}_1 - \hat{E}_2)/(\hat{E}_1 + \hat{E}_2), \tag{2.25}$$

$$\beta = \frac{\mu_1(\kappa_2 - 1) - \mu_2(\kappa_1 - 1)}{\mu_1(\kappa_2 + 1) + \mu_2(\kappa_1 + 1)}, \tag{2.26}$$

where

μ_1 and μ_2 are the shear moduli,

$\kappa_1 = 3 - 4\nu_1$ and $\kappa_2 = 3 - 4\nu_2$ for plane strain case, and $\kappa_1 = (3-\nu_1)/(1+\nu_1)$ and $\kappa_2 = (3-\nu_2)/(1+\nu_2)$ for plane stress case,

and the subscripts 1 and 2 refer to the film and substrate, respectively.

2.4.2 Maximum Stress

Most of the current fracture mechanics practice in the testing and analysis of adhesives and the design of adhesively bonded joints is limited to linear elastic fracture mechanics. In a cracked body or structure, the crack tip is the location with the highest stress because of the singularity of the stress field near the crack tip. This high very stress field is often confined to a small region, which results in a small plastic zone at the crack tip. However, the plastic zone size may increase due to the high applied load and/or high fracture resistance. Linear elastic fracture mechanics may not be applicable if the plastic zone size is large when compared to the length of a through-the-thickness crack in an infinite plate subjected to tensile load or when compared to the adherend or film thickness in an adhesively bonded joint with a long crack along the bondline. As long as the plastic zone size is small, linear elastic fracture mechanics will be applicable even though the specimen or structure may be subjected to plastic deformation other than the crack tip plastic zone. Although energy release rates or stress intensity factors can still be determined based on linear elastic fracture mechanics, the analysis which needs to consider the plastic deformation other than crack tip plastic zone is often very complicated. The elastic-plastic analyses for a double cantilever beam test by Chang et al. (1972) and for a thin film peeling test by Kim (1988a and 1988b) are examples for how complicated these type of analysis can be. As a result, most of the testing and analysis for strength of adhesive bond strength are based not only on linear elastic fracture mechanics (LEFM), but also on the assumption that there is no plastic deformation due to the nonsingular stress field in the adherends or films.

One may estimate the plastic zone size based on the stress intensity factors using the methods similar to those by Broek (1982) for homogeneous material or by Zywicz and Parks (1989) for an interfacial crack and then determine whether linear elastic fracture mechanics is applicable. In the current study, the focus is not be on whether linear elastic fracture mechanics is applicable, but on whether there is gross yielding caused by non-

singular stress in the adherends or films. For the purpose of easy distinction throughout the dissertation, the term "gross yielding" will be used when plastic deformation is due to the non-singular stress exceeding the yield stress in the adherends or films and the terms "small scale yielding" and "large scale yielding" will be used when plastic deformation is due to the stress in the high stress field exceeding the yield stress of the material at the crack tip. To determine whether gross yielding has occurred, we need to determine the maximum stress based on mechanics of materials such as beam, plate or membrane theory. Therefore, in this dissertation, when the term "maximum stress" is used, it refers to the maximum stress ignoring the singular stress field near the crack tip and is obtained based on mechanics of materials.

In a membrane, although maximum membrane stress can be found from a membrane solution, the maximum stress is often not the maximum membrane stress if the bending stress is not negligible, such as at the edge of a suspended membrane at the debond front, which is more like a clamped edge than a hinged edge. Therefore, one needs to determine the bending stress at the edge of the suspended membrane to properly determine the maximum stress. In the membrane analyses for the standard and island blisters, a hinged edge is used as the boundary of the membrane. However, a clamped edge may be more realistic than a hinged edge, considering that except for the pressurized portion, the rest of the film is bonded to the substrate. Since a clamped edge may be more realistic than a hinged edge, one needs to know under what conditions the membrane stresses obtained from a membrane solution converge to the membrane stress obtained from the plate solution with a clamped edge. To answer this question, the results from a comprehensive study of pressurized circular plates by Broadland (1986) may be used. Broadland found that as the nondimensional load $\frac{pR^4}{Dh}$, with D being the bending rigidity, increases, the results obtained from a nonlinear plate solution with both clamped and hinged edge boundary conditions, which is based on large displacement and large rotation assumptions, converge to those obtained from the membrane solutions. In the case of a clamped edge,

when the nondimensional load approaches 10^5, the membrane stresses at the edge obtained from the membrane solution converge to those from the nonlinear plate solution. At this nondimensional load and at the edge of the plate, the plate solution gives a bending stress at the top and bottom surfaces about 2.5 times the meridian membrane stress. The results suggest that the membrane solution accurately predicts the membrane stress, no matter what the realistic edge condition is, as long as the nondimensional load is large enough. From the test parameters obtained from Allen and Senturia (1988) and Gent and Lewandowski (1987), the nondimensional loads are found to be larger than 106, which suggests that the membrane stress can be adequately determined from the membrane solution.

Accurate determination of the membrane edge stresses is important since the bending moment, therefore bending stress, at the edge of the membrane, can be derived from the meridian membrane stress and the energy release rate from Eq. (2.22). This edge membrane stress is given by:

$$M = \left[\frac{GEh^3}{6(1-\nu^2)} - h^2 N^2 / 12 \right]^{1/2}, \tag{2.27}$$

where N is the difference of stress resultants at both sides of the crack tip.

The nondimensional bending stress of the film at the debond front can be written as

$$\sigma_b = (\sigma_{mt} - \sigma_0)\left[\frac{6g}{1-\nu^2} - 3 \right]^{1/2}, \tag{2.28}$$

where σ_{mt} is the nondimensional membrane stress at the debond front,

$$g = \frac{\left\{ \frac{1}{\pi}\left[5B - \sigma_0 \frac{\partial B}{\partial \sigma_0} \right] - \left(5 - \sigma_0 \frac{\partial}{\partial \sigma_0} \right) \int_0^1 \left[\left((\sigma_r - \sigma_0)^2 - 2\nu(\sigma_r - \sigma_0)(\sigma_\theta - \sigma_0) + (\sigma_\theta - \sigma_0)^2 \right) + 2(1-\nu)\sigma_0(\sigma_r + \sigma_\theta - 2\sigma_0) \right] x dx \right\}}{\left[\sigma_{mt}(\nu, \sigma_0) - \sigma_0 \right]^2} \tag{2.29}$$

for the standard blister,

and

$$g = \frac{\frac{1}{2}\frac{1}{a}\left\{\frac{1}{\pi}\frac{\partial B}{\partial a} - \frac{\partial}{\partial a}\int_a^1 \left[\left((\sigma_r - \sigma_0)^2 - 2\nu(\sigma_r - \sigma_0)(\sigma_\theta - \sigma_0) + (\sigma_\theta - \sigma_0)^2\right) + 2(1-\nu)\sigma_0(\sigma_r + \sigma_\theta - 2\sigma_0)\right] x dx\right\}}{\left[\sigma_{mt}(\nu, \sigma_0) - \sigma_0\right]^2} \tag{2.30}$$

for the island blister.

To determine the maximum stress in a membrane, one needs to compare the maximum membrane stress and the combined membrane and tensile bending stress at the edge of the membrane. The larger of the two stresses is the maximum stress. In a standard blister specimen, the maximum membrane stress is located at the center of the membrane and is about 20% larger than the membrane stress at the edge of the membrane. However, it is significantly smaller than the typical bending stress at the edge, which is about 2.5 times the membrane stress at the edge. Therefore, the maximum stress is located at the edge of the membrane and is equal to the sum of the membrane stress and the tensile bending stress.

In the island blister, the maximum stress is located at the edge of the membrane, since the maximum membrane stress is also located there. From the discussion for the standard and island blisters, the nondimensional maximum tensile stress, ignoring the crack tip singularity, can be found at the debond front as

$$\sigma_{max} = \sigma_{mt} + \sigma_b . \tag{2.31}$$

The effect of the maximum stress will be discussed in Chapter 6 where the relationship between the criteria for debonding and yielding is discussed in detail.

2.5 Results and Discussions

Standard Blister

Figure 2.7 illustrates the nondimensional membrane stress distributions of the standard blister without prestress along the radial direction for different Poisson's ratios. For the cases with and without prestress, the maximum membrane stress is located at the center of the blister for all practical values of Poisson's ratio. However, if the bending stress is taken into consideration, the maximum tensile stress is located at the edge of the debond front regardless of the prestress. Typically, the maximum nondimensional bending stress is 1.9 which is nearly five times the membrane stress at the edge. Thus, yielding will most likely occur at the edge of the debond front. It should be noted that the bending moment obtained from Eq.(2.27) has a 0.5% difference compared with the result obtained from a boundary layer solution by Jensen (1991).

When the prestress in the membrane is so large that the stresses due to the pressurization are negligible compared to the prestress, the membrane solution can be easily solved based on the governing equation (Landau and Lifshitz, 1970)

$$\nabla^2 \overline{w} = -\frac{p}{\overline{\sigma}_0 h}. \tag{2.32}$$

It is interesting to see that the above equation is independent of material properties. For the axisymmetrical case, Eq.(2.32) can be written as

$$\frac{1}{r}\frac{d}{dr}\left(r\frac{d\overline{w}}{dr}\right) = -\frac{p}{\overline{\sigma}_0 h}. \tag{2.33}$$

$\overline{w}$ can be easily found by solving the above equation and imposing the boundary conditions $\left(\frac{d\overline{w}}{dr}\right)_{r=0} = 0$ and $\overline{w}=0$ at r=R. With displacement found, the volume of the blister and therefore the energy release rate can then be determined as

$$G = \frac{p^2 R^2}{8\bar{\sigma}_0 h}. \tag{2.34}$$

It should be noted that the above equation has a different form from the one for the general prestress equation, Eq. (2.27), in that G is proportional to the square of pressure, indicative of a linear pressure/volume relation. By introducing the nondimensional prestress as seen in Eq. (2.7), Eq. (2.35) can be modified as

$$G = \frac{1}{8\sigma_0} \frac{(pR)^{4/3}}{(Eh)^{1/3}}. \tag{2.35}$$

Figure 2.8 illustrates the nondimensional maximum membrane stress versus nondimensional prestress obtained from the dominant prestress solution and general prestress solution. The Poisson's ratio for the general prestress solution is 0.3. The nondimensional membrane stresses increase as prestress increases. As would be expected, the variation between the two solutions decreases as the prestress increases. When the nondimensional prestress is equal to 1.0, the percent difference between the two solution is about 6.1%.

Figure 2.9 illustrates the nondimensional energy release rate versus nondimensional prestress for the dominant prestress solution and the general prestress solution of three Poisson's ratios, 0.0, 0.3, and 0.5. In the general prestress solution, the energy release rates converge to finite values as the prestress approaches zero, while the energy release rate approaches infinity for the prestress dominant solution. The large error between the general prestress and prestress dominant solutions at small nondimensional prestress demonstrates that prestress dominant solution is not valid at a small nondimensional prestress. It is also found that the energy release rates of the Poisson's ratios from 0.0 to 0.5 at all prestresses, the curve of ν=0.0 is the upper bound while the one of ν=0.5 is the lower bound. As the nondimensional prestress increases, the difference of the energy release rates between ν=0.0 and ν=0.5 decreases and the energy release rates converge to that of the dominant prestress solution. While the percent difference of maximum

membrane nondimensional stress between the dominant prestress and general prestress solutions at nondimensional prestress of 1.0 is about 6.1%, the percent difference of energy release rates is about 3%. The convergence of the dominant prestress and the general prestress solutions also suggests that the material properties have a decreasing effect as prestress increases. Therefore, one may make reasonable estimates of the material properties and then use Eq. (2.17) to calculate the energy release rates without causing large errors. It should be noted that the nondimensional prestress is a relative quantity of prestress, pressure, geometry, and Young's modulus. As the pressure increases, the effect of prestress decreases. Therefore, the effect of prestress cannot be predicted only based on the conditions before the experiment but the conditions during the experiment must also be considered.

Although the energy release rate of the standard blister test can be determined based on Eqs. (2.17) and (2.18), it is not a convenient way to find the energy release rate for the standard blister test. Fortunately, an approximate formula based on the results of the analytical solution can be derived. Assuming the energy release rate is a second order polynomial of nondimensional prestress and the coefficients of this polynomial are first order polynomials in Poisson's ratio, an approximate formula of energy release rate can be obtained by curve fitting the data from the results of the upper and lower bounds, n=0.0 and n=0.5. The approximate formula is expressed by

$$G = \left[(-0.241\nu + 0.3195)\sigma_0^2 + (0.3952\nu - 0.6528)\sigma_0 + (-0.1678\nu + 0.4636)\right]\frac{(pR)^{4/3}}{(Eh)^{1/3}}. \tag{2.36}$$

The comparison between the analytical solution and approximate formula for a Poisson's ratio of 0.3 is illustrated in Fig. 2.10. Good agreement is seen between the two curves. The error is between -4.5% and 4.5% between a nondimensional prestress of 0.0 and 1.0.

The use of Eq. (2.36) offers one an easy way to calculate the energy release rate for the standard blister test for various material properties and prestresses. The approximate

solution eliminates the laborious numerical effort as done in this chapter or by Gent and Lewandowski (1987). In order to check the accuracy of the fitted curve, Gent's data (1987) were used to compare with the fitted values. The difference between the fitted value and Gent's data is about 2% for a Poisson's ratio of 0.5. It should be noted that since the order of the prestress and Poisson's ratio are chosen relatively arbitrarily, their coefficients do not have any physical meaning.

Figure 2.11 illustrates the phase angle versus nondimensional prestress for a standard blister test. In spite of the change in prestress, the mode mixity does not vary much. It is also interesting to observe from Eq. (2.17) that the pressure is inversely proportional to debond radius for a given energy release rate. Since the product of p and R is a constant, the nondimensional prestress is a constant and therefore, the phase angle is a constant during the debonding process even though the take-off angle may change during the process.

Island Blister

A typical nondimensional membrane stress distribution of the island blister is illustrated in Fig. 2.12, The specimen has a nondimensional prestress of 0.64 as found in the polyimide film studied by Allen and Senturia (1988,1989). The nondimensional island size is 1/150 and Poisson's ratio is 0.34. To check the convergence of the nonlinear relaxation iteration technique used in this study, the models of several different meshes with 21, 41, and 81 nodes were used. All meshes show satisfactory results except for the stresses at the edge of the island. An axisymmetrical nonlinear finite element model of 150 elements was also used to compare with the results from analytical solutions. The FE mesh consists of three layers of elements through the thickness. Since only membrane stress was to be compared with the analytical solution, the mesh was not refined enough to obtain the singular behavior of the stress field very near the crack tip. The finite element program used was ABAQUS (1991) and the element type used was an eight node

quadrilateral element. Very good agreement is seen between the finite element and the analytical results of different mesh sizes except in the region near the island. High stress concentration is seen near the edge of the island. To find the maximum membrane stress at the edge of the island, the finite difference mesh was refined near the edge of the island until a convergent value was found. In the region away from the island, the membrane stress is a little higher than the prestress, which suggests that the prestress is high enough to dominate the stress field in the region far away from the island for this case. From all the island blister analyses, the maximum membrane stress is found to be located at the edge of the island.

Figure 2.13 illustrates the nondimensional energy release rate and nondimensional maximum membrane stress versus nondimensional island radius for an island blister test without prestress. Both energy release rate and maximum stress increase significantly as the island size decreases. Whether gross yielding occurs during the debonding process depends on whether the maximum stress exceeds the critical stresses of the film. The results suggest that the island blister test is capable of producing very high energy release rates at relatively low pressures, but not without high local stresses.

In order to understand the effects of the island radius and prestress on the energy release rate and the maximum stresses of the island blister test, results with various island radii and prestress were obtained and are shown in Figs. 2.14 and 2.15.

Figure 2.14 illustrates the nondimensional energy release rate versus nondimensional island radius in an island blister test with different nondimensional prestress. The energy release rate increases significantly as the island radius decreases. As the island radius reaches zero, which is the moment the specimen debonds completely, the energy release rate is expected to reach infinity since a finite compliance change is accompanied with an from 1.22 for $\sigma_0 = 0$ to 1.45 for $\sigma_0 = 15$.

Figure 2.15 illustrates nondimensional energy release rate versus nondimensional prestress in an island blister test with different nondimensional island radius. It is seen that

when the nondimensional prestress is smaller than about 0.3, the effect of the prestress can be neglected. In this figure, the dominant prestress solutions (Allen and Senturia (1988, 1989)) are also used to illustrate the nondimensional prestress range where the stress induced by the pressure is negligible compared to prestress. It is noted that the applicable range of the dominant prestress solution depends on both nondimensional island radius and nondimensional prestress. As the island radius increases, the dominant prestress range increases. By taking the typical nondimensional prestress, 0.64, and nondimensional island radius, 0.1, from Allen and Senturia (1988, 1989), relatively good agreement is seen between the dominant prestress and general prestress solutions. This finding suggests that although Allen and Senturia used a relatively simple equation to calculate the energy release rate, the results are acceptable because the combination of prestress and island radius used in their tests is in the range where the specimen is prestress dominated.

Figure 2.16 illustrates the phase angle versus nondimensional island radius in an island blister test with a nondimensional prestress of 0.64 and a Poisson's ratio of 0.3. The Dundur's parameters are chosen so that no contact between the film and substrates could occur due to the material properties. Although the strain energy release rate may increase significantly as the island radius decreases, the phase angle decreases only slightly.

2.6 Summary

In this chapter, the membrane solutions for the standard and island blisters were derived. The study of the membrane stress distributions showed that a very high local stress concentration was found at the edge of the island in a island blister, while the membrane stress was relatively uniform all over the rest of the membrane. The high energy release rate in the island blister was attributed to the high stress concentration at the debond front. It was found that both the energy release rate and the membrane stress at the edge of the island increased significantly as the island size decreased. For example,

in Fig. 2.13, if the island size is reduced by 10 times, the energy release rate increases by about 16 times, while the maximum stress increases by about 4 times.

Arbitrary magnitudes of prestress was also considered in the membrane solutions which were used to study the error and applicable range of the two commonly used extreme solutions - no-prestress and prestress dominant solutions. It was found that the misuse of either extreme solution in the wrong prestress and pressure range would result in large error.

The study of the mode mixity in the standard and island blister tests suggested that the mode mixity should remain constant during the debonding process in both tests if the energy release rate remains constant. It was also found that the difference of the phase angle between the two tests was small.

An approximate energy release rate formula for the standard blister was also proposed. The energy release rate could be easily found using this formula and error is within 4.5%.

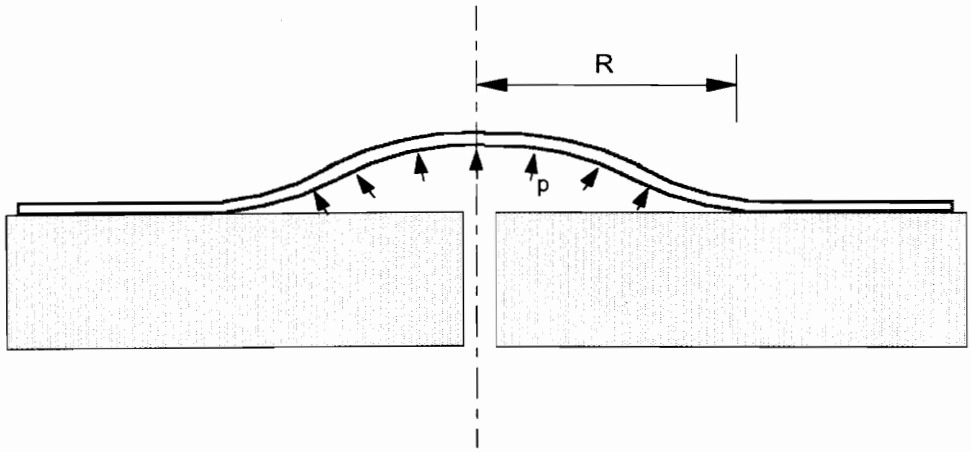

Figure 2.1 Illustration of the standard blister test.

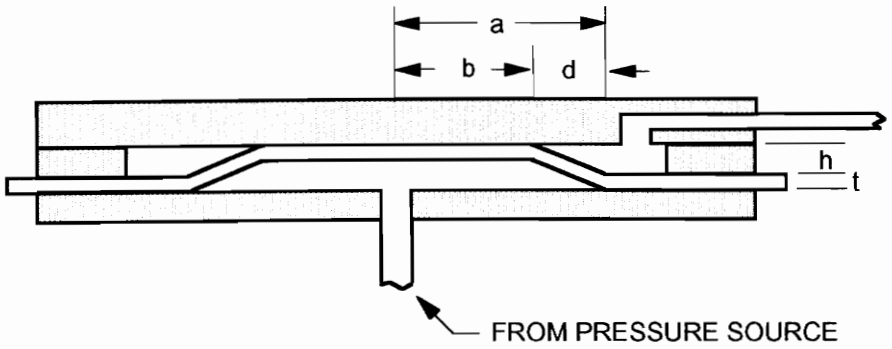

Figure 2.2 Illustration of the constrained blister test.

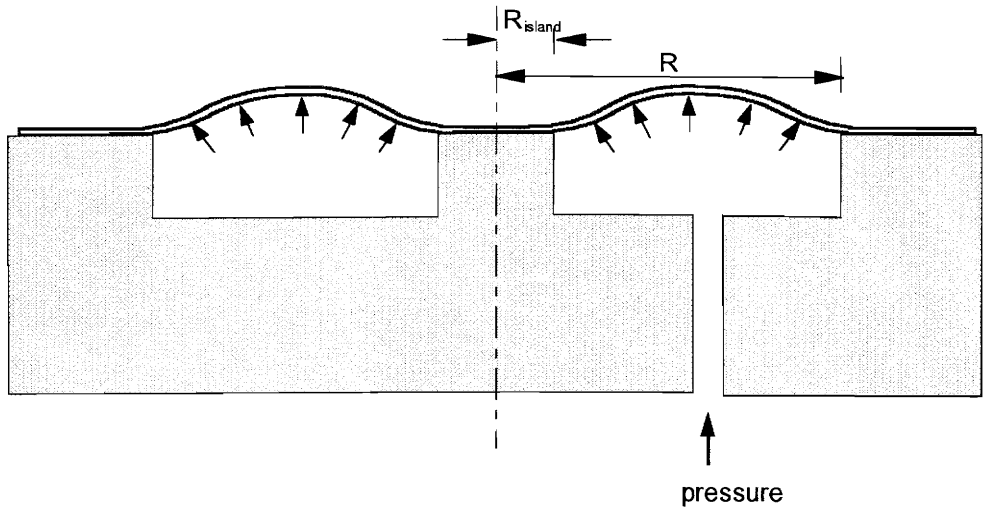

Figure 2.3 Illustration of the island blister test.

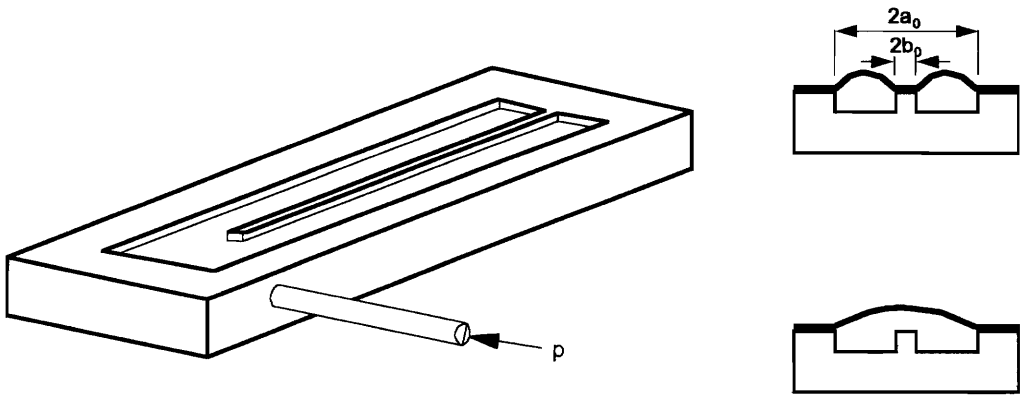

Figure 2.4 Illustration of the peninsula blister test.

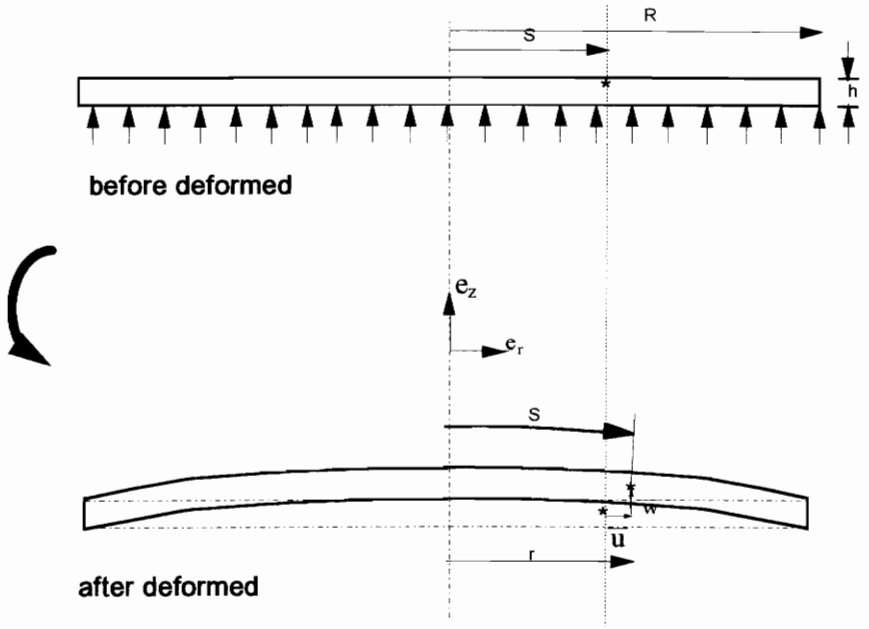

Figure 2.5 The cross section of a pressurized membrane.

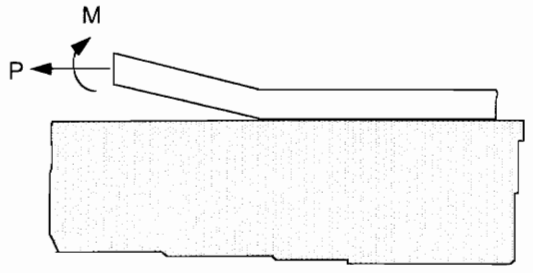

Figure 2.6 Coating with an interface crack subjected to axial and bending loads.

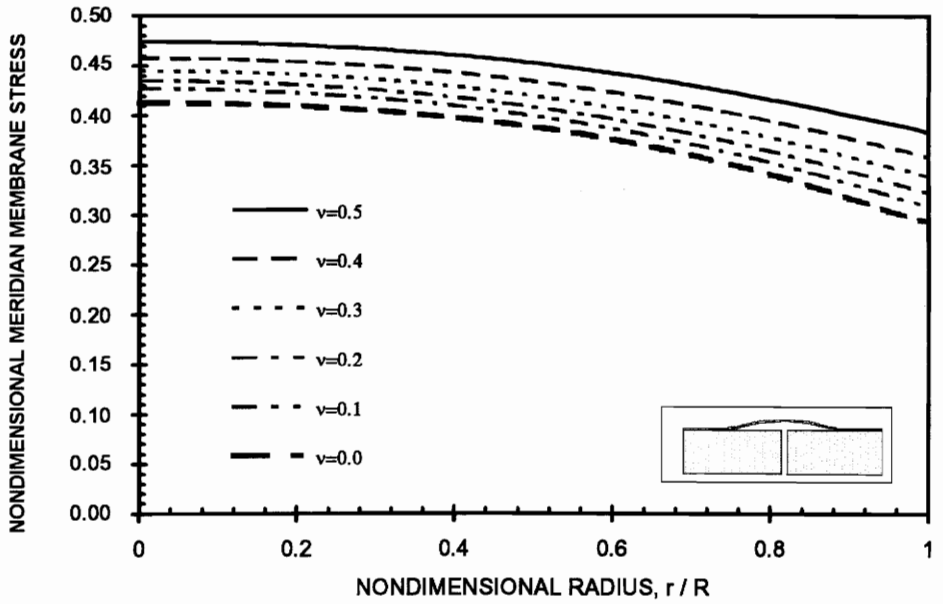

Figure 2.7 Nondimensional membrane stress distributions in a standard blister without prestress along the radial direction for different Poisson's ratios.

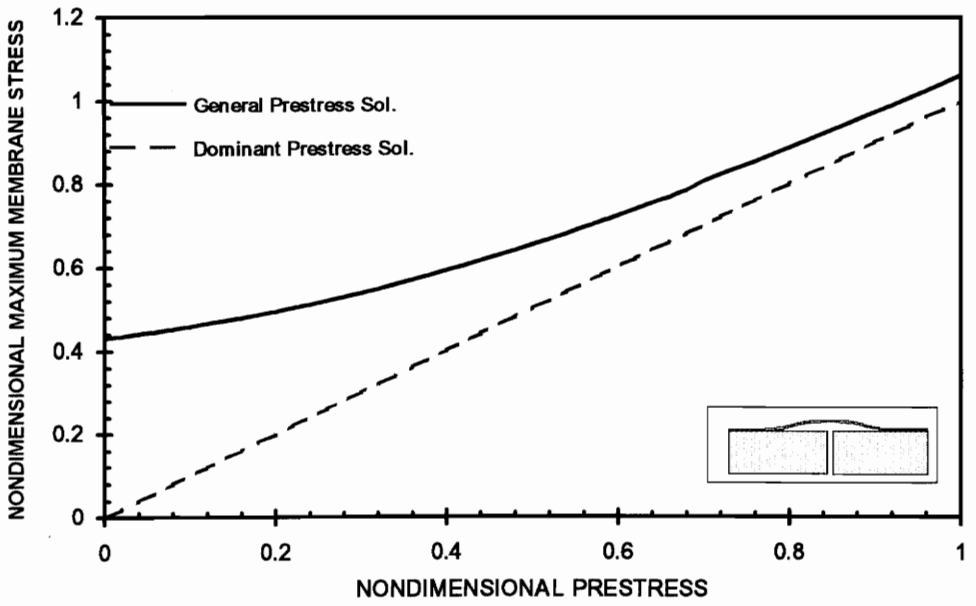

Figure 2.8 Nondimensional maximum membrane stresses from the dominant prestress and general prestress solutions versus nondimensional prestress. Poisson's ratio is 0.3.

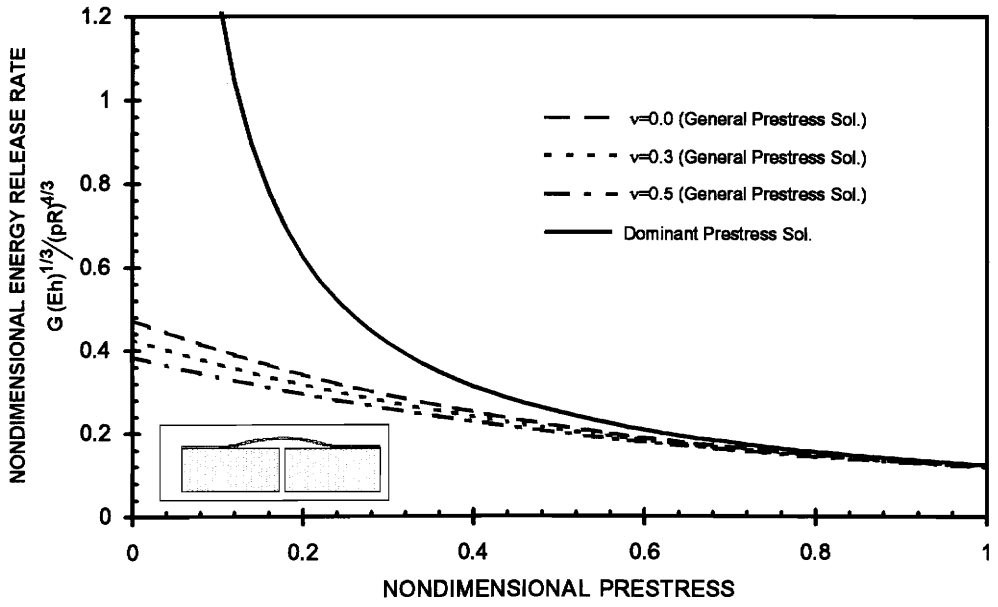

Figure 2.9 Nondimensional energy release rate versus nondimensional prestress obtained from the dominant prestress solution and the general prestress solution of three Poisson's ratios, 0.0, 0.3, and 0.5.

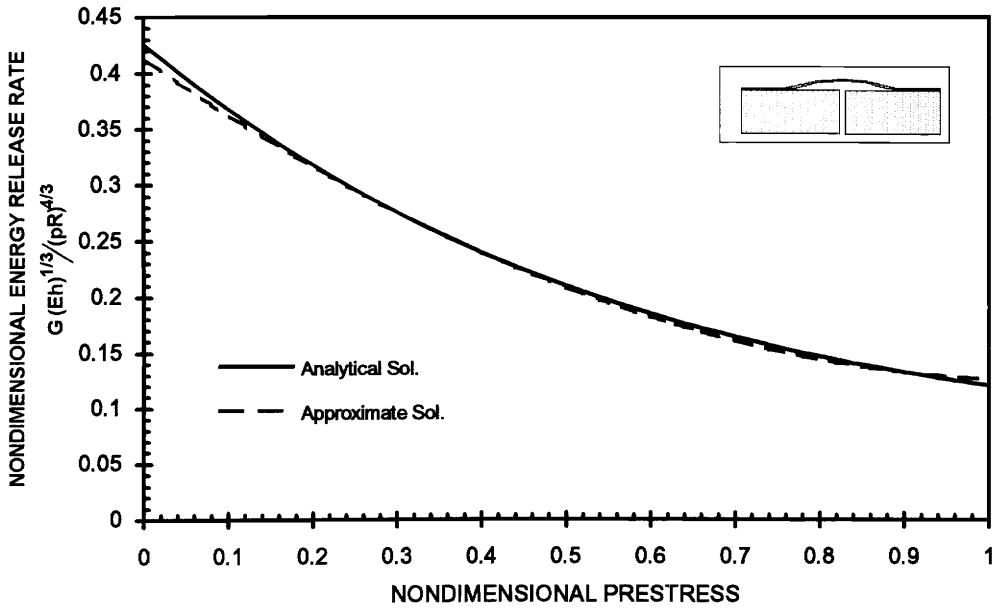

Figure 2.10 Comparison of the nondimensional energy release rate from the analytical solution and the approximate formula. Poisson's ratio is 0.3.

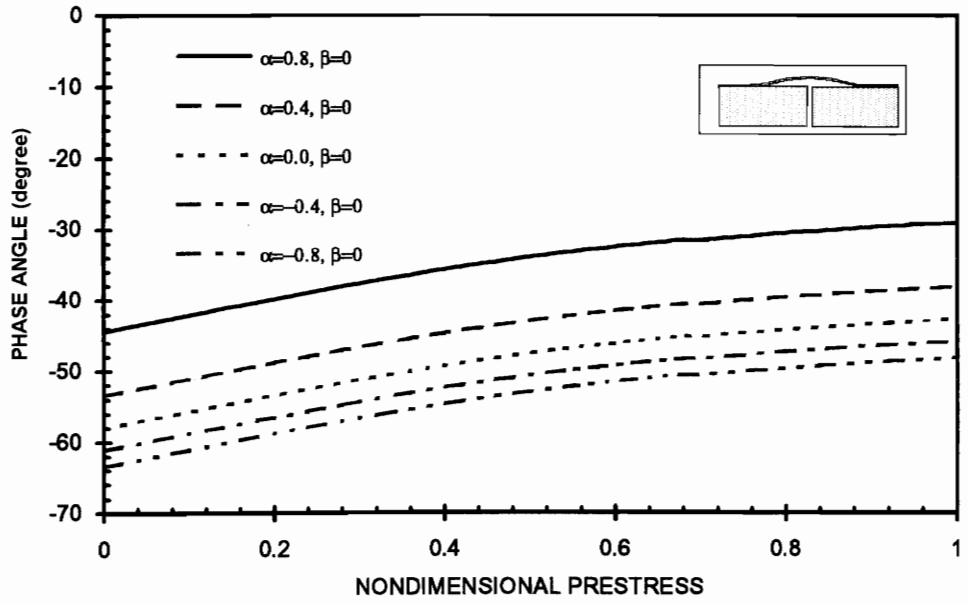

Figure 2.11 Phase angle versus nondimensional prestress for a standard blister test with a Poisson's ratio of 0.3.

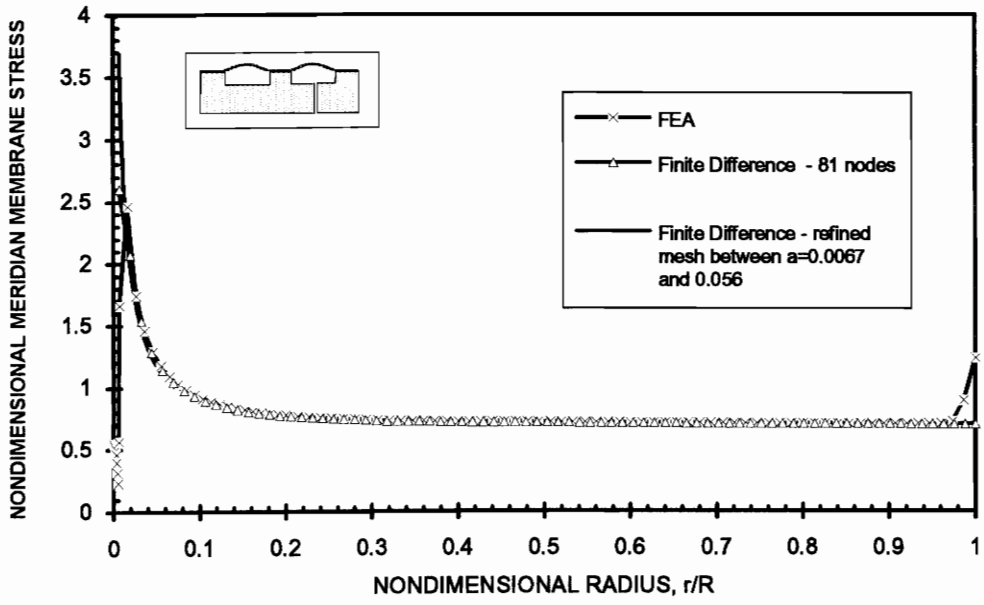

Figure 2.12 Nondimensional membrane stress distribution in a island blister test with a nondimensional prestress of 0.64 and a Poisson's ratio of 0.34. The nondimensional island radius is 1/150.

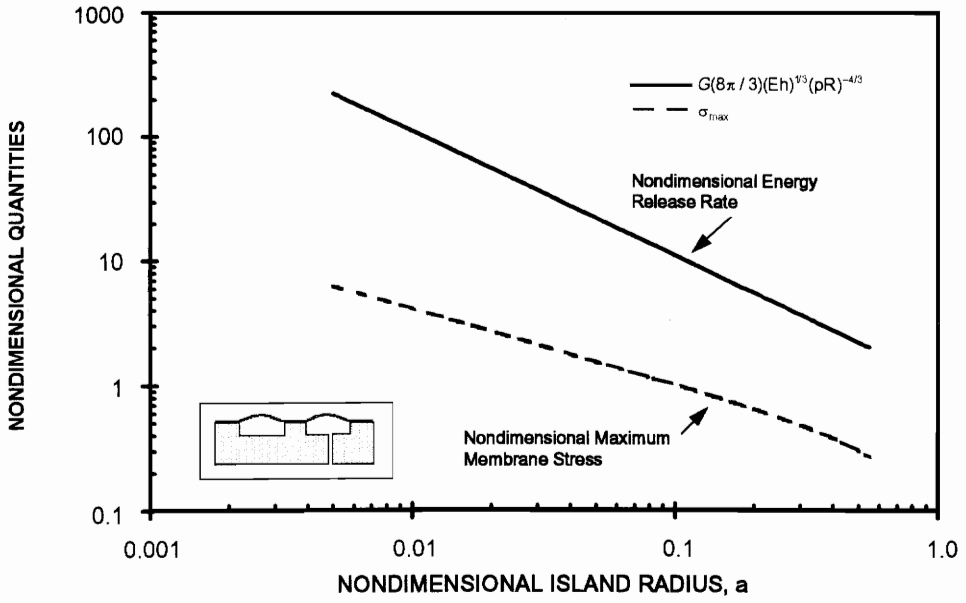

Figure 2.13 Nondimensional energy release rate and nondimensional maximum membrane stress versus nondimensional island radius for an island blister test without prestress. Poisson's ratio is 0.3.

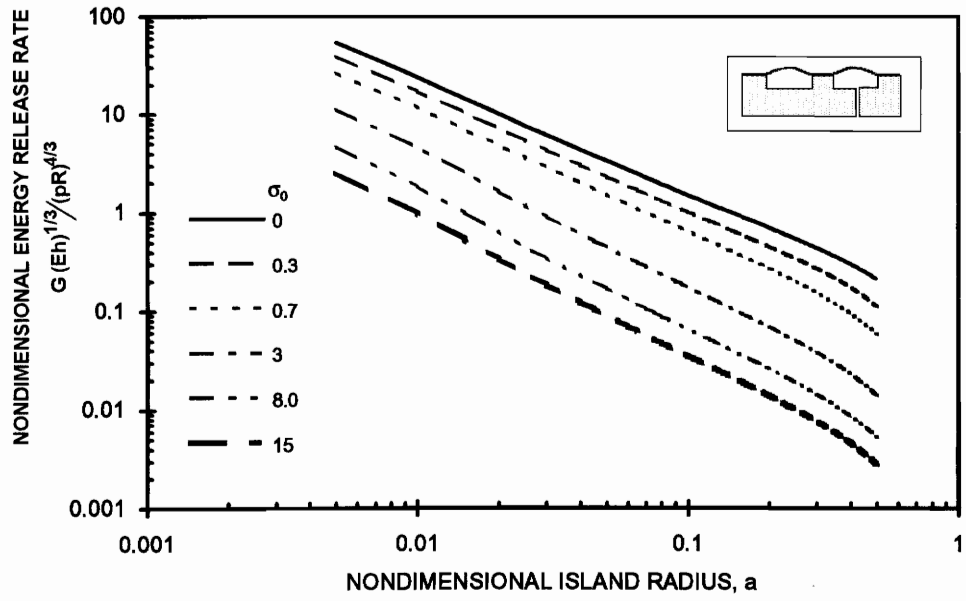

Figure 2.14 Nondimensional energy release rate versus nondimensional island radius in an island blister test with different nondimensional prestress.

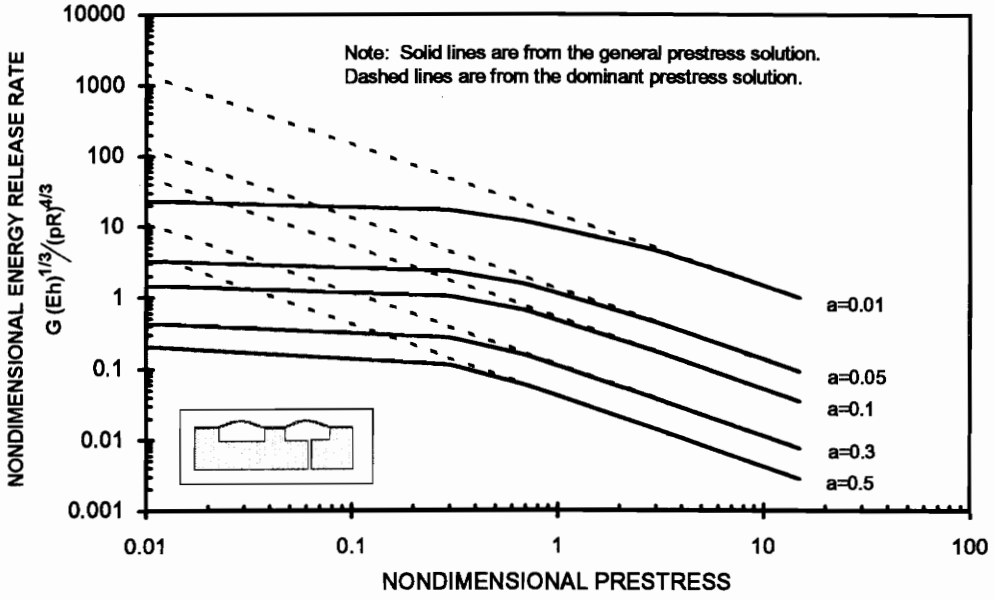

Figure 2.15 Nondimensional energy release rate versus nondimensional prestress in an island blister test with different nondimensional island radius. Poisson's ratio is 0.3.

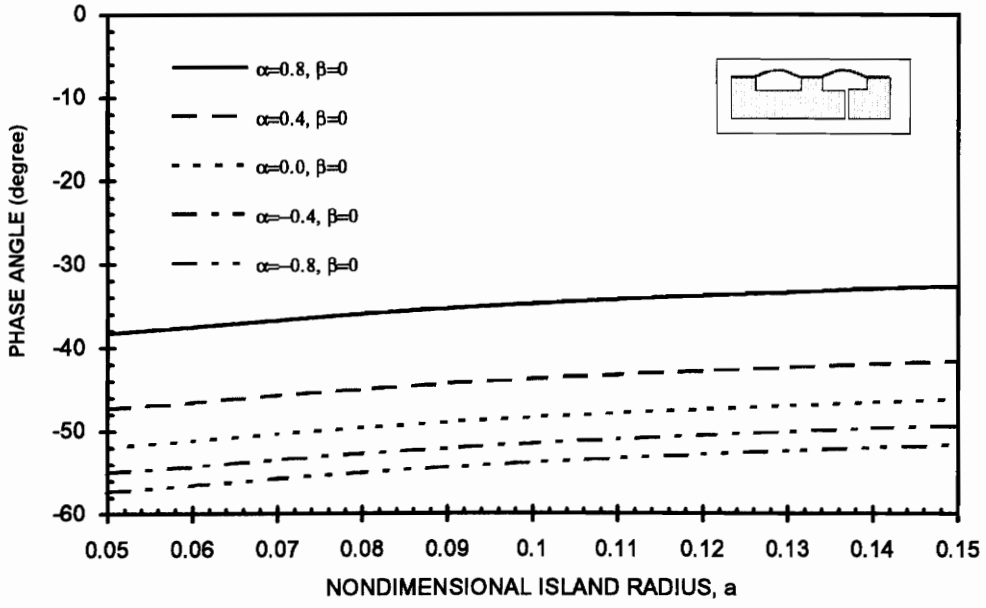

Figure 2.16 Phase angle versus nondimensional island radius in an island blister test with a nondimensional prestress of 0.64 and a Poisson's ratio of 0.3.

Chapter 3. Membrane Analysis for Peninsula Blister Geometry

3.1 Introduction

The peninsula blister geometry was introduced by Dillard *et al.* (1990, 1991) as a modification of the island blister geometry. Energy release rates for the plate solution, no-prestress membrane solution, dominant prestress membrane solutions, and initial slack membrane solution were derived (Dillard, 1990, 1991; Bao, 1992). The results from Dillard's study indicate that this test geometry is a truly constant energy release rate specimen over a relatively large test section. These solutions also show the possibility of obtaining high energy release rates by changing the peninsula width rather than increasing the pressure. Studies of both the island blister (Allen and Senturia 1988, 1989) and the peninsula blister (Dillard et al., 1990, 1991; and Bao, 1992) claim that these two geometries may be capable of debonding films and coatings without yielding or rupturing them. These claims were based on the fact that high energy release rates could be obtained at low pressures. However, the stress analysis of the island blister in Chapter 2 shows that the low pressure does not necessarily produce low stress in the specimen. Instead, the island blister specimen has a very localized high stress concentration near the edge of the island in addition to the stress singularity at the crack tip. The analysis in the chapter 2 also shows that the prestress should be properly determined to avoid large errors due to the misuse of no-prestress or dominant prestress solutions, which suggests that it is necessary to solve for the energy release rate by considering the actual magnitude of prestress.

In this chapter, the energy release rate of the peninsula blister with an arbitrary magnitude of prestress will be derived and compared with the two extreme solutions. The

range of where the two extreme solutions can apply will also be identified. A comparison of the standard, island, and peninsula blister geometries will also be made. Although it is possible to obtain the stress distribution using finite element analysis, the stresses near the debond front will not be solved in the current study. Instead, the magnitude of the stress near the debond front will be discussed in Chapters 5 and 6 by using the energy release rate obtained in this chapter and the so called "fracture efficiency parameter" of the peel tests. In order to derive the energy release rates for the peninsula blister specimen, the problem of a one-dimensional blister will be solved. The energy release rate of one-dimensional blister will be determined, although it will not be discussed in detail.

3.2 Mathematical Formulations and Solutions

3.2.1 One Dimensional Blister

The derivation of the governing equations for the one-dimensional blister which consists of a membrane bonded along two straight parallel edges as seen in Fig. 3.1 is similar to that of circular blister in Chapter 2. Considering only the plane strain case, we can find the constitutive equation as:

$$\overline{\sigma}_r = N_r / h = \frac{E}{1-\nu^2}\overline{\varepsilon}_r + \overline{\sigma}_0, \tag{3.1}$$

where

$\overline{\sigma}_0$ is the prestress in the membrane.

$\overline{\sigma}_r$ is the total meridian stress in the membrane and is the sum of the prestress and the stress due to the applied load.

$\overline{\varepsilon}_r$ is the meridian strain in the membrane caused by the applied load. It does not include the strain due to the prestress.

N_r is the meridian stress resultant,

E is the Young's modulus of the membrane,

ν is the Poisson's ratio of the membrane,

and h is the thickness of the membrane.

It should be noted that the prestress in Eq. (3.1) can be either a uniaxial or an equal biaxial prestress. The difference between the uniaxial and biaxial prestresses is in the relationship with the prestrain:

for uni-axial prestress and prestrain: $\bar{\sigma}_0 = \frac{E}{1-\nu^2}\bar{\varepsilon}_0,$ (3.2-1)

and for bi-axial prestress and prestrain $\bar{\sigma}_0 = \frac{E}{1-\nu}\bar{\varepsilon}_0.$ (3.2-2)

Strain and displacement relation is given by

$$\bar{\varepsilon}_r = \frac{d\bar{u}}{dr} + \frac{1}{2}\left(\frac{d\bar{w}}{dr}\right)^2, \tag{3.3}$$

where $\bar{u}$ is the displacement in the radial direction,

$\bar{w}$ is the displacement in the transverse direction,

r is the radial coordinate in a rectangular geometry.

The equilibrium equation in the meridian direction is

$$dN_r = 0, \tag{3.4-1}$$

and equilibrium equation in the direction normal to the meridian direction is

$$N_r \frac{d^2\bar{w}}{dr^2} = -p, \tag{3.4-2}$$

where p is the pressure.

It should be noted that during the derivation of the above equations, large displacement, small rotation and small strain assumptions have been made. By substituting constitutive and strain/displacement relations into the equilibrium equations and introducing the following nondimensional forms,

$$u = \frac{\bar{u}}{R}\left(\frac{pR}{Eh}\right)^{-2/3}, \tag{3.5-1}$$

$$w = \frac{\bar{w}}{R}\left(\frac{pR}{Eh}\right)^{-1/3}, \tag{3.5-2}$$

$$\sigma_0 = \frac{\bar{\sigma}_0}{E}\left(\frac{pR}{Eh}\right)^{-2/3}, \tag{3.5-3}$$

$$\sigma_r = \frac{\bar{\sigma}_r}{E}\left(\frac{pR}{Eh}\right)^{-2/3}, \tag{3.5-4}$$

and

$$x = \frac{r}{R}. \tag{3.5-5}$$

we can obtain the following two governing equations:

$$u_{,xx} + w_{,x} w_{,xx} = 0, \tag{3.6-1}$$

and

$$w_{,xx}\left(u_{,x} + \frac{1}{2} w_{,x}^2 + \sigma_0\right) = 0. \tag{3.6-2}$$

By imposing the boundary conditions of $w_{,x} = u = 0$ at $x=0$ and $w = u = 0$ at $x=1$, we can solve for w and u as

$$w(x) = \frac{c_1}{2}(x^2 - 1) \tag{3.7-1}$$

and

$$u(x) = -\frac{c_1^2}{6}x^3 + \frac{c_1^2}{6}x, \tag{3.7-2}$$

where c_1 can be solved from the following equation

$$c_1^3 + 6\sigma_0(1-\nu^2)c_1 + 6(1-\nu^2) = 0 \tag{3.8}$$

and is expressed as:

$$c_1 = \frac{-2\sigma_0(1-\nu^2)}{\left\{-3(1-\nu^2)+\left[9(1-\nu^2)^2+8\sigma_0^3(1-\nu^2)^3\right]^{1/2}\right\}^{1/3}} + \left\{-3(1-\nu^2)+\left[9(1-\nu^2)^2+8\sigma_0^3(1-\nu^2)^3\right]^{1/2}\right\}^{1/3} \tag{3.9-1}$$

It is found that in the case without prestress, $c_1 = -\left[6(1-\nu^2)\right]^{1/3}$. (3.9-2)

After the displacements, w(x) and u(x), are determined, we can easily find the nondimensional blister volume per unit length, B, and the nondimensional membrane stress, σ_r, given by:

$$B = 2\int_0^1 w dx = -\frac{2}{3}c_1 \tag{3.10}$$

and

$$\sigma_r = -\frac{1}{c_1}. \tag{3.11}$$

3.2.2 Energy Release Rates

One-Dimensional Blister Test

We can also find the volume per unit length and strain energy due to applied pressure per unit length as

$$\overline{V} = BR^2\left(\frac{pR}{Eh}\right)^{1/3}. \tag{3.12-1}$$

and

$$U = 2h\int_0^R \frac{\overline{\sigma}_r + \overline{\sigma}_0}{2}\overline{\varepsilon}_r dr \tag{3.12-2}$$

It should be noted that only the energy release rate due to the applied pressure is considered, since the initial strain energy due to the prestress is not released during the

debonding process. Because the initial strain energy is not considered, the relationship between the prestress and prestrain is not used and either the uniaxial or the biaxial prestress in the following derivations can be used.

After some algebra based on Eq. (3.12) and energy balance equation,

$$2G\delta A = p\delta\overline{V} - \delta U, \tag{3.13}$$

we can find the energy release rate:

$$G = \frac{(pR)^{4/3}}{2(Eh)^{1/3}}\left\{\frac{-2}{9}\left[7c_1 - 2\sigma_0\frac{dc_1}{d\sigma_0}\right] - \frac{1-\nu^2}{3}\left[7\left(\frac{1}{c_1^2} - \sigma_0^2\right) - 2\sigma_0\left(\frac{-2}{c_1^3}\frac{dc_1}{d\sigma_0} - 2\sigma_0\right)\right]\right\}. \tag{3.14}$$

It is worth noting that for the case without prestress, energy release rate can be expressed as

$$G = \frac{7}{12}\left[6(1-\nu^2)\right]^{1/3}\frac{(pR)^{4/3}}{(Eh)^{1/3}}. \tag{3.15}$$

Peninsula Blister Test

With the solution for the one-dimensional blister, we are able to derive the energy release rate for the peninsula blister (Fig. 2.4) in which the membrane has a prestress of arbitrary magnitude by using the following energy balance equation (Dillard *et al.* (1990)):

$$G = p\frac{\partial}{2b\partial\ell}\left[\ell\overline{V}_{debond} + (L-\ell)\overline{V}_{bonded}\right] - \frac{\partial}{2b\partial\ell}\left[\ell U_{debond} + (L-\ell)U_{bonded}\right]. \tag{3.16}$$

where

ℓ is the distance of debond front from peninsula tip,

L is the length of the peninsula,

and the subscripts "bonded" and "debond" denote the associated quantities in the bonded and debonded section, respectively.

Both $\overline{V}$ and U can be obtained using Eq. (3.12) by substituting R with $\frac{a_0 - b_0}{2}$ and a_0 for bonded and debonded cases, respectively.

The energy release rate is given by:

$$G = \frac{(pa_0)^{4/3}}{(Eh)^{1/3}} \left\{ \left[\frac{2^{-4/3} c_b (1-S)^{7/3} - c_d}{3S} \right] - \frac{1-\nu^2}{2S} \left[\frac{1}{c_d^2} - \sigma_{0d}^2 \right] - 2^{-4/3} (1-S)^{7/3} \left[\frac{1}{c_b^2} - \sigma_{0d}^2 \left(\frac{(1-S)}{2} \right)^{-4/3} \right] \right\} \tag{3.17}$$

where
$$S = \frac{b_0}{a_0}, \tag{3.18-1}$$

$$c_d = c_1(\sigma_0 = \sigma_{0d}), \tag{3.18-2}$$

$$c_b = c_1\left(\sigma_0 = \sigma_{0d} \left[\frac{2}{(1-S)} \right]^{2/3}\right), \tag{3.18-3}$$

and
$$\sigma_{0d} = \frac{\overline{\sigma}_0}{E} \left(\frac{pa_0}{Eh} \right)^{-2/3}. \tag{3.18-4}$$

In the case without prestress, the energy release rate is expressed as:

$$G = \frac{(pa_0)^{4/3}}{8(Eh)^{1/3}} \frac{\left[3(1-\nu^2)\right]^{1/3} \left[2^{4/3} - (1-S)^{7/3}\right]}{S} \tag{3.19}$$

3.3 Results and Discussions

Figure 3.2 illustrates the energy release rates versus nondimensional peninsula width in a peninsula blister test with different prestresses and a Poisson's ratio of 0.34. It is seen that the energy release rate increases as the peninsula width decreases. Very high energy release rate at low pressure can be obtained by decreasing the nondimensional peninsula width. Although the stress analysis in the peninsula blister is not available in the current

study, it will be shown in Chapters 4 and 5 that high energy release rates require high stresses near the debond front. Since the stresses away from the debond front would approach those found in the one-dimensional blister, we may conclude that the peninsula blister specimen has a high stress concentration near the debond front and low stresses in the rest of the specimen, which is very similar to the stress distribution found in the island blister specimen (Fig. 2.3). It is interesting to note that all lines with different nondimensional prestress have a slope of about -0.98, which suggests that the energy release rate is approximately inversely proportional to the nondimensional peninsula width.

Figure 3.3 illustrates the same data as in Fig. 3.2 with nondimensional prestress as the abscissa. It is seen that when the nondimensional prestress is smaller than 0.1, the energy release rate plateaus at the value of the no-prestress case.

From Figs. 3.2 and 3.3, it is seen that the calculation of the energy release rate of the peninsula blister specimen greatly depends on proper measurement of the prestress. Since it is common for one to use either the no-prestress or dominant prestress solutions to calculate the energy release rate, it is important to know the range when these limiting solutions may apply and the error one may encounter if one of these solutions is used. Figure 3.4 illustrates the percent error of energy release rates using the two extreme solutions compared with the one from Eq. (3.17). The nondimensional peninsula width is 0.16. Errors of at least 10% can be found for the no-prestress solution with a nondimensional prestress larger than 0.1 and for the dominant prestress solution with a nondimensional prestress smaller than 1.0. For the no-prestress solution, error larger than 100% will occur if the nondimensional prestress is larger than 0.8. Error larger than 100% is seen if the nondimensional prestress is smaller than 0.3 for the dominant prestress solution. The situation is further complicated by the fact that nondimensional prestress is a function of pressure, i.e., the error in determining the energy release rate depends on the applied pressure. So both pressure and prestress are needed if one is to evaluate the error based on the extreme solutions.

A comparison of energy release rates during the debonding process in the standard, island, and peninsula blister tests is shown in Fig. 3.5. Both standard and island blister specimens give an increasing energy release rate as the debond proceeds, which results in an unstable debonding process. The peninsula blister produces a constant energy release rate and therefore, a stable debonding process.

Figure 3.6 illustrates the size comparison for the three blister specimens to produce the same energy release rate under the same pressure. A typical nondimensional island radius is chosen as 0.05 and a typical nondimensional peninsula width of 0.1. Under these conditions, one needs the largest specimen to use the standard blister test. One may reduce the specimen size for the standard blister by increasing the pressure, however, better seals and more sophisticated equipment may be needed. Although the island blister has the smallest test area, it requires more specimens if a series of data is needed. The peninsula blister has a very long test area which allows one to perform several tests on one specimen.

3.4 Summary

The membrane solution for the one-dimensional blister was solved. Based on this solution, the energy release rates for the peninsula blister were derived. Very high energy release rate at low pressure was found by decreasing the size of the peninsula. In addition to the advantages of high and constant energy release rates compared to the standard and island, the size comparison also showed that the peninsula blister has the advantage of very long testing area with a relatively small specimen size.

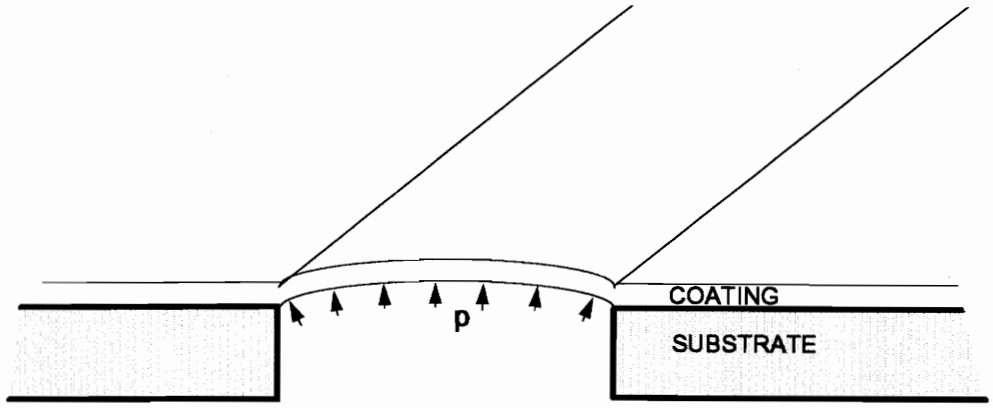

Figure 3.1 Illustration of a one-dimensional blister.

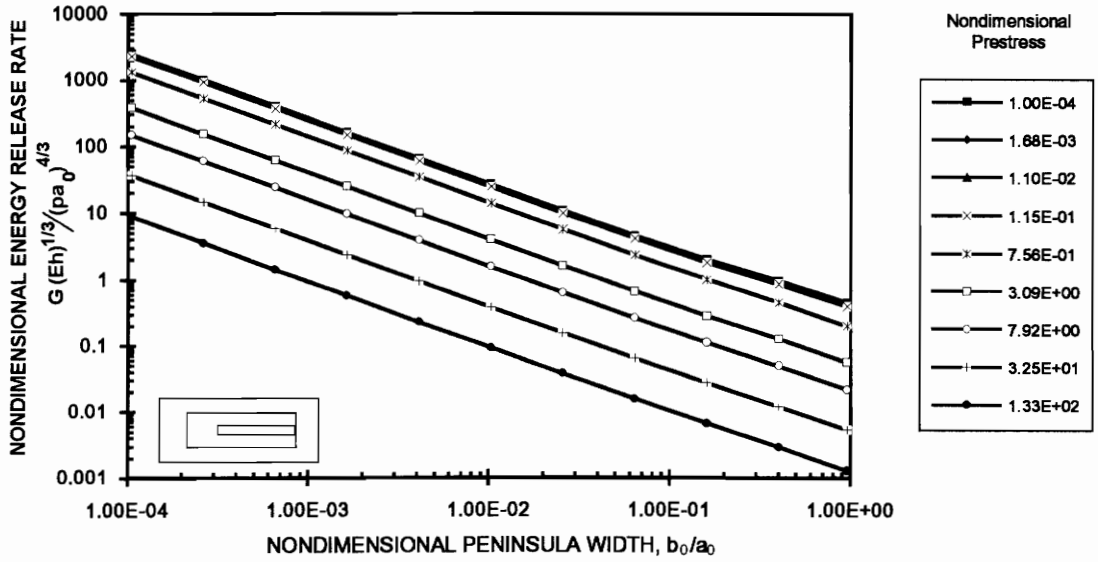

Figure 3.2 Energy release rates versus nondimensional peninsula width in a peninsula blister test with different prestresses and a Poisson's ratio of 0.34.

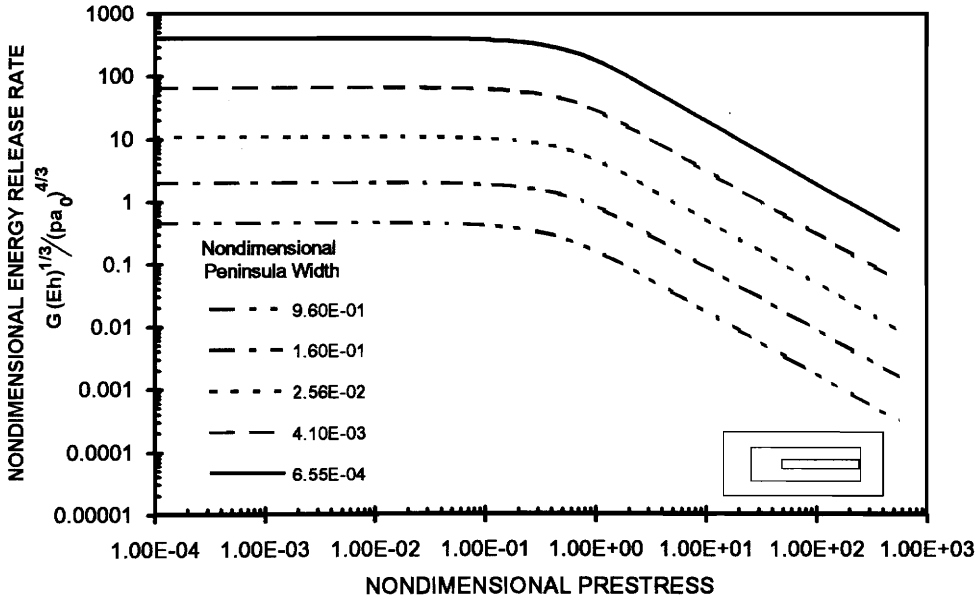

Figure 3.3 Energy release rates versus nondimensional prestress in a peninsula blister test with different nondimensional peninsula width and a Poisson's ratio of 0.34.

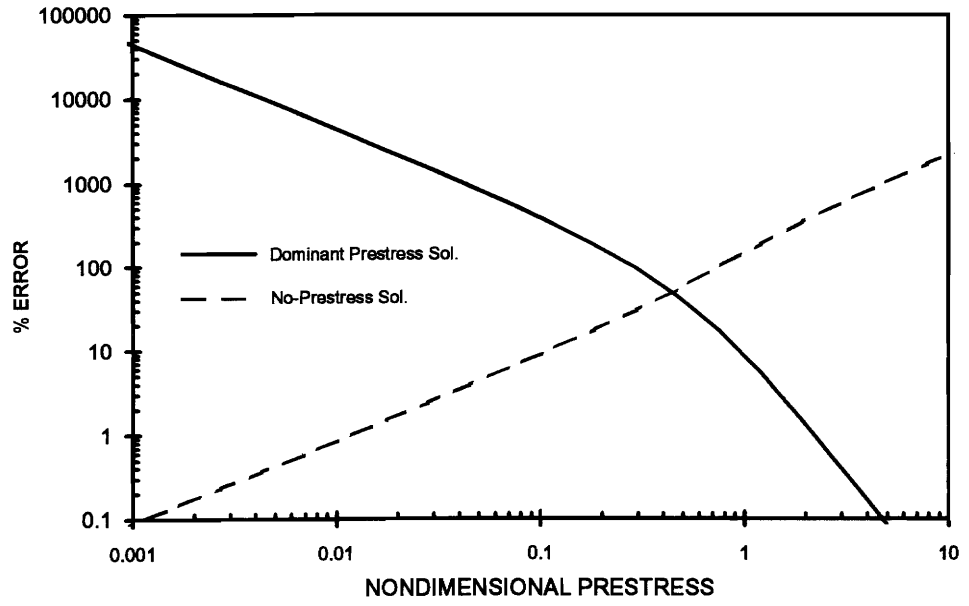

Figure 3.4 Percent error of energy release rates of two extreme solutions compared with the general prestress solution. Poisson's ratio is 0.34.

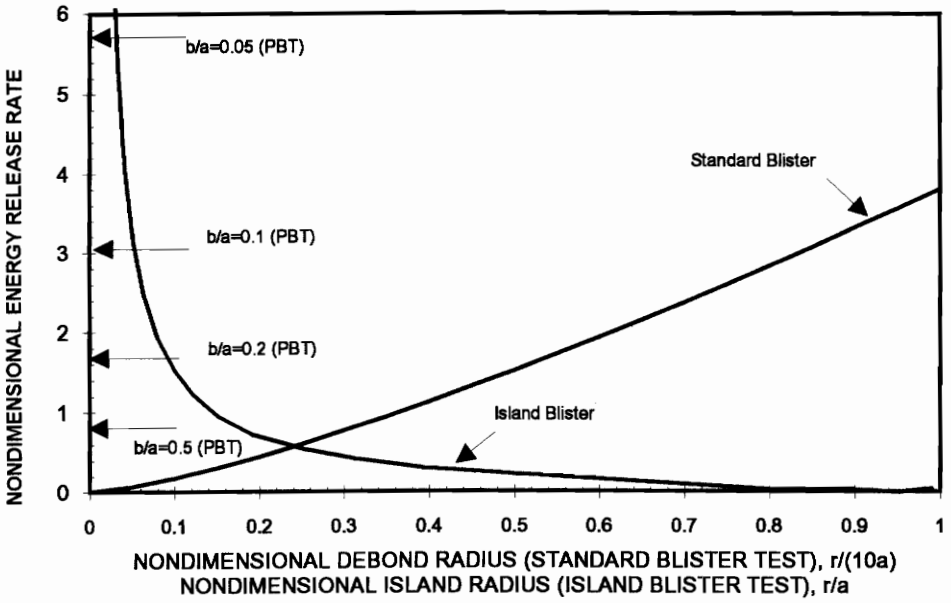

Figure 3.5 Comparison of energy release rates during the debond process in the standard, island, and peninsula blister tests.

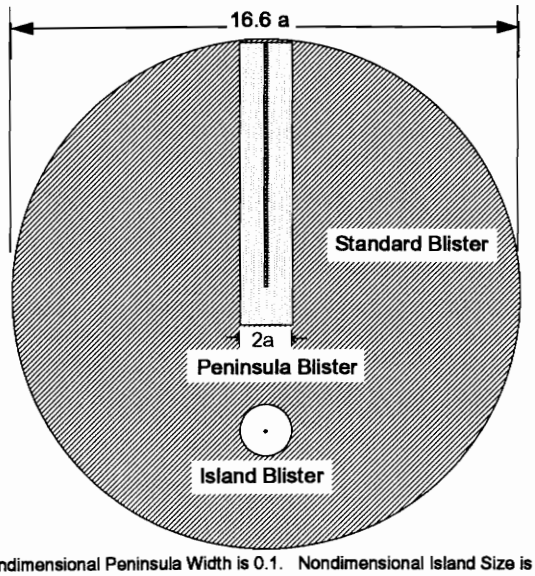

Figure 3.6 Size comparison for the three blister specimens to produce the same energy release rate under the same pressure.

Chapter 4. Comparison of Various Membrane Peeling Tests for Film Adhesion Measurement.

4.1 Introduction

The peel test (Fig. 4-1) is a mechanical test that has been extensively used to measure bond fracture strength of adhesive assemblies. In a peel test, a thin flexible strip that is bonded to a substrate by a layer of adhesive is pulled away at some angle to the underlying substrate. The force required to separate the adherend from the substrate, called the peel force, is related to the bond fracture strength and has been used to compare and develop adhesives, conduct quality control, and test surface preparation.

Spies (1953) was the first to present a theoretical analysis of the mechanics of elastic peeling. He considered 90^{o} peeling of a thin strip and represented the bonded part of the strip as an elastic beam on an elastic foundation and the flexible part as an elastica. Similar elastic models have also been presented by Bikerman (1957), Kaeble (1959, 1960), Jouwersma (1960), Yurenka (1962), Gardon (1963), Saubestre *et al.* (1965), Kendall (1973), Gent and Hamed (1975), and Nicholson (1977). In the absence of plastic/viscoelastic deformation, the peel force is a direct measure of the bond fracture strength. However, when plastic deformation takes place, one needs to consider the plastic dissipation and residual elastic strain energy that is left in the adherend to determine the bond fracture strength from an experimentally determined peel force. Several elastoplastic analyses of the peel test have been presented by Chang *et al.* (1972), Chen and Flavin (1972), and Gent and Hamed (1977). A numerical solution of the elastoplastic peel problem has been given by Crocombe and Adams (1981, 1982). Atkins and Mai (1986) found that the residual elastic strain energy during elastoplastic peeling is also an

important factor in determining the bond fracture strength. Kim and Aravas (1988) derived the moment-curvature relation for pure bending of an elastoplastic beam and related the experimentally measured peel force to the bond fracture strength. The analysis was later applied to thin metallic films. It was found that a bond fracture strength of 100 J/m^2 can be obtained for a fracture toughness of about 1 J/m^2 in for very thin copper films of 10 μm thick. By measuring the liberated heat during a peel test for polymeric films and metal substrate, Goldfarb (1991) and Farris (1992) found that the peel experiment for a polyimide/aluminum system overestimates the thermodynamic work of adhesion by at least 1200%. The mode mixity of various angle peel tests was investigated by Thouless and Jensen (1992) who found that the mode mixity is essentially constant except at very small peel angles.

Although the peel test offers a simple test geometry for measuring bond fracture strength, it suffers from several problems. The most severe one is that if the adherend is very thin, such as polyimide films of 1-10 μm thick, and adhesion is strong, the adherend may tear due to the high membrane/bending stresses or the high stress concentration at the grip. On the other hand, the blister test offers an attractive alternative because the loading method does not require mechanical contact and therefore, eliminates the stress concentration problem associated with gripping a peel specimen. In spite of the relatively large amount of literature for blister test geometries, few of them address the problems and limitations of this test category. Allen and Senturia (1988, 1989) noted that rupturing without debond occurs for polyimide films using the standard blister tests, but not the island blister test. Liechti and Liang (1992) found that the bursting was noticed in some blister specimens and that relatively high interfacial toughnesses were obtained from specimens that did not burst. They believed that yielding had occurred for those specimens that did not burst, thereby leading to high interfacial toughness.

Since the blister and peel specimens debond in a similar fashion, questions of how to differentiate between peel tests and blister tests at the region very near the debond front

were raised (Bao, 1992). In this chapter, a comparison of peel tests, blister tests and their variations will be made to clarify the similarities and differences of various membrane peeling tests.

4.2 Comparison Between the Peel Test and Pull-Off Test:

In this section, the peel test (Fig. 4.1) and its variation, the pull-off test (Gent, 1987), as shown in Fig. 4.2 are compared as an illustration of whether the same membrane peel stress and take-off angle at the debond front can have the same energy release rate under different far field loading conditions in a macroscopically different test geometry.

Peel Test

From the energy balance equation, the energy release rate of the peel test can be expressed as:

$$G = \frac{\delta W}{\delta A} - \frac{\delta U}{\delta A} \tag{4.1}$$

where

δA is the change of the debond area,

δW is the change of the external work,

and δU is the change of the strain energy,

The change of external work and strain energy can be expressed as:

$$\delta W = \bar{\sigma} h \left[\frac{\delta A}{1+\bar{\varepsilon}_0} - \delta A \cos\theta + \frac{\bar{\varepsilon}\delta A}{1+\bar{\varepsilon}_0} \right], \tag{4.2-1}$$

and

$$\delta U = \frac{h}{2\hat{E}} \left[\bar{\sigma}^2 - \bar{\sigma}_0^2 \right] \frac{\delta a}{1+\bar{\varepsilon}_0}. \tag{4.2-2}$$

where

$\hat{E} = \frac{E}{1-\nu^2}$ for the plane strain case,

$\hat{E} = E$ for the plane stress case,

$\bar{\sigma}$ is the applied membrane peel stress,

$\bar{\varepsilon}$ is the membrane peel strain,

and δa is the change of debonding length.

The relation between the equal biaxial prestress and prestrain in the plane strain case is:

$$\bar{\sigma}_0 = \frac{E}{1-\nu}\bar{\varepsilon}_0 \tag{4.3}$$

It should be noted that in Thouless' derivation (1992), only the uniaxial prestress-strain relation is considered, which may not apply in most film and coating problems. By substituting Eqs. (4.2) into Eq. (4.1), we can obtain the energy release rate as:

$$G = \bar{\sigma}h\left[1-\bar{\varepsilon}_0-\cos\theta+\bar{\varepsilon}-\bar{\varepsilon}_0\bar{\varepsilon}\right]-\frac{h}{2}\left[\bar{\sigma}+\bar{\sigma}_0\right]\left[(1-\bar{\varepsilon}_0)(\bar{\varepsilon}-\bar{\varepsilon}_0)\right]. \tag{4.4}$$

Assuming small strains in the membrane and then ignoring the higher order strain terms, the energy release rate can be obtained as:

$$G = \bar{\sigma}h\left[1+\bar{\varepsilon}-\bar{\varepsilon}_0-\cos\theta\right]-\frac{h}{2\hat{E}}\left[\bar{\sigma}^2-\bar{\sigma}_0^2\right]. \tag{4.5}$$

or

$$G = \bar{\sigma}h\left[1+\frac{1}{2\hat{E}}\bar{\sigma}-\frac{1}{\hat{E}}\bar{\sigma}_0-\cos\theta\right]+\frac{h}{2\hat{E}}\bar{\sigma}_0^2. \tag{4.6}$$

For the no-prestress case, Eq. (4.6) can be simplified as the familiar equation for the peel test:

$$G = \bar{\sigma}h\left(1+\frac{\bar{\sigma}}{2E}-\cos\theta\right). \tag{4.7}$$

Pull-Off Test

From Fig. (4.2) and considering the plane stress case for simplicity, we can easily find the following relations for a pull-off test:

$$2\bar{\sigma}hb\sin\theta = F \tag{4.8}$$

$$a^2 + y^2 = a^2\left[1+\bar{\sigma}/E\right]^2 \tag{4.9}$$

$$y/a = \tan\theta \tag{4.10}$$

where

b is the width of the specimen,

F is the pull-off force,

θ is the peel angle,

y is the out of plane displacement at the center of the membrane,

and a is half of the debonding length.

Assuming θ is small, neglecting the higher order strain terms, and performing some simple algebra, we can easily obtain the following relationship:

$$(\bar{\sigma} - \bar{\sigma}_0) = \theta^2 bE. \tag{4.11}$$

The change of the external work and strain energy can then be easily obtained as

$$dW = F\delta y = \frac{4\bar{\sigma}(\bar{\sigma} - \bar{\sigma}_0)h}{bE}\delta a \tag{4.12-1}$$

and

$$dU = \frac{(\bar{\sigma}^2 - \bar{\sigma}_0^2)h}{2bE}\delta a \tag{4.12-2}$$

Substituting Eqs. (4.12) into Eq.(4.1), the energy release rate at each end of the specimen can be obtained as

$$G = \frac{(3\bar{\sigma}^2 - 4\bar{\sigma}\bar{\sigma}_0 + \bar{\sigma}_0^2)h}{2E} \tag{4.13}$$

In a specimen without prestress, the energy release rate can be found to be:

$$G = \frac{3\bar{\sigma}^2 h}{2E} \tag{4.14}$$

Consistency between Peel Test and Pull-Off Test

Since the peel angle and membrane peel stress in a peel test can be chosen arbitrarily, we may choose the membrane peel stress and angle to be exactly the same as those in the pull-off test. Since the peel and pull-off tests of the same membrane peel stress and peel angle should give the same stress state in the specimen away from the point where the load is applied, therefore, they should produce the same stress intensity factor and the same energy release rate. The following section is to check the above argument:

From the pull test, we have the relation of

$$a(1+\bar{\varepsilon})\cos\theta = a \tag{4.15}$$

therefore,

$$\cos\theta = \frac{1}{1+\bar{\varepsilon}} = 1 - \bar{\varepsilon} + \frac{\bar{\varepsilon}^2}{2} - \ldots \tag{4.16}$$

Substituting the above relation into Eq.(4.7), we can obtain the energy release rate for the peel test with the same membrane peel stress and peel angle as the pull-off test:

$$G = \bar{\sigma}h(1 + \frac{\bar{\varepsilon}}{2} - 1 + \bar{\varepsilon} - \frac{\bar{\varepsilon}^2}{2} + \ldots) \tag{4.17}$$

Neglecting the higher order strain terms, we can obtain

$$G = \frac{3\bar{\sigma}^2 h}{2E} \tag{4.18}$$

which is exactly the same as that of the pull-off test.

This example suggests that in spite of the change of the test geometry and the applied load, the energy release rates remain the same as long as the membrane peel stress and peel angle remain the same. The above argument also suggests that tests with debonding mechanisms of peeling a membrane adherend from the substrate may have the same problems such as gross yielding as the peel test. One of the most significant test categories with similar debonding mechanism to the peel test is the family of blister tests. A comparison of the peel test with the blister tests is investigated in Sections 4.3 and 4.4. In Section 4.3, an idealized plane blister, the one-dimensional blister, is compared with the equivalent peel test. The comparison between circular blisters and plane strain peel tests are studied in Section 4.4.

4.3 Comparison between the Peel Test and One-Dimensional Blister Test

In the geometry of peel tests, a distance is required for the direction of the meridian stress to change from that of the applied membrane peel stress to that of the bonded surface. If the thickness of the membrane is infinitesimally small, this distance would approach zero. For the current comparison between the peel test and blister test for thin membranes, it is assumed that this distance is negligible in the one-dimensional blister geometry so that the meridian stress and take-off angle at the boundary could be chosen and used as the applied membrane peel stress and the peel angle in the equivalent peel test.

For simplicity, the plane stress version of the one-dimensional blister is considered. From Eq. (3.15), the energy release rate for the one-dimensional blister test can be expressed as:

$$G = \frac{7\bar{\sigma}^2 \mathrm{h}}{2\mathrm{E}} \tag{4.19}$$

From Eqs. (3.5-2), (3.7-1) and (3.11), the tangent of the membrane peel angle can easily be obtained as:

$$\tan\theta = (6\bar{\sigma}/E)^{1/2} \tag{4.20}$$

and the cosine of the membrane peel angle is given as

$$\cos\theta = (1+6\bar{\sigma}/E)^{-1/2} = 1-\frac{6\bar{\sigma}}{2E}+\frac{3}{8}\left(\frac{6\bar{\sigma}}{E}\right)^2-.... \tag{4.21}$$

Substituting the above equation into Eq.(4.7), we can obtain the energy release rate for the peel test with the same peel angle and membrane peel stress at the debond front as the one-dimensional blister test:

$$G=\frac{7\bar{\sigma}^2 h}{2E}, \tag{4.22}$$

The Eqs. (4.22) and (4.19) are exactly the same, which indicates that the one-dimensional blister test and peel test give the same energy release rate under the same membrane peel stress and peel angle despite the very different loading method and deformed shape of the specimens away from the debond front.

4.4 Comparison between the Peel Test and Circular Blister Tests

In the comparison of the pull-off/peel test and the one-dimensional blister/peel test, only the plane problem was considered. In order to compare the peel test and circular blister tests, we need to consider whether the results from a axisymmetrical membrane problem can be used in a plane strain membrane problem.

For a plane strain membrane problem, the stress state in the membrane is given by:

$$\bar{\sigma}_\eta = \nu\bar{\sigma}_\xi + (1-\nu)\bar{\sigma}_0. \tag{4.23}$$

where

ξ represents the meridian direction of the membrane,

and η represents the direction which lies on the membrane surface and is perpendicular to the meridian direction.

In an axisymmetrical problem, the meridian and circumferential stresses do not obey a simple relationship as in Eq. (4.23) except at the boundary. There the meridian and circumferential stresses obey a similar relationship:

$$\overline{\sigma}_\theta = \nu\overline{\sigma}_r + (1-\nu)\overline{\sigma}_0. \tag{4.24}$$

Eq. (4.24) holds for an axisymmetrical problem because the circumferential strain, ε_θ at the boundary is zero. In spite of the obvious difference between the solutions for the plane strain and axisymmetrical problems, these two problems should have the same stress state if the meridian stress and equal biaxial prestress in the axisymmetrical and plane strain problems are taken to be equal at the boundary.

Following the same argument made in Section 4.3, the distance for the direction of the meridian stress to change from that of the take-off angle at the debonded side to that of the bonded surface is assumed to be negligible. Since the stress state of an axisymmetrical membrane problem would approach that of a plane strain problem as the point of interest approaches the boundary from the membrane at the debonded side, the meridian stress and take-off angle at the boundary of the circular blisters could be taken as the applied membrane peel stress and peel angle in the equivalent peel tests.

The tangent of the take-off angle at the boundary for the circular blister is given by:

$$\tan\theta = \frac{d\overline{w}}{dr} = \frac{d\overline{w}}{Rdx} = \frac{dw}{dx}\left(\frac{pR}{Eh}\right)^{1/3} = m\left(\frac{pR}{Eh}\right)^{1/3}, \tag{4.25}$$

and the cosine of the take-off angle is given by:

$$\cos\theta = \frac{1}{\left[1+\frac{m^2\bar{\sigma}_r}{\sigma_r E}\right]^{1/2}} = 1-\frac{1}{2}\left(\frac{m^2\bar{\sigma}_r}{\sigma_r E}\right)+\frac{3}{8}\left(\frac{m^2\bar{\sigma}_r}{\sigma_r E}\right)^2-\ldots \tag{4.26}$$

It should be noted that the above quantities are evaluated at x=1 and x=a for the standard blister and island blister, respectively. By substituting Eq. (4.26) and membrane stress at the debond front into Eq. (4.7), we can obtain the energy release rate of the equivalent peel test which has the same peel angle and membrane peel stress as those at the debond front of the circular blister tests:

$$G = \bar{\sigma}_r h\left[1+\frac{(1-\nu^2)}{2E}\bar{\sigma}_r-\frac{(1-\nu^2)}{E}\bar{\sigma}_0-1+\frac{1}{2}\left(\frac{m^2\bar{\sigma}_r}{\sigma_r E}\right)-\frac{3}{8}\left(\frac{m^2\bar{\sigma}_r}{\sigma_r E}\right)^2+\ldots\right]+\frac{(1-\nu^2)h}{2E}\bar{\sigma}_0^2 \tag{4.27}$$

Assuming the strain is small, we may neglect the higher order terms in Eq. (4.27) and obtain the ratio between energy release rate and the square of the membrane stress at the debond front:

$$\frac{G}{\bar{\sigma}_r^2} = \frac{h}{E}\left[\frac{(1-\nu^2)}{2}+\frac{1}{2}\left(\frac{m^2}{\sigma_r}\right)-(1-\nu^2)\frac{\sigma_0}{\sigma_r}+\frac{(1-\nu^2)}{2}\frac{\sigma_0^2}{\sigma_r^2}\right]. \tag{4.28}$$

The reason for using this ratio will become apparent in Chapter 5 where the fracture efficiency parameter is defined. Since closed form solutions of the circular blister tests are not available, Eq. (4.28) will be represented numerically in the following discussions.

Figure 4.3 illustrates the energy release rate to the square of membrane peel stress ratio versus nondimensional prestress in a standard blister test. A typical Poisson's ratio of 0.3 is used. Excellent agreement is seen between the standard blister and peel tests. The ratio decreases as the prestress increases and is expected to approach zero when the prestress is very large. The results justify the earlier claims about the similarity of plane strain and axisymmetrical problems and the negligible distance for the direction of the

meridian stress to change from that of the take-off angle at the debonded side to that of the bonded surface.

Figure 4.4 illustrates the energy release rate to the square of membrane peel stress ratio versus nondimensional island radius in an island blister test with different nondimensional prestresses. The Poisson's ratio is 0.3. It is interesting to see that for the cases with small nondimensional prestress, such as the one with zero prestress in Fig. 4.4, the ratio increases as the island radius increases, while the ratio decreases for larger prestress cases. For the relatively large nondimensional prestress case, the ratio approaches zero as seen in the cases with nondimensional prestress of 3 and 8. Excellent agreements are seen between island blister test and peel tests for all prestresses and island radii.

4.5 Summary

In this chapter, the comparison based on the same membrane peel stress and membrane peel angle between the peel tests and other membrane peeling tests were made The results of the comparison between the peel test and the pull-off, the one-dimensional blister, the standard blister, or the island blister tests, suggested that in spite of different geometries and loading conditions, these different test geometries were special cases of peel tests of specific membrane peel stress and peel angle. The major difference between these tests and the peel test was that the applied membrane peel stress and peel angle can be applied independently in the peel test while these two quantities could not in the other tests. In the tests other than the peel test, the membrane peel stress and peel angle were determined for a given set of specimen dimensions, material properties and applied load. Therefore, peel tests can produce various energy release rates to the square of membrane peel stress ratios while the other test geometries can produce only one ratio once the specimen dimensions, material properties and applied loads are determined. In the case without prestress, the standard blister test had the highest ratio and the pull-off test had

the lowest among these tests excluding the peel test, which suggested that the standard blister test would have a lowest membrane peel stress and the pull-off test, the highest for a given energy release rate. The pull-off test would have a membrane peel stress 1.6 times as that in the standard blister test.

Although a comparison between the peel test and other blister geometries, such as the constrained blister and the peninsula blister, was not conducted in the present study, it is expected that these tests would also be special cases of the peel tests as found for the other membrane peeling tests.

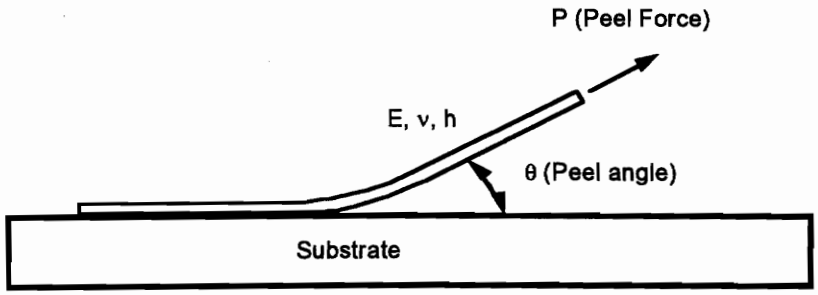

Figure 4.1 Illustration of a peel test.

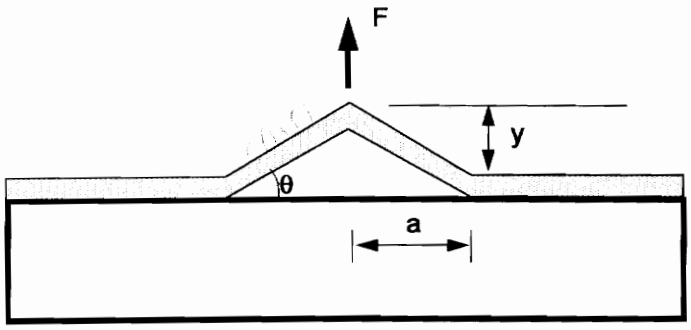

Figure 4.2 Illustration of a pull-off test.

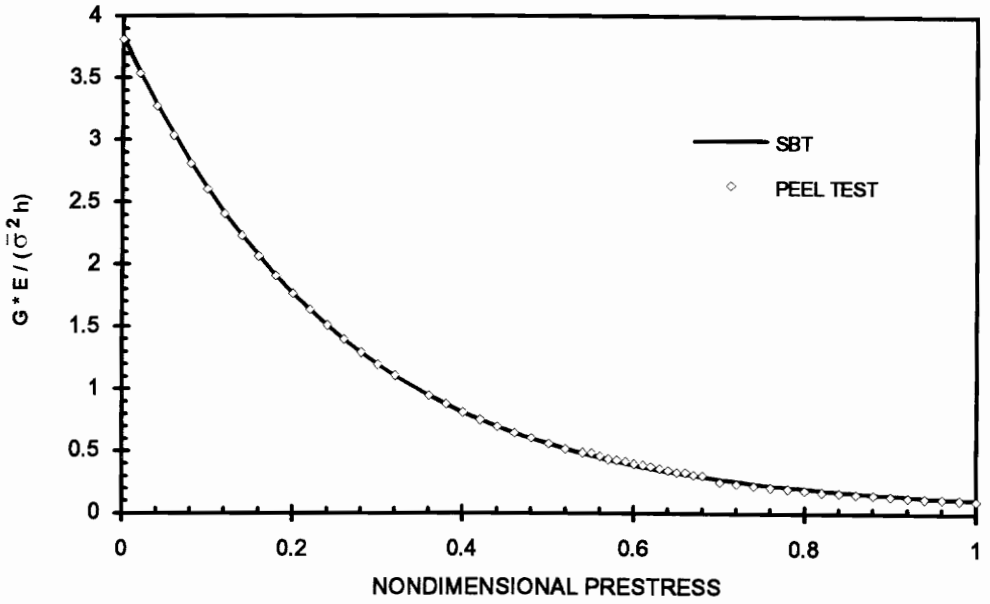

Figure 4.3 Energy release rate to the square of membrane peel stress ratio versus nondimensional prestress in a standard blister test. Poisson's ratio is 0.3.

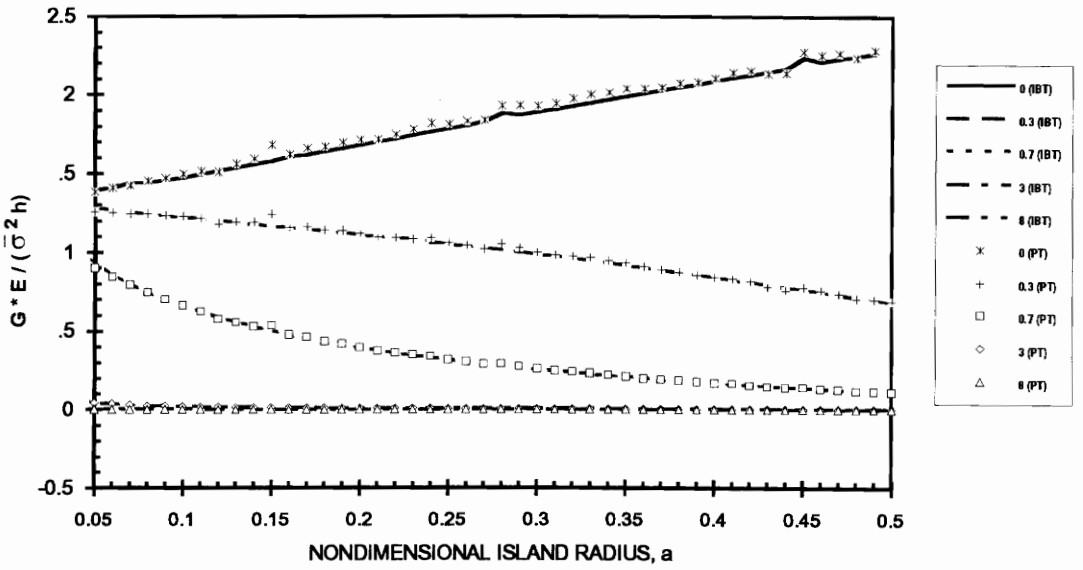

Figure 4.4 Energy release rate to the square of membrane peel stress ratio versus nondimensional island radius in an island blister test with different nondimensional prestresses. The Poisson's ratio is 0.3.

Chapter 5. Fracture Efficiency Parameter

5.1 Introduction

For any test measure the bond fracture strength of adhesively bonded joints, one important characteristic is the ability to debond the specimen without causing gross yielding in the adherends. Gross yielding in the adherends or films of a fracture specimen makes determination of bond fracture strength very complicated and difficult. The yielding problem is especially pronounced for specimens involving films and coatings because these specimens have relatively low load bearing capacity due to the small thickness. Therefore, measurement of bond fracture strength for films and coatings may require tests that are capable of producing high energy release rates at relatively low film stresses. Since fracture along the bond line and failure in the adherends of a bonded joint (including films and coatings) are subject to different criteria, it is necessary to study the relationship between the quantities associated with these two different criteria in the same specimen. Understanding this relationship, one might then design a testing method or choose proper specimen dimensions to avoid excessive yielding.

In an adhesively bonded joint, applied load, joint geometry, material properties, prestress, and specimen dimensions are the major factors determining the magnitude of applied energy release rate and stresses in the adherends. Before performing tests to determine the bond fracture strength of a specific material system, one needs to consider all the above factors and possibly optimize the tests to successfully debond the joint without yielding. In this chapter, a simple parameter called the "fracture efficiency parameter" will be defined and used to study the relation between bond failure and adherend (or film) failure. The parameter will applied to the general case of a bonded

system to investigate the possibility of designing a test geometry to achieve a higher "efficiency" than currently available test geometries.

5.2 The Fracture Efficiency Parameter

Within the framework of LEFM, the most commonly used quantity associated with the fracture criterion for adhesive assemblies is the energy release rate. To determine whether gross yielding will occur in the adherend or films, one needs to choose an appropriate quantity associated with yielding criteria for materials with various extent of ductility. For example, one may use the maximum principal stress in the maximum principal stress criterion for a brittle material, the maximum shear stress in the Tresca criterion for a ductile material, or the maximum effective stress in the Von Mises criterion for a moderately ductile material. During the test measurement, whether the specimen will debond or yield in the adherends depends on the magnitudes of two competing quantities - the energy release rate and maximum stress. The two quantities are related using a dimensional analysis similar to the one by Broek (1982). In this nondimensional analysis, the energy release rate is proportional to a strain energy release rate term and a length term and is given by

$$G = C^* \frac{\overline{\sigma}_{avg}^2 \lambda^*}{E^*} \tag{5.1}$$

where

$\overline{\sigma}_{avg}$ is the averaged applied stress.

E^* is a characteristic material modulus,

λ^* is a characteristic length,

and C^* is a nondimensional constant.

Two examples can demonstrate the use of Eq. (5.1). The first example considers a through-the-thickness mode I crack of length 2a in an infinite plate of modulus E. The plate is subjected to a tensile stress $\overline{\sigma}$ at infinity which is perpendicular to the crack orientation. In this classical crack problem, the characteristic modulus is E; the characteristic length is a; and the averaged applied stress is $\overline{\sigma}$. From Eq. (5.1), the energy release rate would be given by

$$G = C^* \frac{\overline{\sigma}^2 a}{E}. \tag{5.2-1}$$

This equation is identical to the energy release rate obtained from the elasticity (Broek, 1982), which is given by

$$G = \pi \frac{\overline{\sigma}^2 a}{E} \tag{5.2-2}$$

From Eqs. (5.2), C^* is π.

The second example considers a 0° peel test in which a film of thickness h and modulus E bonded to a rigid substrate is subjected to a peel stress of $\overline{\sigma}$. The film is assumed to be infinitely long and the crack is semi-infinitely long. In this interfacial crack problem, the characteristic modulus is E; the characteristic length is h; and the averaged applied stress is $\overline{\sigma}$. From Eq. (5.1), the energy release rate would be given by

$$G = C^* \frac{\overline{\sigma}^2 h}{E}. \tag{5.3-1}$$

Again, this equation is identical to the energy release rate obtained from Eq. (4.7) which was obtained from the energy balance equation. Eq. (4.7) gives an energy release rate as

$$G = \frac{1}{2} \frac{\overline{\sigma}^2 h}{E} \tag{5.3-2}$$

From Eqs. (5.3), C^* is 1/2.

The relationship between the average applied stress, $\overline{\sigma}_{avg}$, and the maximum stress, $\overline{\sigma}_{max}$, in the non-singular stress field is given by:

$$\overline{\sigma}_{max} = C_s \overline{\sigma}_{avg} \tag{5.4}$$

where C_s is the stress concentration factor and is a function of test geometry, material properties, specimen dimension, etc.

Weissberg and Arcan (1992) have shown that stress intensity factor is proportional to $C_s\overline{\sigma}_{avg}$. Therefore, Eq. (5.2) can be expressed as

$$G = C_e \frac{\overline{\sigma}_{max}^2 \lambda^*}{E^*} \tag{5.5}$$

where

$\overline{\sigma}_{max}$ is the maximum stress which can be the maximum tensile stress in the maximum principal stress criterion, maximum shear stress in the Tresca criterion, or maximum effective stress in the von Mises criterion and is dependent on the specimen geometry, material properties, and loading condition.

and C_e is a nondimensional coefficient which is given by

$$C_e = \frac{C^*}{C_s^2} \tag{5.6}$$

It should be noted that C_e is also a function of test geometry, material properties, specimen dimension, etc.

With the energy release rate/maximum stress relationship in Eq. (5.6), the quantity, $\frac{C_e \lambda^*}{E^*}$, which is the ratio between energy release rate and the square of maximum stress, can then be used to evaluate the "fracture efficiency" of a certain test geometry, or a test's

ability of producing a maximum energy release rate at a certain maximum stress level. This quantity is defined as "fracture efficiency parameter", T_e, and is expressed as:

$$T_e = \frac{G}{\bar{\sigma}_{max}^2} \tag{5.7}$$

For simplicity, the maximum tensile stress is used in the current study, which suggests that the results for this equation are more appropriate for brittle materials. It should be noted that the fracture efficiency parameter can be applied to more general materials by choosing an appropriate effective maximum stress. In the problem of films and coatings, it should be noted that the maximum stress is not the maximum membrane stress, but the maximum value of the sum of the bending stress and membrane stress.

With the fracture efficiency parameter defined, it is natural to define a critical fracture efficiency parameter as the ratio between the bond fracture strength and the square of the adherend strength,

$$T_e^c = \frac{\Gamma(\psi)}{\bar{\sigma}_{cr}^2}, \tag{5.8}$$

where $\Gamma(\psi)$ is the bond fracture strength.

From the study of fracture efficiency parameter and the critical fracture efficiency parameter, it is found that the ratio between the two parameter is an indication of whether a specific sample under a specific test geometry will results in debonding without adherend failure or in adherend failure before debonding. For convenience, the ratio between the fracture efficiency parameter and the critical fracture efficiency parameter can be called 'normalized fracture efficiency parameter' and expressed as

$$\bar{T}_e = \frac{T_e}{T_e^c} = C_e \frac{\lambda^*}{E^*} \frac{\bar{\sigma}_{cr}^2}{\Gamma}. \tag{5.9}$$

If the normalized fracture efficiency parameter is larger than one, then the specimen will debond without adherend yield/failure. Alternatively, if the normalized fracture

efficiency parameter is smaller than one, the specimen will cause adherend yield/failure before debonding. The normalized fracture efficiency parameter is useful both in designing the test and in evaluating the measured bond fracture strength value. For example, one may estimate the bond fracture strength and then design an appropriate specimen to obtain a normalized fracture efficiency parameter larger than one so that one may prevent yielding in the adherend. To evaluate whether the measured bond fracture toughness is reasonable, one may calculate the maximum bond fracture strength that can be measured without causing the adherend failure and compare it with the measured bond fracture strength. If the measured bond fracture strength is larger than the maximum bond fracture strength, the adherend failure such as yielding has occurred and the measured bond fracture strength may be in gross error. Therefore, one may need to calculate the bond fracture strength based considering the plastic deformation or redesign the specimen and redo the test.

5.3 Fracture Efficiency Parameter of the Membrane Peeling Tests

5.3.1 Mathematical Formulations

Using the definition in Eq. (5.7), the fracture efficiency parameter for some membrane peeling type test, such as the standard blister, island blister, and peel test can be derived as follows:

Standard Blister Test

The fracture efficiency parameter for the standard blister test in the case with and without prestress can be obtained from Eq. (2.17) and (2.18) for energy release rates and (2.31) for the nondimensional maximum stress and is given by:

$$T_e = \frac{h}{E\sigma_{max}^2}\left\{\frac{1}{\pi}\left[5B - \sigma_0\frac{\partial B}{\partial \sigma_0}\right] - \left(5B - \sigma_0\frac{\partial}{\partial \sigma_0}\right)\right.$$
$$\left.\int_0^1\left[\left((\sigma_r - \sigma_0)^2 - 2\nu(\sigma_r - \sigma_0)(\sigma_\theta - \sigma_0) + (\sigma_\theta - \sigma_0)^2\right) + 2(1-\nu)\sigma_0(\sigma_r + \sigma_\theta - 2\sigma_0)\right]x dx\right\}$$

(with prestress) (5.10)

and $$T_e = \frac{5}{4\pi}\frac{h}{E}\frac{B(\nu)}{\sigma_{max}^2(\nu)}, \quad \text{(without prestress)} \tag{5.11}$$

Note that B is the nondimensional blister volume and was given in Eq. (2.10-2).

Island Blister Test

The fracture efficiency parameters in the case with and without prestress can be obtained from Eqs. (2.19) and (2.21) for energy release rates and (2.31) for the nondimensional maximum stress and is given by:

$$T_e = \frac{\frac{1}{2}\frac{h}{E}\frac{1}{a}\left\{\frac{1}{\pi}\frac{\partial B}{\partial a} - \frac{\partial}{\partial a}\int_a^1\left[\left((\sigma_r - \sigma_0)^2 - 2\nu(\sigma_r - \sigma_0)(\sigma_\theta - \sigma_0) + (\sigma_\theta - \sigma_0)^2\right) + 2(1-\nu)\sigma_0(\sigma_r + \sigma_\theta - 2\sigma_0)\right]x dx\right\}}{\sigma_{max}^2(\nu, \sigma_0, a)}$$

(with prestress) (5.12)

and $$T_e = \frac{\frac{3}{8\pi}\frac{h}{E}\frac{1}{a}\frac{\partial B(\nu)}{\partial a}}{\sigma_{max}^2(\nu)}. \quad \text{(without prestress)} \tag{5.13}$$

Peel Test

Similarly, the fracture efficiency parameter for the peel test with uniaxial and biaxial prestrain can be obtained from Eqs. (5.4) and (2.31) and is given by

$$T_e = \frac{\bar{\varepsilon}(1 + \bar{\varepsilon} - \bar{\varepsilon}_0 - \cos\theta) - \left[\frac{\bar{\varepsilon}^2}{2} - \frac{\bar{\varepsilon}_0^2}{2}\right]}{\sigma_{max}^2}\frac{h}{\hat{E}} \quad \text{(uniaxial prestrain)} \tag{5.14}$$

and $$T_e = \frac{\bar{\varepsilon}(1+\bar{\varepsilon}-\frac{\bar{\varepsilon}_0}{(1-\nu)}-\cos\theta)-\left[\frac{\bar{\varepsilon}^2}{2}-\frac{\bar{\varepsilon}_0^2}{2(1-\nu)^2}\right]}{\sigma_{max}^2}\frac{h}{\hat{E}} \quad \text{(biaxial prestrain)} \qquad (5.15)$$

5.3.2 Comments about the Fracture Efficiency Parameter

Several comments about the fracture efficiency parameter can be made here:

(a) For all linear systems and some nonlinear systems such as membrane blisters without prestress, the fracture efficiency parameter is independent of the magnitude of the applied load. In some cases of nonlinear systems such as the peel, membrane blister with prestress, and cracked lap shear tests, the fracture efficiency parameter is only weakly dependent on the applied load through the nondimensional coefficient, C_e. The dependence of the fracture efficiency parameter of several nonlinear specimens on the applied load is discussed in Chapters 5 and 6. Because both the energy release rate and adherend (or film) stresses increase as the applied load increases, the independence or weak dependence of the fracture efficiency parameter on the applied load makes it an appropriate index to evaluate how a particular geometry/material system perform.

(b) For the standard blister specimen without prestress, the fracture efficiency parameter is independent of the radius of the blister; i.e., if the film yields without debonding at a specific radius, it will yield for any blister size although increasing radius can increase the energy release rate for a given pressure. The only way to avoid film yielding for a specific material is to increase the thickness of the film, since the fracture efficiency parameter is linearly proportional to the thickness.

(c) For blister specimens with prestress, the fracture efficiency parameter depends on the nondimensional prestress, σ_0. It should be noted that $\sigma_0 = \frac{\bar{\sigma}_0}{E}\left(\frac{pR}{Eh}\right)^{-2/3}$, so changing prestress, pressure, and outer blister radius can change the fracture efficiency parameter. Increasing pressure or blister radius has the same effect as decreasing

prestress. In this case, the fracture efficiency parameter is no longer linearly proportional to the film thickness due to the dependence on the nondimensional prestress. However, since the dependence of fracture efficiency parameter on the thickness through the nondimensional prestress is much weaker than the dependence on film thickness outside the bracket as shown in Eqs. (5.10) and (5.12), it is still approximately proportional to the thickness.

(d) As shown in Chapter 2, the island and the standard blister tests have about the same mode mixity. Thus when comparing the fracture efficiency parameter of these tests, the effect of the mode mixity will not be considered. However, the laminated beam specimens have a wide difference of mode mixity which can have a significant effect on the fracture efficiency parameter. Therefore, the effect of the mode mixity on the fracture efficiency parameter will be studied and discussed in Section 5.4.

5.3.3 Results and Discussions

Figure 5.1 illustrates the nondimensional fracture efficiency parameter versus peel angle for peel tests in plane stress with various peel strains. The nondimensional fracture efficiency parameter for the coating problem is conveniently expressed by

$$T_e \frac{E}{h} \tag{5.16}$$

The residual strain is zero in this case. For all applied peel strains, the nondimensional fracture efficiency parameters decrease significantly at very small angles and then increase slightly as the peel angle changes from zero to 180o. The most observation in this figure may be that all fracture efficiency parameters are nearly constant and equal for a large range of peel angles (10°-180°). The results suggest that the peel specimen is less likely to yield at very small peel angles or large peel angles. Since peel tests of very small angles are not commonly used, the difference in the fracture efficiency parameter is almost negligible in the peel tests with commonly used peel angles such as 90° and 180°. Except

for very small peel angles, the fracture efficiency parameter is rather insensitive to the applied strain. Although one may feel that it is "easier" to peel a specimen at a higher angle since the force needed is smaller, the bending moment at larger angle is larger and therefore, the maximum stress is about the same as the one in the test with smaller peel angle.

Figure 5.2 illustrates the phase angle versus peel angle for different peel strains. The prestress is zero. The results are the same as those of Thouless (1992). For the purpose of illustration, the materials are chosen so that the top adherend and bottom substrate have equivalent material properties. For all peel strains, the absolute value of phase angle decreases as the peel angle decreases, which suggests that mode II effect increases. It is seen that despite the significant change of the peel angle for smaller peel strain, the phase angle remains fairly constant for most peel angles. When the peel angle approaches zero, the phase angle switches signs, which suggests that the top adherend and bottom substrate contact each other. It should be noted that the phase angle simply switches signs instead of passing through zero.

In Fig. 5.2, the phase angle of a standard blister without prestress is also shown. The phase angle has a constant value of -52°, which is dependent of the applied pressure and specimen dimension. This result may appear to contradict that of the peel test (Fig. 5.1) despite that the similarity between the peel and standard blister tests have been shown in Chapter 4. However, one may maintain a constant phase angle in a peel test for any given peel angle if the applied peel strain is chosen appropriately when the specimen has no prestress. In a standard blister test, both membrane peel stress and peel angle decrease as the applied pressure decreases. The constant phase angle suggests that the relationship between the membrane peel stress and peel angle in a standard blister test without prestress for any given applied pressure is equivalent to automatically controlling the peel stress and peel angle in a peel test in such way that phase angle can be maintained at a constant value.

Figure 5.3 illustrates the nondimensional fracture efficiency parameter versus nondimensional prestress in a standard blister test with a Poisson's ratio of 0.3. The fracture efficiency of the standard blister test decreases as the nondimensional prestress increases. Since decreasing the nondimensional prestress is equivalent to increasing the blister radius, the results in Fig. 5.3 suggest that once debond of a blister can be initiated without yielding, it would do so at larger debond radii. This is in contrast to the case without prestress, where the fracture efficiency parameter is independent of the debond radius.

Figure 5.4 illustrates the nondimensional fracture efficiency parameter versus nondimensional island radius in an island blister test with various nondimensional prestress. A Poisson's ratio of 0.3 is also used. The results are quite different for the cases with different prestresses. An nearly constant fracture efficiency parameter is seen for the case without prestress at all island radius. As the prestress increases, the fracture efficiency increases more significantly as the island radius decreases. The results suggest that if gross yielding occurs, the island radius needs to be decreased to have possible debond initiated without yielding the film. However, the effect of decreasing the island radius depends on the prestress in the membrane. For the cases with small prestresses, the variation may be so small that it is unlikely that changing the size of the island could prevent yielding in the specimens. The nondimensional fracture efficiency parameter for a standard blister test without prestress is found to be 0.118, which is very close to that found in the island blister test with different island radii shown in Fig. 5.4. The result of the case without prestress suggests that if films yield without debonding in the standard blister test, it will also be likely to do so in the island blister test even though the island blister test needs much lower pressure. It should be noted that the maximum stress used in the fracture efficiency parameter is not the maximum membrane stress, but the maximum sum of bending stress and membrane stress. It is interesting to see in Fig. 5.3 that increasing pressure and blister radius can increase the fracture efficiency of the standard blister test with prestress, while fracture efficiency parameter is independent of

pressure and blister radius for the case without prestress. From the phase angle study for the standard and island blister tests in Chapter 2, it is found that the phase angles are around -50° and has a difference less than 4% for the standard and island blister tests for the case with the same material properties for the top adherend and bottom substrate. Thus it is appropriate to directly compare the fracture efficiency parameter between the two tests without considering the effect of mode mixity. In order to compare the fracture efficiency parameter between the standard and island blister test, the same real prestress, rather than nondimensional prestress, should be determined for both tests. The procedure to find the equivalent nondimensional prestress for the standard blister test based on a nondimensional prestress of a island blister test is described briefly as follows.

From Eqs. (2.7-4) and (3.2) The equal biaxial prestrains in the island and the standard blister specimens are:

$$\bar{\varepsilon}_0^{ibt} = (1-\nu)\sigma_0^{ibt}\frac{(p_{ibt}R)^{2/3}}{(Eh)^{2/3}}, \tag{5.17}$$

and

$$\bar{\varepsilon}_0^{sbt} = (1-\nu)\sigma_0^{sbt}\frac{(p_{sbt}R)^{2/3}}{(Eh)^{2/3}}. \tag{5.18}$$

where superscripts and subscripts "sbt' and "ibt" denote the quantities associated with the standard blister and island blister tests, respectively.

If the specimens with the same prestress is used in both tests, then we can find the relation of pressures needed for both tests to achieve the same energy release rate:

$$\frac{(p_{sbt})^{2/3}}{(p_{ibt})^{2/3}} = \frac{\sigma_0^{ibt}}{\sigma_0^{sbt}}. \tag{5.19}$$

Assume that the conditions of the island blister test are known and the island blister test and the standard blister test have the same outer radius, thickness, material properties, and energy release rate when the island blister specimen is loaded with a pressure of p_{ibt} and standard blister specimen, p_{sbt}. By using the energy release rate results from the

island blister as seen in Fig. 2.14 and approximate energy release rate equation for the standard blister, Eq. (2.36), we can easily solve for the nondimensional prestress of the equivalent standard blister. It is found that the equivalent nondimensional prestress is 0.416 for the standard blister test to achieve the same energy release rate as that in a island blister test in the case of an island blister test with a nondimensional prestress of 0.7 and nondimensional island size of 0.1. It can be seen from Figs. 5.3 and 5.4 that the standard blister test has a nondimensional fracture efficiency parameter of 0.075, while island blister test, 0.072. The results suggest that it is unlikely to induce yielding in one test geometry without inducing yielding in the other, which is indeed what was observed in Allen experiment (Allen, 1989). Allen also found that their specimens ruptured in the standard blister tests but not in the island blister tests after gross yielding in both tests. In order to predict rupture after yielding, elastic-plastic or plastic flow analysis is needed and awaits further study. The comparison of the fracture efficiency parameter is not capable of predicting rupture after gross yielding. To explain the experimental observation by Allen, we may find one possible explanation from the analytical solutions obtained in this study. Figures 2.7 and 2.12 indicate high membrane stresses throughout the standard blister specimen and low membrane stresses in the island blister specimen except for the high stress concentration at the edge of the island. From the view point of statistics, it is more likely to rupture the standard blister specimen than island blister specimen due to the high stress level throughout the standard blister specimen if the tensile stress limit of the membrane is not significantly higher than the maximum membrane stress in the standard blister.

In table 5.1, the normalized fracture efficiency parameter is used to examine whether gross yielding has occurred in some of the bond fracture strength measurement that can be found in the literature. Since not all material properties were found in the papers, some of the material properties were estimated from the other sources. It should be noted that C_e in the peel tests and blister tests are taken as 0.15 and 0.12, respectively, although it may be even smaller if considering the prestress in the coating. It is found that the normalized

fracture efficiency parameters are all smaller than 0.1, which suggests that yielding occurred in all cases and the measured bond fracture strength has been greatly overestimated. In the paper by Kim, et al (1989), the bond fracture strength corrected after considering the plastic energy dissipation is at least 1/60 of the measured apparent bond fracture strength. Goldfarb and Farris (1991) and Allen (1989) also reported evidence of plastic and viscoelastic deformation in their specimens, which also support that the normalized fracture efficiency parameter is smaller than one.

Table 5.1 Normalized fracture efficiency parameter in the literature.

Source	Test Method	Coating /Substrate	Coating Thickness (mm)	Apparent G (N/m)	Normalized T_e.	Yield?	E (GPa) Y (MPa)
Allen and Senturia, (1988)	Standard Blister	PI/Si	0.01	32	0.093	Yes	3 86.2
Allen and Senturia, (1989)	Island Blister	PI/Si	0.005	126	0.012	Yes	13 86.2
Kim, et al, (1989)	Peel Test	Cu/PI	0.077	303.8	0.0011	Yes	1.24 60
Kim, et al, (1989)	Peel Test	Cu/PI	0.015	509.5	0.00013	Yes	1.24 60
Gent and Lewandowski, (1987)	Standard Blister	Polypro-pylene/ Plexiglas	0.09	154	0.056	Yes	1.2 31
Gent and Lewandowski, (1987)	Peel Test	Polypro-pylene/ Plexiglas	0.09	228	0.048	Yes	1.2 31
Fernando and Kinloch, (1990)	Standard Blister	Photopo-lymer/ GFRP	0.03	140	0.037	Yes	2.41 58.6
Goldfarb and Farris, (1991)	Peel Test	PI/Al	0.063	660	0.0059	Yes	3 35
Goldfarb and Farris, (1991)	Peel Test	PI/Al	0.1	800	0.041	Yes	70 393

5.4 Fracture Efficiency Parameter of General Laminated Beam Specimens

Beam-type fracture specimens as described in Chapter 1 are the most frequently used specimens for composites, adhesively bonded joints, and other laminated materials. Most of these specimens of mixed mode I and II are special cases of layered materials with cracks between the two layers and with axial force and moment loaded along the edges of the layers (Fig. 5.5). For convenience, specimens of this general configuration are called general laminated beam specimens. For specimens with homogeneous, isotropic materials, the energy release rate has been obtained by Hutchinson and Suo (1992). The results can be summarized as:

$$G=\frac{1}{2\hat{E}_1}\left(\frac{P_1^2}{h}+12\frac{M_1^2}{h^3}\right)+\frac{1}{2\hat{E}_2}\left(\frac{P_2^2}{H}+12\frac{M_2^2}{H^3}-\frac{P_3^2}{Ah}-\frac{M_3^2}{IH^3}\right) \tag{5.20}$$

where

$$\Delta=\frac{1+2\Sigma\eta+\Sigma\eta^2}{2\eta(1+\Sigma\eta)}, \tag{5.21-1}$$

$$\Sigma=\frac{\hat{E}_1}{\hat{E}_2}, \tag{5.21-2}$$

$$\eta=\frac{h}{H}, \tag{5.21-3}$$

$$\hat{E}_1=\frac{E_1}{(1-\nu_1^2)}, \tag{5.21-4}$$

$$\hat{E}_2=\frac{E_2}{(1-\nu_2^2)}, \tag{5.21-5}$$

$$A=\frac{1}{\eta}+\Sigma, \tag{5.21-6}$$

and $$I = \Sigma\left[\left(\Delta - \frac{1}{\eta}\right)^2 - \left(\Delta - \frac{1}{\eta}\right) + \frac{1}{3}\right] + \frac{\Delta}{\eta}\left(\Delta - \frac{1}{\eta}\right) + \frac{1}{3\eta^3}. \quad (5.21\text{-}7)$$

Yielding may occur in the top adherend at the debonded section, bottom adherend at the debonded section, top adherend at the bonded section, and bottom adherend at the bonded section, which will be denoted as possible yielding sites 1, 2, 3, and 4, respectively, in the following discussion. The fracture efficiency parameter for this specimen will then be evaluated based on the site at which the maximum stress occurs. Although it is rare to find specimens which yields at site 3 or 4 before it yields at site 1 or 2, this study does find this situation which will be shown in Chapter 6.

Since elementary beam theory will be used, the maximum stress at the possible yielding site 1, is

$$\overline{\sigma}_{max,1} = \left|\frac{P_1}{h}\right| + \left|\frac{6M_1}{h^2}\right|. \quad (5.22\text{-}1)$$

Similarly, the maximum stress at the possible yielding site 2, is

$$\overline{\sigma}_{max,2} = \left|\frac{P_2}{H}\right| + \left|\frac{6M_2}{H^2}\right|, \quad (5.22\text{-}2)$$

At the site 3, the maximum stress is the larger of the two stresses at the upper surface and lower surface of the top adherend, which are respectively:

$$\overline{\sigma}_{max,3} = \left|\Sigma\left[\frac{P_3}{hA} + \frac{M_3(h + H - \Delta h)}{Ih^3}\right]\right| \quad (5.22\text{-}3)$$

or $$\overline{\sigma}_{max,3} = \left|\Sigma\left[\frac{P_3}{hA} + \frac{M_3(H - \Delta h)}{Ih^3}\right]\right| \quad (5.22\text{-}4)$$

Similarly at the site 4, the maximum stress is the larger stress at the upper surface and lower surface of the bottom adherend:

$$\overline{\sigma}_{max,4} = \left| \frac{P_3}{hA} - \frac{M_3 h}{Ih^3} \right| \tag{5.22-5}$$

or $$\overline{\sigma}_{max,4} = \left| \frac{P_3}{hA} - \frac{M_3 (H - \Delta h)}{Ih^3} \right| \tag{5.22-6}$$

It should be noted that P_3 and M_3 can be expressed in terms of P_1, P_2, M_1, and M_2 as

$$P_3 = P_1 - P_2 \tag{5.23-1}$$

and $$M_3 = M_1 - M_2 + P_1 (\frac{h}{2} + H - \Delta h) + P_2 (\Delta h - \frac{H}{2}). \tag{5.23-2}$$

By introducing the nondimensional terms:

$$\hat{R} = \frac{P_2}{P_1}, \tag{5.24-1}$$

$$\hat{S} = \frac{M_1}{P_1 h}, \tag{5.24-2}$$

$$\hat{T} = \frac{M_2}{P_1 h}, \tag{5.24-3}$$

$$A' = \frac{Ah}{h + H}, \tag{5.24-4}$$

and $$I' = \frac{Ih^3}{(h + H)^3}. \tag{5.24-5}$$

the energy release rates and maximum stresses at various possible yielding sites are

$$G = \frac{P_1^2}{2(\hat{E}_1 + \hat{E}_2)(h + H)} \left\{ \left(1 + \frac{1}{\Sigma}\right) \left[\left(1 + \frac{1}{\eta}\right) + 12\hat{S}^2 \left(1 + \frac{1}{\eta}\right)^3 \right] + (1 + \Sigma) \left[\hat{R}^2 (1 + \eta) \right.\right.$$
$$\left.\left. + 12\hat{T}^2 (1 + \eta)^3 - \frac{1}{A'} (1 - \hat{R})^2 - \frac{1}{I'} \left(\hat{S} - \hat{T} + \frac{(\eta + 2 - 2\Delta\eta)}{2(1 + \eta)} + \frac{\hat{R}(2\Delta\eta - 1)}{2(1 + \eta)} \right)^2 \right] \right\} \tag{5.25}$$

$$\overline{\sigma}_{max,1} = \frac{P_1}{(h+H)}\left[\left(1+\frac{1}{\eta}\right)+\left|6\hat{S}\right|\left(1+\frac{1}{\eta}\right)^2\right], \tag{5.26-1}$$

$$\overline{\sigma}_{max,2} = \frac{P_1}{(h+H)}\left[\hat{R}(1+\eta)+\left|6\hat{T}\right|(1+\eta)^2\right]. \tag{5.26-2}$$

$$\overline{\sigma}_{max,3} = \max\left(\frac{P_1}{h+H}\left|\Sigma\left[\frac{(1-\hat{R})}{A'}+\left(\hat{S}-\hat{T}+\frac{(\eta+2-2\Delta\eta)}{2(1+\eta)}+\frac{\hat{R}(\Delta\eta-2)}{1+\eta}\right)\left[1-\Delta(1+1/\eta)\right]\Big/I'\right]\right|,\right.$$
$$\left.\frac{P_1}{h+H}\left|\Sigma\left[\frac{(1-\hat{R})}{A'}+\left(\hat{S}-\hat{T}+\frac{(\eta+2-2\Delta\eta)}{2(1+\eta)}+\frac{\hat{R}(\Delta\eta-2)}{1+\eta}\right)\left[\frac{1}{1+\eta}-\Delta(1+1/\eta)\right]\Big/I'\right]\right|\right) \tag{5.26-3}$$

and

$$\overline{\sigma}_{max,4} = \max\left(\frac{P_1}{h+H}\left|\frac{(1-\hat{R})}{A'}-\left(\hat{S}-\hat{T}+\frac{(\eta+2-2\Delta\eta)}{2(1+\eta)}+\frac{\hat{R}(\Delta\eta-2)}{1+\eta}\right)(1+1/\eta)\Big/I'\right|,\right.$$
$$\left.\frac{P_1}{h+H}\left|\frac{(1-\hat{R})}{A'}-\left(\hat{S}-\hat{T}+\frac{(\eta+2-2\Delta\eta)}{2(1+\eta)}+\frac{\hat{R}(\Delta\eta-2)}{1+\eta}\right)\left[\frac{1}{1+\eta}-\Delta(1+1/\eta)\right]\Big/I'\right|\right) \tag{5.26-4}$$

where the subscripts 1, 2, 3, and 4 denotes the quantities associated with possible yielding sites 1, 2, 3, and 4.

The fracture efficiency parameter can be determined by taking the ratio between the energy release rate and the square of the maximum stress. There are four possibilities for the fracture efficiency parameter, T_{e1}, T_{e2}, T_{e3}, and T_{e4}. If the materials are the same for the top and bottom adherends, the smaller of the four quantities will be the fracture efficiency parameter of the specimen. To determine the fracture efficiency parameter when the upper and bottom adherends are made of the different materials, the ratios between the maximum stress to the failure stress of respective adherend should be determined and the maximum stress of the larger ratio should be used.

Results and Discussions

Figure 5.6 illustrates one category of the general laminated beam specimens - the coating problem. In this category, the bending rigidity and tensile rigidity of the bottom substrate are much larger than the coating. The problem is a general case of the membrane peeling problem. In a peel test or a blister test, the moment M_1 is dependent on the axial load, P_1. In this general problem, the applied loads, P_1 and M_1 are assumed to be applied independently. It should be noted that the results are applicable for the cases without prestress. However, the results for the cases with prestress can be easily obtained using the same procedure. The results in this figure cover all results of the membrane peeling test geometries. Nearly constant fracture efficiency parameters are seen for most nondimensional moments except near the zero moment where a peak is seen. The peak has a nondimensional fracture efficiency parameter of 0.5. It is interesting to see that the result is very similar to that of a peel test with different peel angles as shown in Fig. 5.1. The maximum fracture efficiency parameter can be achieved using the existing technique - peel test at a 0° peel angle. The results suggest that no matter how one modifies the geometry to improve the efficiency of a test for coating systems, the nondimensional fracture efficiency will be in the range of 0.15 and 0.5. Furthermore, since the fracture efficiency parameter decreases significantly when a small amount of bending moment is induced at the debond front, one may not be able to modify an existing test geometry such as a blister geometry to have very small moment and to achieve a nondimensional fracture efficiency parameter significantly larger than 0.15. The results of this figure further prove that it is unlikely for one to develop a high energy release rate test without inducing high stresses in the coating. To accurately measure the bond fracture strength with gross yielding or viscoelasticity in the specimen, one needs to develop new analytical solutions or experimental techniques to account for the plastic or viscoelastic dissipation in the specimen.

Figure 5.7 illustrates the nondimensional fracture efficiency parameter versus thickness ratio for three laminated specimens, double cantilever beam (DCB), end loaded split (ELS, see Fig. 5.8), and four point bend (FPB) specimens which have the same materials for the top and bottom adherends and are subjected to pure bending loads. The nondimensional fracture efficiency parameter for a laminated beam specimen can be expressed as:

$$T_e\left(\frac{\hat{E}_1+\hat{E}_2}{h+H}\right) \tag{5.27}$$

A double cantilever beam specimen has $M_1=M_2$. An end loaded split specimen has $M_1=-M_2$. Plane strain case is considered. A four point bend specimen has $M_2=0$. For the DCB and ELS specimens, the maximum efficiency is seen at the equal thickness case. The sharp peaks and kinks of lines represent the change of the yielding position from one adherend to another. The maximum fracture efficiency parameter for the FPB specimen occurs at a thickness ratio of 2. It should be noted from Eq. (5.10) that as more strain energy is stored in the bonded side of the specimen, the energy release rate becomes smaller. Although the ELS and the DCB specimen are subjected to the same magnitude of bending moment on the debonded side and have the same stresses on the debonded side, different loading conditions give the DCB specimen a higher energy release rate and therefore, a higher fracture efficiency parameter than the ELS specimen.

To compare the fracture efficiency parameter between test geometries of different mode mixity, the dependency of the fracture toughness on the mode mixity should be considered. A mixed mode fracture criterion proposed by Hutchinson and Suo (1992) may be used to illustrate the effect of mode mixity:

$$\Gamma(\psi)=G_I^c[1+\tan^2(1-\lambda)\psi], \tag{5.28}$$

where $\Gamma(\psi)$ is the interface toughness function,

G_I^c is the mode I toughness,

ψ is the phase angle,

and λ is a parameter that adjusts the influence of the mode II toughness.

It should be noted that the parameter λ adjusts the influence of the mode II contribution in the criterion and $\lambda =$ represents that the fracture is independent of mode mixity. The value of λ should be determined by experiment. According to this criterion, the critical fracture efficiency parameter can be expressed as:

$$T_e^c = \frac{\Gamma(\psi)}{\bar{\sigma}_{cr}^2} \tag{5.29}$$

where σ_{cr} is the tensile strength of the adherend. If a certain test geometry has higher fracture efficiency parameter than the critical fracture efficiency, debonding without yielding is likely to occur. To demonstrate the effect of mode mixity, four test geometries with significantly different mode mixity are discussed next. The test geometries considered are the double cantilever beam, the end loaded split, the four point bend, and the cracked lap shear specimens. The cracked lap shear specimen is assumed to be so long that the energy release rate and fracture efficiency parameter is independent of the boundary conditions. Further study on the cracked lap shear specimen can be found in Chapter 6. The fracture efficiency parameter and phase angles are shown in Fig. 5.8. The material properties and thicknesses of the upper and bottom adherend are assumed to be the same.

Figure 5.9 illustrates the ratio between the fracture efficiency parameter and critical fracture efficiency parameter for these four laminated beam specimens as a function of parameter λ. The ratio can be used to compare the fracture efficiency parameter among different test geometries with different mode mixity and to select the appropriate test geometry and thickness for measuring the adhesion of the adhesive bonds. The higher the ratio is, the most likely the test geometry is able to debond the specimen without causing adherend failure. Whether a certain test is capable of causing debond without causing

adherend failure depends on the value of $\frac{h}{E}\frac{\sigma_{cr}^2}{G_I^c}$. For example, to measure the fracture toughness of a specimen with a λ equal to 0.3, thickness should be adjusted so that $\frac{h}{E}\frac{\sigma_{cr}^2}{G_I^c}$ is larger than 3 for a double cantilever beam specimen, 8.9 for a four point bend specimen, 24.7 for a crack lap shear specimen and 19.41 for a end loaded split specimen. In other words, to achieve the same effective fracture efficiency parameter, the thickness of a crack lap shear specimen should be 8.2 times that of a double cantilever beam specimen.

So far in this section, results were reported for a limited number of laminated beam specimens. Because there are five independent variables in Eq. (5.27), it is very difficult to optimize the fracture efficiency parameter by finding five independent variables. Therefore, only limited ranges of five independent variables have been studied. Preliminary results suggest that the double cantilever beam specimen with equal adherend thickness and materials properties shown in Fig. 5.8 has the highest fracture efficiency parameter.

Figure 5.10 illustrates the comparison between a laminated beam specimen and a membrane peeling specimen. The laminated beam specimen is a beam bonded to a rigid substrate and is subjected to a bending moment. The test geometry has been used by Chang *et al.* (1972). The membrane peeling specimen is a standard blister specimen. For the purpose of illustration, polyimide is chosen as the material of the blister. The thickness is 10 mm. The material properties of the polyimide are taken from Modern Plastics Encyclopedia (1986). It is assumed that the same polyimide can be used as adhesive between the rigid substrate and top adherend which serves as the backing. The top adherend has a thickness of 1 mm. Various backing materials are examined.

To debond the specimen without yielding the adherend or film, the normalized fracture efficiency parameter has to be larger than one. For given material properties and specimen dimensions, one can determine a maximum bond fracture strength from Eq. (5.9)

so that the normalized fracture efficiency parameter is larger than one. In the standard blister tests, the maximum bond fracture strength is 4.3 N/m and 2.8 N/m for the cases with nondimensional prestresses of zero and 0.4, respectively. For the laminated beam specimen, the maximum bond fracture strength varies depending on the backing materials. Of all the laminated beam specimens in Fig. 5.10, the one with Titanium alloy, Ti-5, as the backing material has the highest maximum bond fracture strength of 842.1 N/m, while the one with copper, Cu, has the lowest maximum bond fracture strength of 4.3 N/m. From Eq. (5.9), an ideal baking material should be the one that has high yielding stress, large thickness, and low modulus. Since copper has a relatively low yielding stress and a relatively high modulus, it explains that the specimen with copper as backing material has such a low maximum bond fracture strength.

Since all membrane peeling tests have a similar fracture efficiency for a given thickness, it is useless to switch to another membrane peeling test when one yields. One possible way to increase the fracture efficiency of the membrane peeling test is to increase the membrane thickness. However, for many films, increasing film thickness significantly may not be practical. The result in Fig. 5.10 suggests that the film specimen with backing added may be a good alternative to the membrane peeling specimen.

5.5 Summary

In view of the recent interest in developing "high energy release rate" tests for film adhesion measurement, this chapter studied the relationship between the energy release rate and the maximum non-singular stress in adherends and films. The search for the appropriate criterion for the "high energy release rate" test led to the proposal and investigation of a simple parameter - the fracture efficiency parameter. Defined as the ratio between the energy release rate and the square of the maximum non-singular stress, the fracture efficiency parameter is an index of how much crack driving force a certain test geometry or specimen dimension can produce along the bondline for a given maximum

non-singular stress in the adherends. The fracture efficiency parameter was used to evaluate the performance, or the fracture efficiency, of a certain specimen design. Designing a test geometry or specimen based on the fracture efficiency parameter may prevent gross yielding in the adherend and therefore, prevent large error in determining the bond fracture strength. In addition to designing fracture specimens, the fracture efficiency parameter can also be used to evaluate whether the measured bond fracture strength is reasonable.

In this chapter, the fracture efficiency parameter was used to study the efficiency of the fracture tests among two categories, membrane peeling tests and laminated beam tests. It has been shown that to develop membrane peeling tests with high fracture efficiency for film adhesion measurement is unlikely. If the film yields before debonding in one test, it will likely to do so in another. Therefore, new experimental or analytical techniques considering the energy dissipation due to the inelastic deformation may be needed for film adhesion measurement. An alternative to the membrane peeling test in which the film yields is to add a backing material at the top of the film and test the specimen as a laminated beam specimen. The normalized fracture efficiency parameters based on the film adhesion measurement found in the literature also suggested that all these specimen might have been yielded. Some of the observations and calculations in the literature also supported this finding.

In comparing four laminated beam tests with different mode mixity, double cantilever beam was found to offer the highest fracture efficiency parameter. It was demonstrated in a typical example that the adherend thickness of a cracked lap shear specimen had to be about eight times the thickness in the double cantilever beam specimen in order to achieve the same efficiency. Although this chapter found limited opportunity for improving the fracture efficiency for films and coatings using membrane peeling tests, it showed that significant improvement in fracture efficiency could be achieved by using different test geometries or altering specimen dimensions.

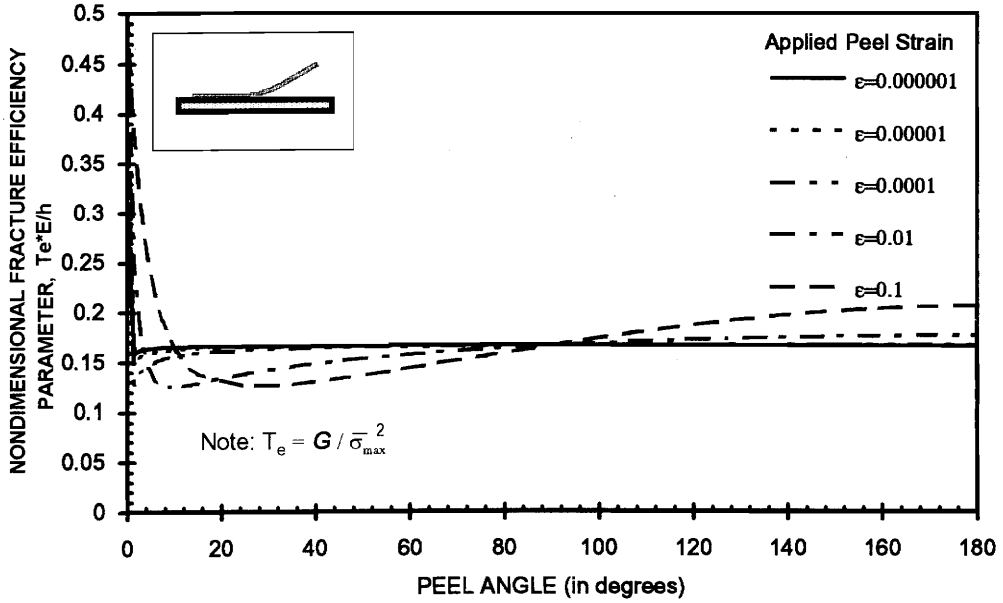

Figure 5.1 Nondimensional fracture efficiency parameter versus peel angle for peel tests in plane stress with various peel strains.

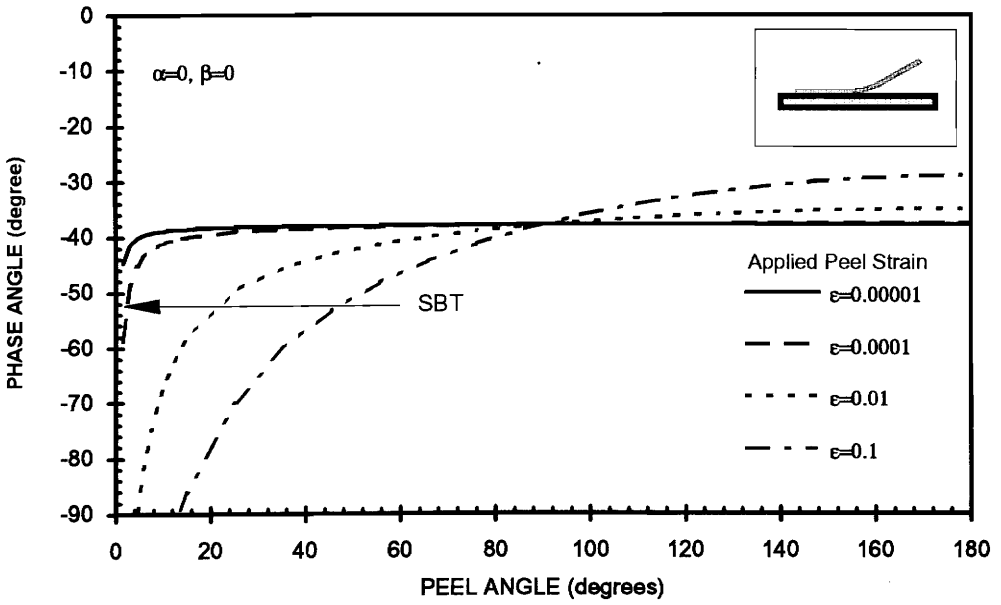

Figure 5.2 Phase angle versus peel angle for different peel strains in peel tests.

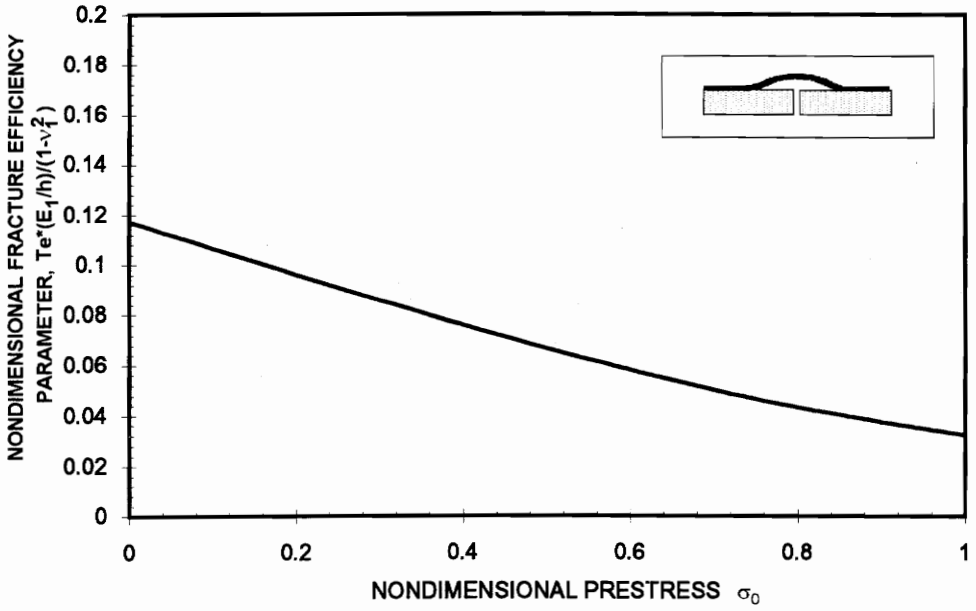

Figure 5.3 Nondimensional fracture efficiency parameter versus nondimensional prestress in a standard blister test with a Poisson's ratio of 0.3.

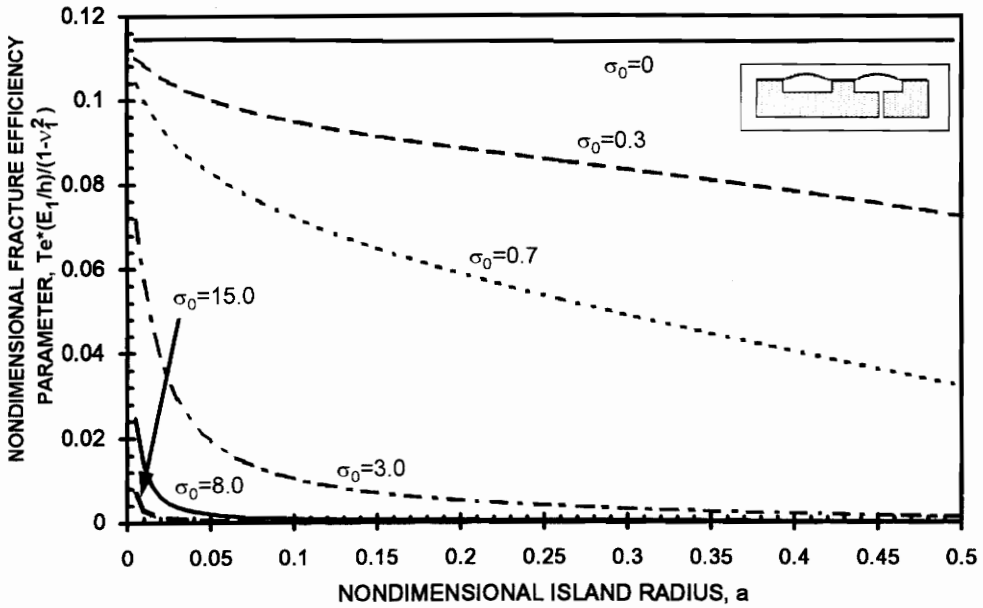

Figure 5.4 Nondimensional fracture efficiency parameter versus nondimensional island radius in an island blister test with various nondimensional prestress. Poisson's ratio is 0.3.

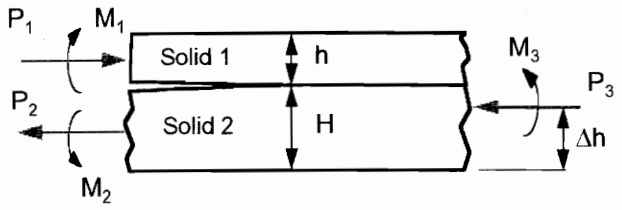

Figure 5.5 Illustration of a general bimaterial interfacial cracking problem.

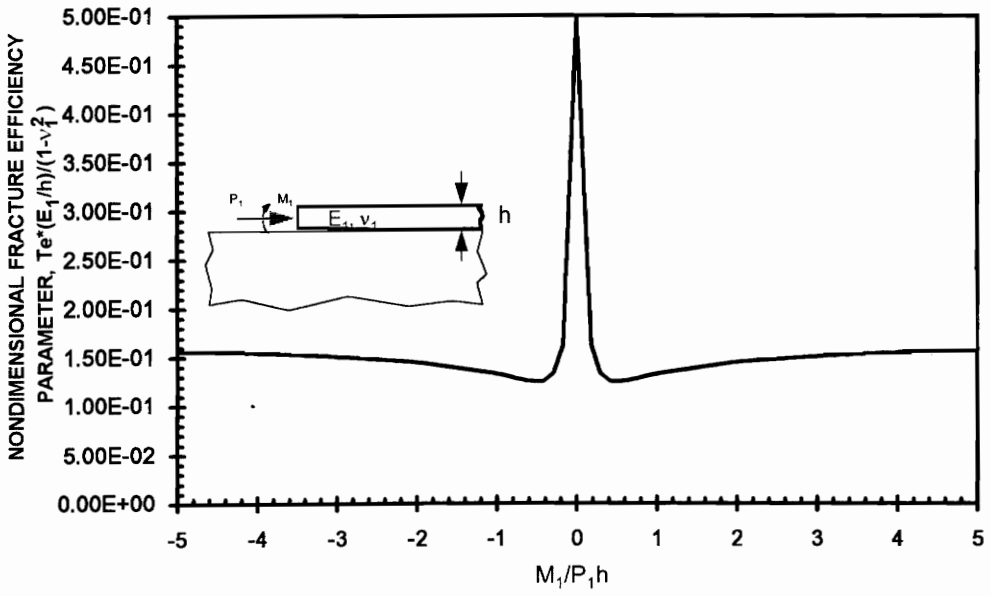

Figure 5.6 Nondimensional fracture efficiency parameter versus nondimensional moment for a general coating problem.

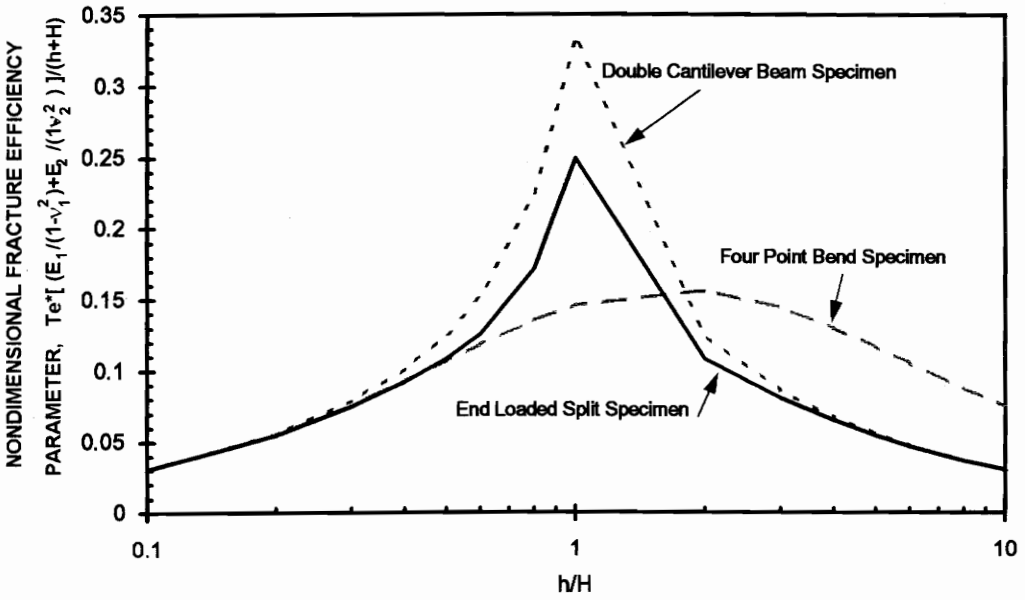

Figure 5.7 Nondimensional fracture efficiency parameter versus thickness ratio for double cantilever beam (DCB), end loaded split (ELS), and four point bend (FPB) specimens

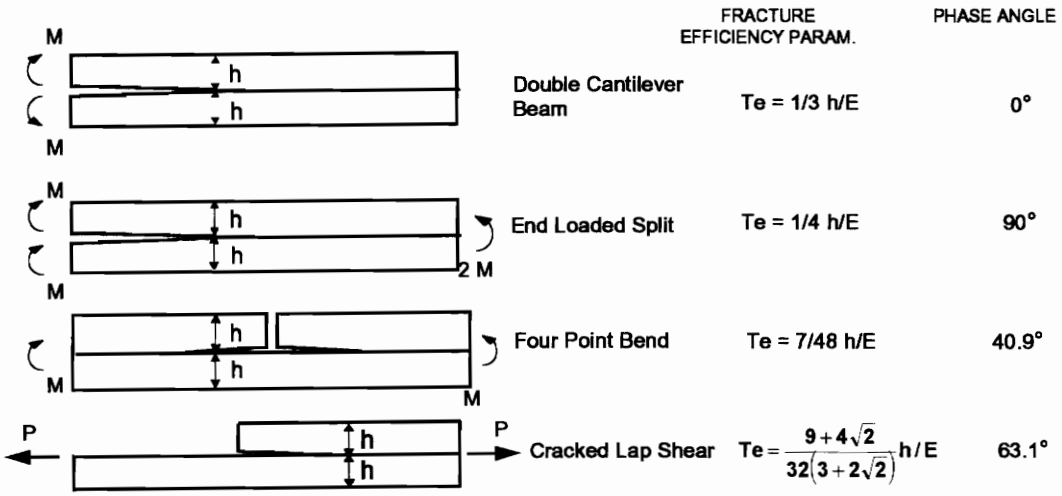

Figure 5.8 Illustration of four constant energy release rate, constant phase angle, and constant fracture efficiency parameter tests.

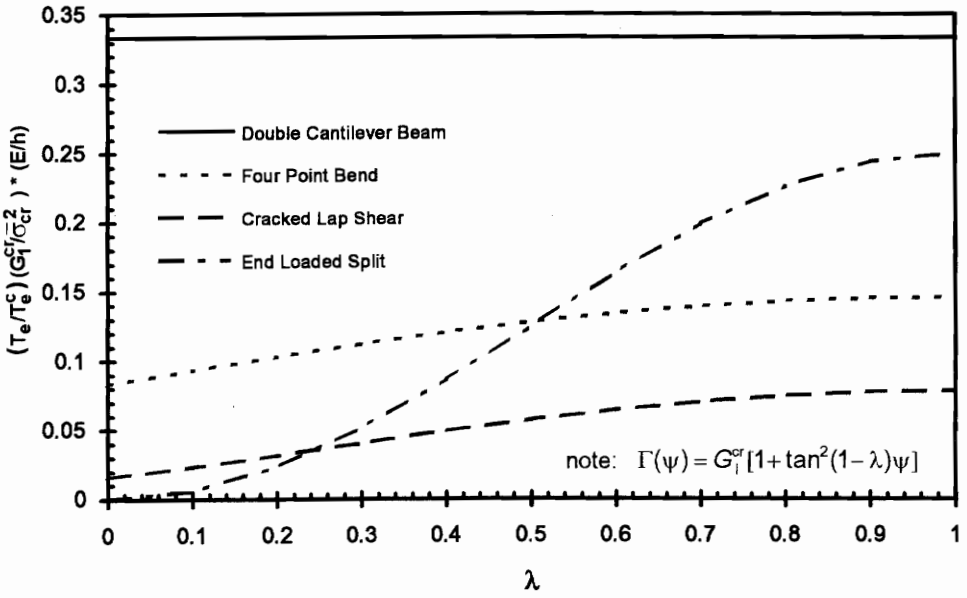

Figure 5.9 Ratio between the fracture efficiency parameter and critical fracture efficiency parameter for four typical laminated beam specimens with different parameter λ.

Prestress	N/A								$\sigma_0 = 0$	$\sigma_0 = 0.4$
$T_e = C_e$ h/E	$T_e = 0.15$ h/E								$T_e = 0.12$ h/E	$T_e = 0.077$ h/E
Thickness	h=1mm								h=0.01mm	h=0.01mm
Adhesive		Polyimide							Coating: Polyimide	
Backing	Cu	Steel (1050)	Al	Ti-5	EP	PE	PC	PI		
E (GPa)	12.4	21.0	7.0	11.6	2.4	3.0	2.4	2.1	2.1	
Y (MPa)	60	414	393	806	58.6	60	62	86	86	
Maximum Bond Fracture Strength w/o Yielding (J/m^2)	4.3	124	329	842	213	180	243	538	4.3	2.8

Al: Aluminum Alloy (2024-T6)
Ti-5: Titanium Alloy (Ti-5)
EP: Epoxy
PC: Polycarbonate
PE: Polyester
PI: Polyimide
Normalized Fracture Efficiency Parameter $\frac{T_e}{T_e^c} = \frac{C_e}{\Gamma}\frac{h\bar{\sigma}_y^2}{E}$

Figure 5.10 The comparison of maximum available bond fracture strength without gross yielding using laminated beam and standard blister specimens.

Chapter 6. The Cracked Lap Shear Specimen Revisited, A Closed Form Solution

6.1 Introduction

Shear loaded joints are widely used for adhesively bonded components. Due to the combination of peel and shear stresses, the fracture in a lap shear joint is often a mixed mode problem. To properly assess the mixed mode bond fracture strength of the lap shear joint, the cracked lap shear specimen was proposed by Brussat et al. (1977). The cracked lap shear specimen has been used to study adhesive joint debonding (Brussat *et al.*, (1977); Mall et al., (1984); Lin and Liechti, (1987); Schmueser and Johnson, (1990)) and composite delamination(Mall et al., (1987); Mall and Yun, (1987)). Although the geometry seems simple for testing, it has been found that the results was sensitive to the boundary conditions (Everett and Johnson, (1985); Lin and Liechti, (1987)). Furthermore, it was found that to properly determine the mode mixity and the energy release rate, geometrical nonlinearity of the specimen should be considered (Johnson, 1987). Although some analytical solutions have been derived, these solutions are useful for rather limited cases such as for an infinitely long specimen (Brussat et al., 1977) or for a specimen with the same thickness and material for lap and strap adherends (Edde and Verreman, 1992). The finite element method has been the most widely used tool to obtain the fracture parameters for cracked lap shear specimens. However, it is difficult to use nonlinear finite element analysis to investigate the effects of all the parameters involved in the cracked lap shear specimen and the behavior of this test geometry has not been fully understood. Therefore, a comprehensive analytical solution is needed for better analysis and design of the cracked lap shear specimen.

This chapter will revisit the cracked lap shear specimen and introduce a new nondimensional closed form solution based on a nonlinear beam-column approach. The energy release rate and mode mixity for the cracked lap shear specimens subjected to various boundary conditions will also be derived. The effects of the boundary conditions, specimen dimension, material properties, and loading will be discussed. The results will be used to design the specimen with constant energy release rate, constant mode mixity, and higher fracture efficiency. The solution will also be compared with the results of finite element analysis in the literature. Finally, the solution will be used to understand the anomalous debond history of a series of fatigue experiments using cracked lap shear specimens.

6.2 Mathematical Formulations

In this section, the deflections and bending moments in a cracked lap shear specimen will be determined using an approach similar to the one pioneered by Goland and Reissner (1944) for single lap joints.

The cracked lap shear specimen configuration analyzed is shown in Fig. 6.1. The thickness of the strap and lap adherends are h and H respectively. The material properties, Young's modulus E and Poisson's ratio ν, for the strap and lap adherend are denoted with subscripts 1 and 2, respectively. The specimen is loaded with a tensile load P at the left end of the strap. The total length of the specimen is L. The length from the left end of the strap to the crack tip is denoted ℓ_1. ℓ_0 denotes the length from the crack tip to the right end of the specimen. Following the Goland and Reissner approach, the adhesive layer is assumed to be so thin compared to the adherend thickness and so compliant compared to the adherend that it can be neglected. While the local stresses might change if this layer were included in the analysis, the energy release rate should not be greatly affected. Both

ends of the specimen are subjected to appropriate boundary conditions depending on the how the specimen is gripped in the experiment.

Figure 6.1(b) illustrates the plane passing through centroids of cross-section of the specimen and the coordinates of the problem. For convenience, two sets of coordinate systems (x_1, w_1) and (x_0, w_0) are introduced for the parts of the specimen to the left and right of the crack tip, respectively. w_1 and w_0 coordinates represent the transverse deflections of the specimen from the unloaded condition and are positive downward. The sign convention of the bending moment M, shear force V, and axial force P are shown in Fig. 6.1(c). In addition to the applied load, P, the reaction force, R_1, and reaction bending moment, m_1, may also exist at the left end of the specimen depending on the types of the boundary conditions. The specimen is considered as a plane problem so the forces and moments are averaged over the width of the specimen.

Using a "beam-column" approach similar to that used by Goland and Reissner (1944), we can set M_1 equal to the bending moment at position x_1 in the section at left side of the crack tip and M_0 equal to the moment in the bonded section at position x_0 from the crack tips, each per unit of width, then

$$M_1 = P(\alpha_n x_1 - w_1 + \frac{R_1}{P} x_1 + \frac{m_1}{P}) \tag{6.1-1}$$

$$M_0 = P\left[\alpha_n (x_0 + \ell_1) - w_0 - (\frac{h}{2} + H - \Delta h) + \frac{R_1}{P}(x_0 + \ell_1) + \frac{m_1}{P}\right] \tag{6.1-2}$$

where

Δh is the distance of the neutral axis of the bonded section from the bottom surface of the lap adherend.

Δ is a nondimensional quantity and can be expressed as

$$\Delta = \frac{1 + 2\Sigma\eta + \Sigma\eta^2}{2\eta(1 + \Sigma\eta)} \tag{6.2-1}$$

η is the thickness ratio of the strap to lap adherend:

$$\eta = h / H \tag{6.2-2}$$

Σ is the modulus ratio of the strap to lap adherends:

$$\Sigma = \frac{E_1 / (1 - \nu_1^2)}{E_2 / (1 - \nu_2^2)} = \frac{\hat{E}_1}{\hat{E}_2} \tag{6.2-3}$$

α_n represents the angle between the x_1 (or x_2) coordinates and the line of applied load (a'b'):

$$\alpha_n = (\frac{h}{2} + H - \Delta h) / L \tag{6.2-4}$$

According to the theory of thin, cylindrically bent plates, the differential equations for the transverse deflections, w_1 and w_0 are:

$$\frac{d^2 w_1}{dx_1^2} = -\frac{M_1}{D_1} = -\frac{P}{D_1}(\alpha_n x_1 - w_1 + \frac{R_1}{P} x_1 + \frac{m_1}{P}) \tag{6.3-1}$$

$$\frac{d^2 w_0}{dx_0^2} = -\frac{M_0}{D_0} = -\frac{P}{D_0}\left[\alpha_n (x_0 + \ell_1) - w_0 - (\frac{h}{2} + H - \Delta h) + \frac{R_1}{P}(x_0 + \ell_1) + \frac{m_1}{P}\right] \tag{6.3-2}$$

where D_1 and D_0 are the flexural rigidities of the strap adherend at the unbonded section and overlap joint section respectively.

Equations (6.3) have solutions of:

$$\frac{w_1}{L} = A_1 \cosh(\lambda_1 x_1) + B_1 \sinh(\lambda_1 x_1) + (\alpha_n + \hat{R}_1)\frac{x_1}{L} + \hat{m}_1 \tag{6.4-1}$$

$$\frac{w_0}{L} = A_0 \cosh(\lambda_0 x_0) + B_0 \sinh(\lambda_0 x_0) + \left[(\alpha_n + \hat{R}_1)\frac{(x_0 + \ell_1)}{L} - \alpha_n + \hat{m}_1\right] \tag{6.4-2}$$

where

$$\lambda_1 = \sqrt{\frac{P}{D_1}} \tag{6.5-1}$$

$$\lambda_0 = \sqrt{\frac{P}{D_0}} \tag{6.5-2}$$

$\hat{R}_1$ is the nondimensional reaction force:

$$\hat{R}_1 = \frac{R_1}{P} \tag{6.6}$$

$\hat{m}_1$ is the nondimensional reaction moment:

$$\hat{m}_1 = \frac{m_1}{PL} \tag{6.7}$$

The unknowns, A_1, B_1, A_0, B_0, $\hat{R}_1$ and $\hat{m}_1$ in Eqs. (6.4) can be solved by imposing appropriate boundary conditions. Three possible boundary condition configurations for the cracked lap shear test will be investigated in this study (Fig. 6.2) and are summarized below. The unknown constants determined for Cases A, B, and C are listed in Appendix A.

Case A. Roller-Roller Configuration

A roller boundary can be achieved by installing a shim to avoid bending during clamp-up. Four boundary conditions are found in this case in which the reaction force R_1 and moment m_1 are equal to zero. The four boundary conditions are:

at $x_1=0$, $\quad w_1 = 0$ (6.8-1)

at $x_1=t_1$, $x_0=0$ $\quad w_1 = w_0$ (6.8-2)

at $x_1=t_1$, $x_0=0$ $\quad \frac{dw_1}{dx_1} = \frac{dw_0}{dx_0}$ (6.8-3)

at $x_0=t_0$, $\quad w_0 = 0$ (6.8-4)

This configuration is equivalent to half of the single lap shear joint problem solved by Goland and Reissner (1944).

Case B. Roller-Clamped Configuration

In this case, the reaction moment m_1 is equal to zero and five boundary conditions can be found by solving for the five unknowns constants, A_1, B_1, A_0, B_0, and $\hat{R}_1$:

at $x_1=0$, $$w_1 = 0 \tag{6.9-1}$$

at $x_1=\ell_1$, $x_0=0$ $$w_1 = w_0 \tag{6.9-2}$$

at $x_1=\ell_1$, $x_0=0$ $$\frac{dw_1}{dx_1} = \frac{dw_0}{dx_0} \tag{6.9-3}$$

at $x_0=\ell_0$, $$w_0 = 0 \tag{6.9-4}$$

at $x_0=\ell_0$, $$\frac{dw_0}{dx_0} = 0 \tag{6.9-5}$$

Case C. Clamped-Clamped Configuration

In this case, six boundary conditions can be found by solving for the six unknowns constants, A_1, B_1, A_0, B_0, $\hat{R}_1$, and $\hat{m}_1$:

at $x_1=0$, $$w_1 = 0 \tag{6.10-1}$$

at $x_0=\ell_0$, $$\frac{dw_0}{dx_0} = 0 \tag{6.10-2}$$

at $x_1=\ell_1$, $x_0=0$ $$w_1 = w_0 \tag{6.10-3}$$

at $x_1=\ell_1$, $x_0=0$ $$\frac{dw_1}{dx_1} = \frac{dw_0}{dx_0} \tag{6.10-4}$$

at $x_0=\ell_0$, $$w_0 = 0 \tag{6.10-5}$$

at $x_0=\ell_0$, $$\frac{dw_0}{dx_0} = 0 \tag{6.10-6}$$

After the unknown constants are determined, the bending moments in the specimen are readily evaluated. Since the bending moments at $x_1 = \ell_1^-$ and $x_0 = 0^+$ can be directly used to determine the energy release rate and mode mixity, as will be discussed in the next section, they are evaluated as:

$$\text{at } x_1 = \ell_1^-, \qquad M_1(\ell_1) = PL\left[-A_1 \cosh(\lambda_1 \ell_1) - B_1 \sinh(\lambda_1 \ell_1)\right] \tag{6.11-1}$$

$$\text{at } x_0 = 0^+, \qquad M_0(0) = PL\left[-A_2 - \hat{R}_1 \frac{\ell_1}{L}\right] \tag{6.11-2}$$

Figure 6.2 also shows the typical deformed shape of the neutral axis for different boundary conditions. The thickness and transverse deflection have been magnified by 10 and 150 times, respectively.

6.3 Energy Release Rate and Mode Mixity

Using the energy release rate and stress intensity factors derived by Suo and Hutchinson (1990) for an interfacial crack in a bilayer with each layer being homogeneous, isotropic, and linearly elastic, these fracture parameters in a cracked lap shear specimen can be determined.

The energy release rate is given by

$$G = \frac{1}{2\hat{E}_1}\left(\frac{P^2}{h} + 12\frac{M_1^2(\ell_1)}{h^3}\right) + \frac{1}{2\hat{E}_2}\left(-\frac{P^2}{Ah} - \frac{M_0^2(0)}{IH^3}\right), \tag{6.12}$$

where

$$\hat{E}_1 = \frac{E_1}{(1-\nu_1^2)}, \ \hat{E}_2 = \frac{E_2}{(1-\nu_2^2)}, \tag{6.13}$$

$$A = \frac{1}{\eta} + \Sigma, \text{ and } I = \Sigma\left[\left(\Delta - \frac{1}{\eta}\right)^2 - \left(\Delta - \frac{1}{\eta}\right) + \frac{1}{3}\right] + \frac{\Delta}{\eta}\left(\Delta - \frac{1}{\eta}\right) + \frac{1}{3\eta^3}. \tag{6.14}$$

The complex stress intensity factor is given by

$$K = K_I + iK_{II}$$
$$= h^{-i\varepsilon}\left(\frac{1-\alpha}{1-\beta^2}\right)^{1/2}\left(\frac{-P+C_1P-C_2M_0(0)/h}{\sqrt{2hU}} - ie^{i\gamma}\frac{M_1(\ell_1)-C_3M_0(0)}{\sqrt{2h^3V}}\right)e^{i\omega} \qquad (6.15)$$

where

α and β are Dundur's elastic mismatch parameters which are given by

$$\alpha = \frac{\hat{E}_1 - \hat{E}_2}{\hat{E}_1 + \hat{E}_2} \text{ and } \beta = \frac{1}{2}\frac{E_1(1-2\nu_2)/(1+\nu_1) - E_2(1-2\nu_1)/(1+\nu_2)}{E_1(1-\nu_2)/(1+\nu_1) + E_2(1-\nu_1)/(1+\nu_2)}, \qquad (6.16)$$

ε is a bimaterial constant: $\varepsilon = \frac{1}{2\pi}\ln\left(\frac{1-\beta}{1+\beta}\right)$. (6.17)

C_1, C_2, C_3, U, V and γ are geometric factors and are given by

$$C_1 = \frac{\Sigma}{A},\ C_2 = \frac{\Sigma}{I}\left(\frac{1}{\eta}+\frac{1}{2}-\Delta\right), \text{ and } C_1 = \frac{\Sigma}{12I}, \qquad (6.18\text{-}1)$$

and by

$$U = \frac{1}{1+\Sigma\eta(4+6\eta+3\eta^2)},\ V = \frac{1}{12(1+\Sigma\eta^3)}, \text{ and } \sin\gamma = 6\Sigma\eta^2(1+\eta)\sqrt{UV}, \qquad (6.18\text{-}2)$$

and the angle ω is a function of the Dundur's parameters and adherend thickness ratio, η. The tables of ω can be found in Suo and Hutchinson (1990).

The ratio between the mode I and mode II energy release rate which is called mode ratio in this chapter can then be expressed by

$$\frac{G_I}{G_{II}} = \frac{K_I^2}{K_{II}^2}. \qquad (6.19)$$

It should be noted that the relations in Eqs. (6.12) and (6.15) are based on the assumption the adhesive layer can be negligible because the thickness of the adhesive layer is very small compared with in-plane dimensions of the specimen and the modulus of the

adhesive is much small compared with those of the adherends. This assumption will be verified Section 6.3 where the results from the analytical solution and finite element analysis have excellent agreement. Because the adhesive layer is assumed to be negligible, the energy release rate and stress intensity factors in Eqs. (6.12) and (6.15) are macroscopic quantities. Although it can be proved that the macroscopic energy release rate is equal to the local energy release rate at the crack tip using a simple energy argument or application of the J-integral, the macroscopic stress intensity factors, are not always equal to the local stress intensity factors at the crack tip. The relation between the macroscopic and local stress intensity factors can be found in Suo and Hutchinson (1989) and Fleck el al (1991) for some cases.

As seen in Appendix A, the debond problem in a cracked lap shear specimen can be described by five nondimensional parameters: nondimensional axial load, $\hat{P} = \sqrt{\frac{P}{\hat{E}_1(h+H)}}$; nondimensional crack tip position, $q = \frac{\ell_1}{L}$; nondimensional strap thickness, $\kappa = \frac{h}{L}$; nondimensional adherend thickness ratio, $\eta = h / H$; and nondimensional adherend modulus ratio, $\Sigma = \frac{\hat{E}_1}{\hat{E}_2}$. With the above these quantities, the energy release rate can be rewritten as:

$$G = \frac{P^2}{2(\hat{E}_1 + \hat{E}_2)(h+H)}\left\{(1+\frac{1}{\Sigma})\left[(1+\frac{1}{\eta}) + 12\hat{M}_1^2(1+\frac{1}{\eta})^3\right] - (1+\Sigma)\left[\frac{(1+1/\eta)}{A} + \hat{M}_0^2\frac{(1+1/\eta)^3}{I}\right]\right\} \tag{6.20}$$

where

$\hat{M}_1$ and $\hat{M}_0$ are the nondimensional bending moments which are given by

$$\hat{M}_1 = \frac{M_1(\ell_1)}{P(h+H)} \text{ and } \hat{M}_0 = \frac{M_0(\ell_0)}{P(h+H)} \tag{6.21}$$

The quantity:

$$G\frac{(\hat{E}_1+\hat{E}_2)(h+H)}{P^2} \tag{6.22}$$

will be called the nondimensional energy release rate in this chapter.

Equation (6.20) can be used for the cracked lap shear specimen subjected to various boundary conditions. The effects of the boundary conditions on the energy release rate and mode mixity will be passed through the bending moments, $\hat{M}_1$ and $\hat{M}_0$.

For comparison purposes, it is interesting to note that the total energy release rate obtained by Brussat et al. (1977) for an extremely long specimen is given by

$$\begin{aligned} G &= \frac{P^2}{2\hat{E}_1 h}\left(1-\frac{\hat{E}_1 h}{\hat{E}_1 h+\hat{E}_2 H}\right) \\ &= \frac{P^2}{2(\hat{E}_1+\hat{E}_2)(h+H)}\left(1+\frac{1}{\Sigma}\right)\left(1+\frac{1}{\eta}\right)\left(1-\frac{\Sigma\eta}{\Sigma\eta+1}\right) \end{aligned} \tag{6.23}$$

It should be noted that energy release rate obtained from Eq. (6.23) is independent of the crack length. It can be used as a limiting case for extremely long specimens.

6.4 Results and Discussions

Although five nondimensional parameters are found in the solution, the authors do not attempt to explore every case with all the possible combinations of five parameters. Instead, typical parameters found in the literature and in the experiments will be used. The closed form solution may easily be evaluated for other configuration or material properties.

Figure 6.3 illustrates the nondimensional energy release rate versus the nondimensional position of the crack tip for various nondimensional strap thicknesses. The results of three sets of boundary condition are plotted in the same figure. In this case,

the strap and lap adherends are assumed to have the same thickness and material properties. The nondimensional applied load is taken as 0.01, which is similar to those found in the literature. The cases with clamped-clamped, roller-clamped, and roller-roller boundary conditions are denoted as (C-C), (R-C), and (R-R) in the legend list. Typical nondimensional strap thickness of 0.005 and 0.025 are used. The numbers can be taken from a specimen of 305 mm (12 inches) in length and 1.59 mm (1/16 inches) in the strap adherend thickness and a specimen of 254 mm (10 inches) in length and 6.35 mm (1/4 inches) in thickness, respectively. These dimensions are similar to those found in the literature. Three stages of crack growth can be seen in this figure. The first is when the crack tip moves away from the left end of the strap to a nondimensional position of about 0.2. The second stage is when the crack tip moves from a nondimensional position of about 0.2 to 0.7. The last stage is when crack moves from 0.7 toward the right end of the specimen. In the first stage, the energy release rate with the clamped end (C-C case) drop to about 15% of the initial value and the ones with the roller end (R-C and R-R cases) increase by about 400%. If the initial cracks are growing within in this region, the specimens are expected to have a significant change in debonding rate in a fatigue test. In the second stage, the energy release rates for the three cases of nondimensional strap thickness of 0.005 are nearly constant. The value is approximately equal to that found for an infinitely long specimen using Eq. (6.23). These results suggest that as the nondimensional strap thickness is reduced further, the strain energy release will converge toward this value and the specimen can have a larger testing window with only a small change in energy release rate. In the same region, the cases of clamped-clamped and roller-clamped boundary conditions with a nondimensional strap thickness of 0.025 have about a 25% variation of energy release rate. Larger variation in energy release rate during the debonding process is expected if the nondimensional strap thickness is increased more. In the last stage, a significant change in energy release rate is seen again for all cases.

From the results in Fig. 6.3, the energy release rate in the roller-roller case is the most sensitive to the nondimensional strap thickness, while the clamped-clamped case is the least sensitive. The results suggest that the clamped-clamped configuration is more applicable over a wider range of nondimensional strap adherend thickness. Fortunately, this is also most frequently encountered in experimental test fixtures. The effects of the applied load and material modulus can also be investigated through Fig. 6.3 since decreasing the nondimensional strap thickness has the same effect as decreasing the modulus or increasing the applied load as can be seen in the nondimensional form of the applied load in Eq. (A.1). The results suggest that if the whole specimen is more compliant, the effects of the boundary conditions would be less significant and the specimen would behave more like the infinitely long specimen. Due to the geometrically nonlinear effects, the compliance is also a function of load. When the load is larger, the specimen would appear more compliant.

Figure 6.4 illustrates the ratio of mode I to mode II energy release rates versus the nondimensional crack tip position for specimens with the same parameters found in the discussions of Fig. 6.3. The mode ratio trends parallel the discussion of the energy release rate. It is seen that the crack tip is predominately loaded in mode II.

Figure 6.5 illustrates the nondimensional fracture efficiency parameter versus the nondimensional crack tip position for the same problem discussed in Fig. 6.3. It is seen that the fracture efficiencies only vary slightly with crack growth in the central portion of the specimen for all cases. The results suggest that the fracture efficiency is somewhat insensitive to the boundary conditions over a reasonable testing region.

Figures 6.6 and 6.7 show the nondimensional energy release rate and nondimensional fracture efficiency parameter versus the nondimensional crack tip position, respectively, for cracked lap shear specimens with various thickness ratios and nondimensional strap thickness. For comparison purposes, three thickness ratios are chosen as 2, 1 and 0.5. The same material is used in the strap and lap adherends. In order

to compare the magnitudes of the energy release rate under the same applied load with different thickness ratios, the sum of the strap and lap adherend thickness is taken as a constant. The specimen lengths for all cases are also the same. The nondimensional strap thicknesses for different thickness ratios are adjusted accordingly. The nondimensional applied load is chosen as 0.01. Although only three cases are examined in Figs. 6.6 and 6.7, the results represent trends for a wider range of adherend thickness ratio.

In Fig. 6.6, it is seen that for all boundary conditions in the main testing region where the nondimensional crack tip position is between 0.2 and 0.7, the thickness ratio of 0.5 produces the highest energy release rate and the thickness ratio of 2 has the lowest of the three cases examined. However, it is more important to see that the thickness ratio of 0.5 has more variation in the energy release rate as the crack grows while the thickness of 2 remains nearly constant. Therefore, from the viewpoint of the experiment, it is preferred to use the strap thicker than the lap in order to have a stable crack growing test. In spite of the smaller energy release rate for the specimens with smaller thickness ratios, one could always increase the axial load to increase the energy release rate while maintaining the stable crack growing advantage using the smaller thickness ratio specimens. Although increasing the load will increase the adherend stress and may cause the specimen to yield, whether the specimens with different thickness ratios will yield without debonding should be investigated through the fracture efficiency parameter as plotted in Fig.6.7.

In Fig. 6.6, the results obtained from Eq. (6.23) for an infinitely long specimen are also plotted, which have values of 2, 1, and 0.5 for the cases of thickness ratio equal to 0.5, 1, and 2, respectively. These three straight lines can serve as the limiting energy release rates when the specimens are subjected to a very large load, or have very compliant materials in the adherends, or have very thin adherends, or are very long. It is again seen that the larger nondimensional strap adherend thickness produces a energy release rate closer to the infinitely long case.

The comparison of the nondimensional fracture efficiency parameters for different adherend thickness ratios are seen in Fig. 6.7. It is interesting to see that although the specimen with a smaller adherend thickness ratio produces higher energy release rates, it actually has a smaller fracture efficiency parameter due to the higher adherend stress. Therefore, the specimens with smaller adherend thickness ratio not only have the advantage of more stable growth but also have the advantage of higher fracture efficiency. It should be noted that unlike in a linear system in which the fracture efficiency parameter is independent of applied load, the fracture efficiency parameter of the cracked lap shear specimens depends on the applied load through the dependence of the nondimensional applied load. However, this dependency is much weaker than the dependency of the energy release rate or adherend stresses on the applied load as can be seen in Fig. 6.5 where the fracture efficiency parameters of different nondimensional strap adherend thickness, and therefore, different nondimensional applied load, are approximately the same in the test window.

Figure 6.8 illustrates the nondimensional energy release rate versus nondimensional position of the crack tip for various adherend modulus ratios. Similar results to those in Fig. 6.6 are seen in this figure. More constant energy release rates can be obtained by using the stiffer material for the strap adherend. The results are consistent with those of Fig. 6.6 in that the larger rigidity in strap adherend results in more constant but smaller energy release rate.

Comparison Between the Closed Form Solutions and Finite Element Analysis

In order to examine the accuracy of the closed form solutions derived in this study, numerous results of nonlinear finite element analysis were taken from the literature to compare with the closed form solutions. More detailed information of these problems adapted from the literature are provide in Appendix B. Table 6.1 has the summary of these information.

Table 6.1 Specimen summary of the finite element analysis.

Case	B.C.	Strap		Lap	
		(Material) (Modulus*)	(thickness) (length)	(Material) (Modulus*)	(thickness) (length)
I	R-C	aluminum 72.45 GPa	3.18 mm 305 mm	aluminum 72.45 GPa	6.35 mm 254 mm
II	R-C	aluminum 72.45 GPa	3.18 mm 305 mm	aluminum 72.45 GPa	3.18 mm 254 mm
III	R-C	aluminum 71.02 GPa	3.2 mm 254 mm	Gr/Ep 103.93 GPa	1.6 mm 203 mm
IV	R-C	Gr/Ep 131** GPa	2.0 mm 241.3 mm	Gr/Ep 131** GPa	2.0 mm 203.2 mm
V	C-C	aluminum 72 GPa	3.2 mm 250 mm	aluminum 72 GPa	3.2 mm 200 mm

* Young's modulus. ** Shear modulus.

The comparison of energy release rates between the closed form solution and various finite element analyses is shown in Fig. 6.9. Very good agreement is seen for all cases with roller-clamped boundary conditions. The deviation in the clamped-clamped case is larger, but still less than 17%. Since only one case of clamped-clamped boundary conditions was found in the literature, it is not clear why the error is larger than those found in the roller-clamped cases. Although the closed form solution gives the possible energy release rates as the crack grows from zero crack length to the full length of the lap, the longest crack length in all of the finite element analyses is less than 60% of the lap length. In Cases III and IV, the material properties in the fiber direction are used in Eq. (6.12) to determine the energy release rates, since the majority of strain energy is due to the stresses in the fiber direction of the composite adherends. Although Eq. (6.12) is based on the assumption that the adherends are made of isotropic materials, the results suggest that it is a good approximation for the current study of composite materials as long as the material properties in the fiber direction are used.

Figure 6.10 shows the mode ratio comparison between the analytical and finite element analysis. It should be noted that the mode ratio obtained from Eq. (6.15) is the

macroscopic mode ratio which is based on the assumption of a negligible adhesive layer. Since the adhesive layers were modeled in the finite element analysis, the mode ratios from the finite element analysis could be viewed as the local mode ratio. According to the work by Fleck *et al.* (1991), the macroscopic mode ratio could be equal to local mode ratio when three conditions are satisfied: the crack is located at the center of the bondline, both adherends have the same thickness, and both adherends are made of the same material. Relatively good agreement is seen between the analytical and finite element analysis for Case I in which the above three conditions are satisfied. However, why the agreement is not as good as that for the energy release rate is not fully understood. Larger deviation is seen for the case when the crack is not at the center of the bondline (Case V) and when the strap and lap adherends have unequal thickness (Case II). In order to obtain the local mode ratio for the Cases II and V, further study similar to that of Fleck's (1991) is needed. Larger deviation is also seen in Cases III and IV, when the composite material is used, as is expected, since Eq. (6.15) is only applicable for adherends of isotropic material.

The results in Figs. 6.9 and 6.10 show that the closed form solution for energy release rates compares quite well with the finite element analysis. The comparison of mode ratio does not have as good agreement as energy release rate for all cases due to the inherent difference between macroscopic and local mode ratios. Despite the larger errors found in the mode ratio compared to the local mode ratio, many researchers found that the cyclic debond growth rate correlated better with the total energy release rate than with either mode I or mode II energy release rate independently, (Mall et al., (1984); Mall et al., (1987); Lin and Liechti, (1987)). Therefore, it is more important to predict the total energy release rate accurately, which the current closed form solution can do.

Explanation of Anomalous Fatigue Crack Growth Data

In the discussions for Figs. 6.11 to 6.13, the closed form solution will be used to understand a anomalous crack growth behavior of cracked lap shear specimens used in a fatigue study prior to the current analytical investigation.

A typical crack growth history of a series of fatigue tests using the cracked lap shear specimens is seen in Fig. 6.11. The strap and lap adherends were made of steel and had a thickness of 2.54 mm and a width of 25.4 mm. The adhesive was an epoxy. The specimen had been conditioned for five and a half months in an environmentally controlled chamber with 99% relative humidity and 60°C. The specimen was clamped at both ends using hydraulic grips and was subjected to a 10Hz cyclic load between 6.674kN and 0.667 kN using an MTS load frame. The initial crack length measured from the edge of the lap adherend to the crack tip was 50 mm. The total specimen length between the grips was 210 mm. The length of the lap adherend less the gripped length was 195 mm. The crack was successfully initiated and grew for about 90 mm. However, the debonding rate decreased as the crack grew longer and nearly stopped at a crack length of 140 mm after about six-million cycles. After another five million cycles, the specimen showed very little crack growth.

Figure 6.12 illustrates the energy release rate versus crack length. It is seen that the energy release rate increases slightly and then decreases in the test windows found in the fatigue test. When the crack first starts to grow, the total energy release rate is about 31 N/m. When the crack stops growing, the total energy release rate has dropped below 25 N/m which is a 24% decrease from the initial value. By examining the mode ratio in Fig. 6.13, it is found that the mode ratio has changed from 0.26 to 0.22, which may not be significant enough to stop the crack growth. Therefore, it is suspected that the reason the crack stopped is because the applied energy release rate dropped below a possible

threshold value, 25 J/m^2. Indeed, after the maximum load was increased from 6.674 kN to 11.12 kN, the crack resumed growing as seen in Fig. 6.11.

6.5 Summary

The chapter reported a closed form, nondimensional, nonlinear solution for cracked lap shear specimens with three sets of possible boundary conditions. The solution was derived based on a beam-column approach. The fracture parameters such as the energy release rates and mode ratios were emphasized although the stress distribution along the bondline could have been obtained using an approach similar to that pioneered by Goland and Reissner (1944). The fracture parameters at various crack tip position were studied through five nondimensional parameters. In view of the sensitivity of energy release rates to the crack growth, the use of clamped-clamped boundary conditions is recommended. In order to obtain a more constant energy release rate test, the specimens should be designed so that the adherend thickness was small compared with the specimen length and the thicker or stiffer adherend should be used as the strap adherend. Although the use of a thinner strap adherend produced higher energy release rates at low loads, the fracture efficiency parameter is lower than if the thicker adherend is used as the strap. This example also served as an excellent example of how the fracture efficiency parameter can be used to design better specimens.

The fracture parameters obtained from the closed form solution were compared with those from the finite element analysis found in the literature. Very good agreement was found for all roller-clamped case. Although the mode ratio can be obtained from the closed form solution, it is a macroscopic mode ratio as in contrast to the local mode ratio found in the finite element analysis. When the crack was located at the center of the bondline and the strap and lap adherends are made of the same thickness and material, the mode ratio obtained from the analytical solution compared well with the ones from the finite element analyses. Further study is needed to determine the local mode ratio from the

information of the macroscopic mode ratio with different adherend thickness, material properties, and various crack locations in the bondline.

The closed form solution also gave a reasonable explanation of why the crack growth slowed down significantly after crack tip reached a specific position in a series of fatigue tests. It is believed that this type of problem could have been avoided by better design of the specimen dimensions using the solution presented in this chapter.

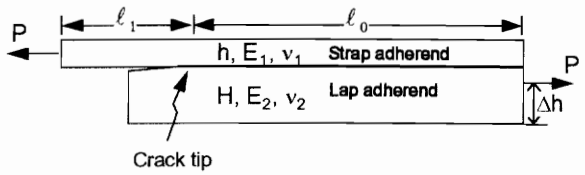

(a) Configuration of a cracked lap shear specimen.

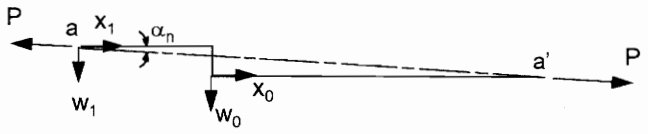

(b) Coordinate systems.

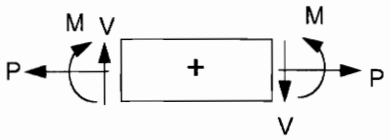

(c) Sign convention.

Figure 6.1 Illustration of the cracked lap shear configuration.

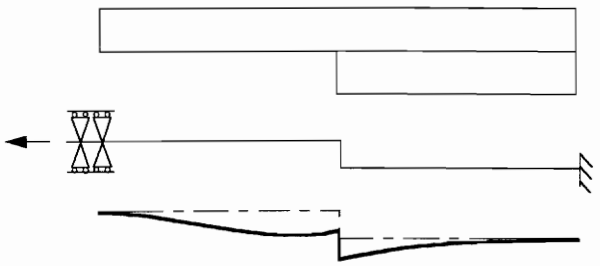

(a) Clamped-clamped B.C.

(b) Roller-clamped B.C.

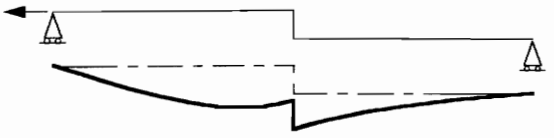

(c) Roller-roller B.C.

Figure 6.2 Three possible boundary condition configurations in cracked lap shear test

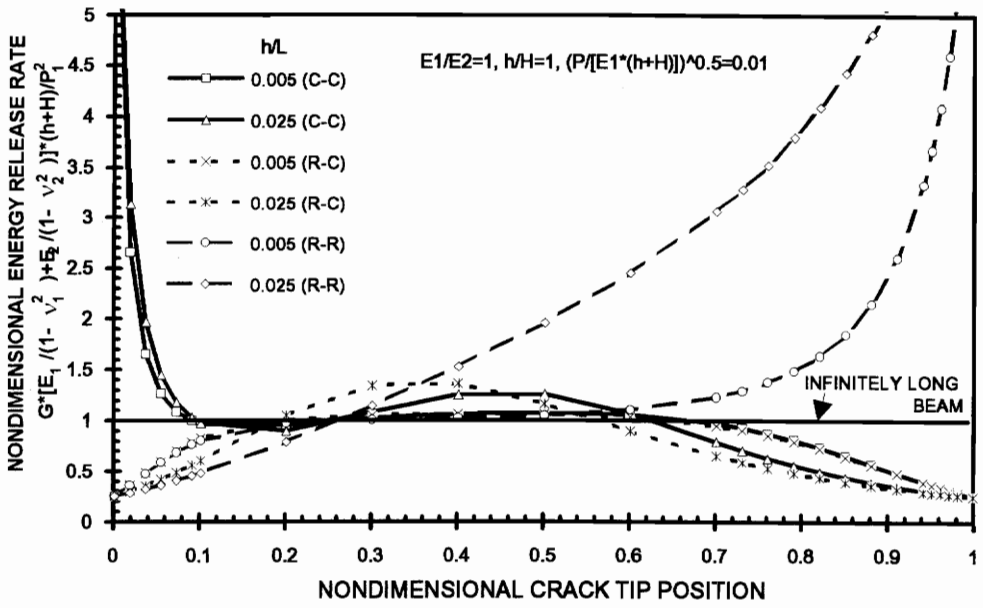

Figure 6.3 Nondimensional energy release rate versus nondimensional position of the crack tip for various nondimensional strap thicknesses.

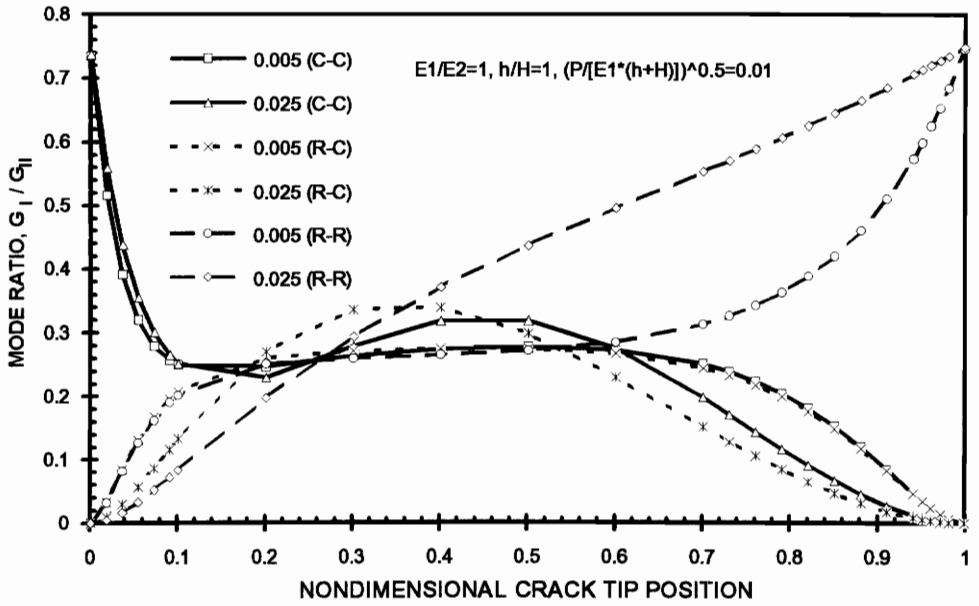

Figure 6.4 Ratio of mode I to mode II energy release rates versus the nondimensional crack tip position for various nondimensional strap thicknesses.

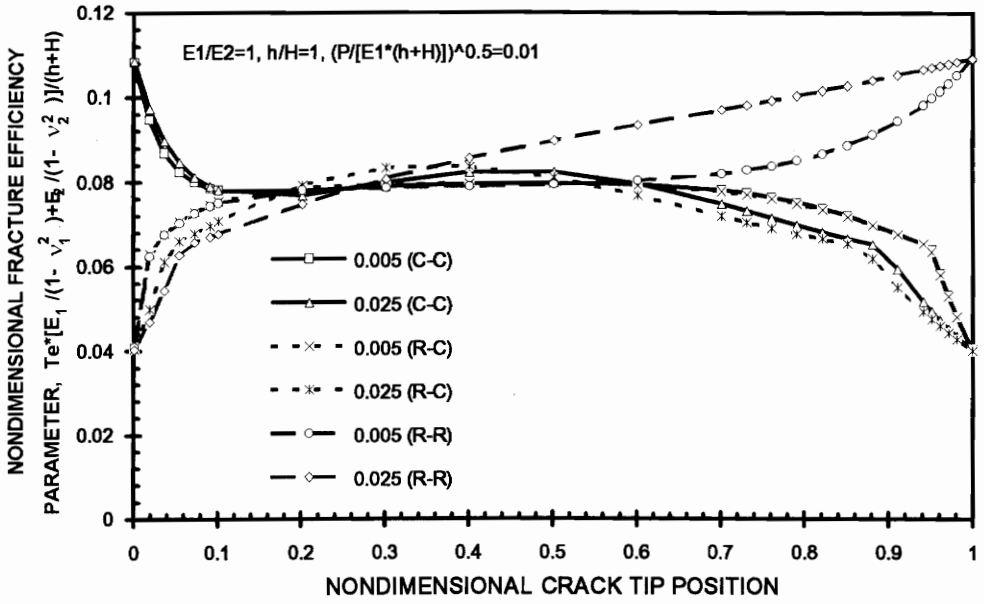

Figure 6.5 Nondimensional fracture efficiency parameter versus nondimensional crack tip position for various nondimensional strap thicknesses.

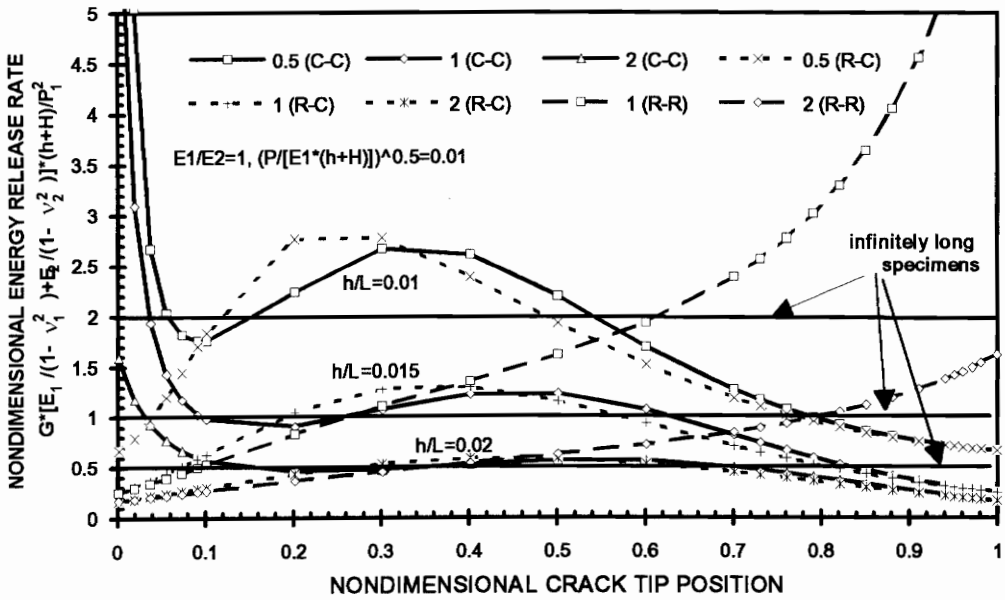

Figure 6.6 Nondimensional energy release rate versus nondimensional crack tip position for cracked lap shear specimens with various thickness ratios and nondimensional strap thickness.

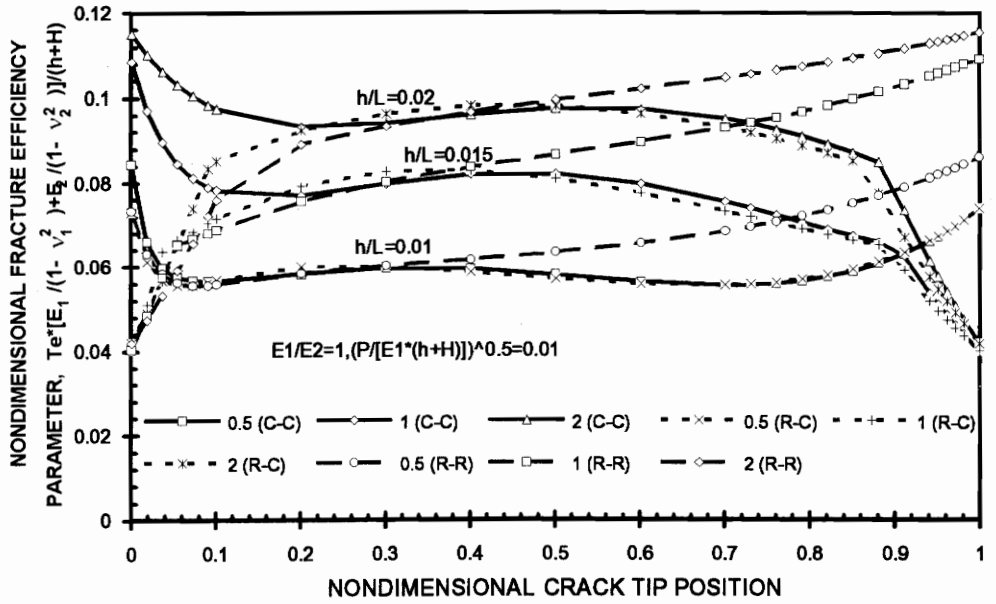

Figure 6.7 Nondimensional fracture efficiency parameter versus nondimensional crack tip position for cracked lap shear specimens with various thickness ratios and nondimensional strap thickness.

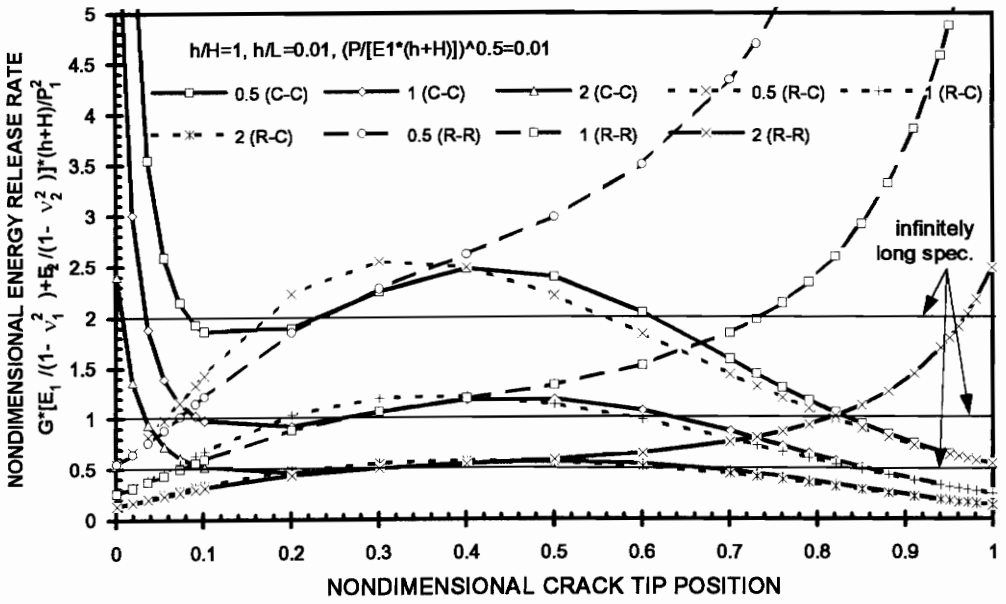

Figure 6.8 Nondimensional energy release rate versus nondimensional position of the crack tip for various adherend modulus ratios.

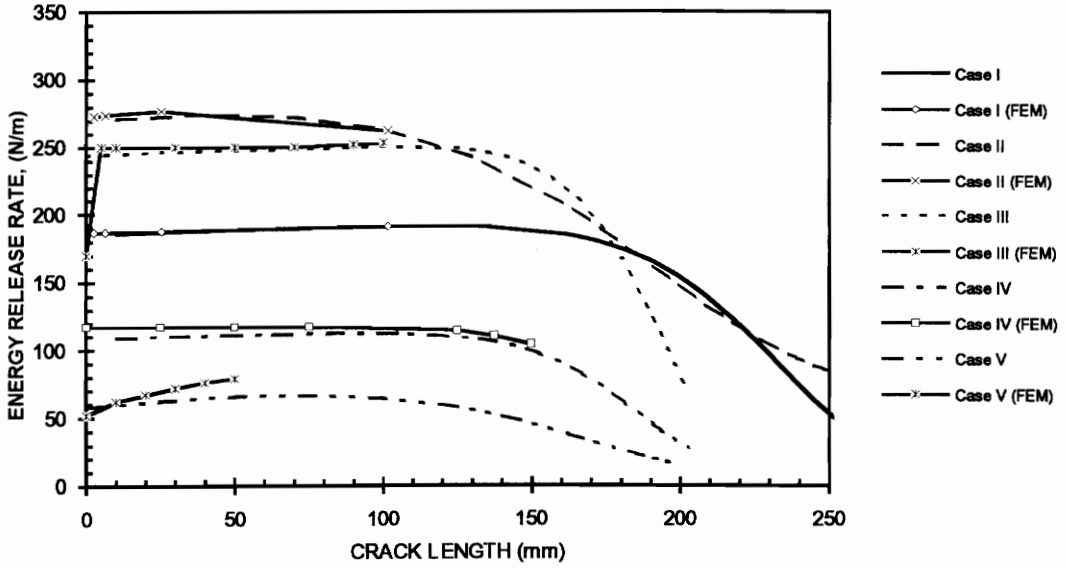

Figure 6.9 Comparison of energy release rates between the closed-form solution and various finite element analyses.

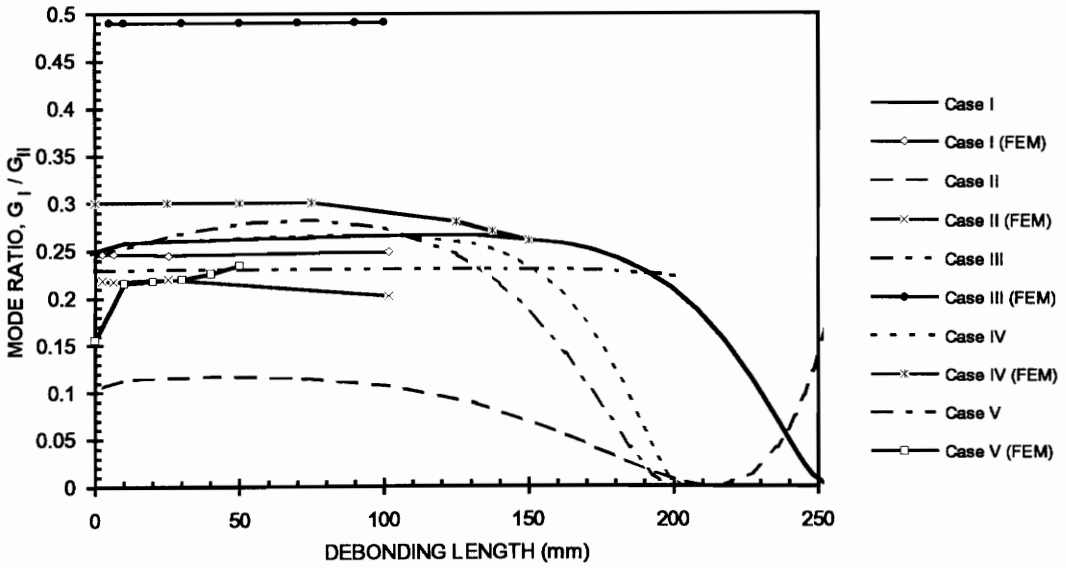

Figure 6.10 Mode ratio comparison between the analytical and finite element analysis.

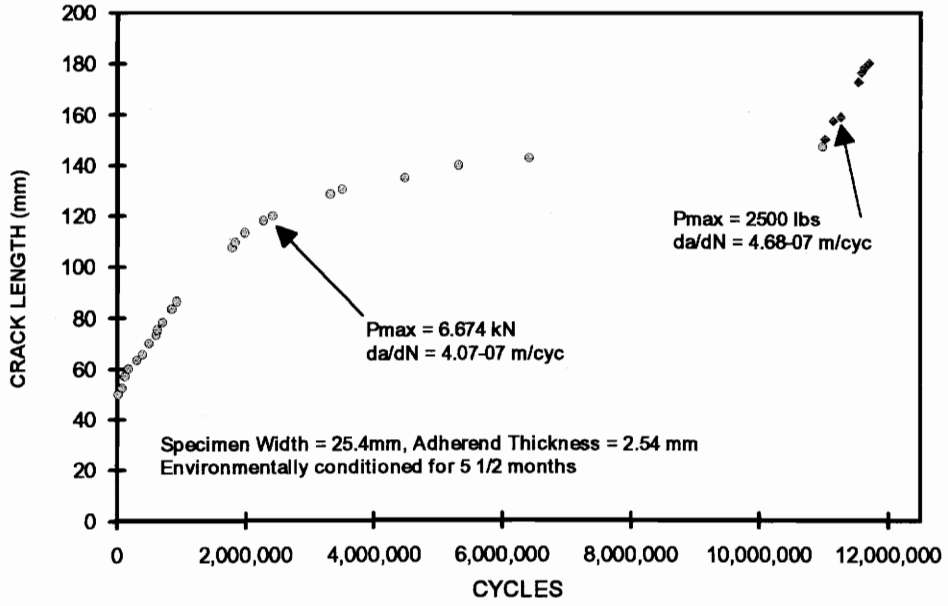

Figure 6.11 A typical fatigue crack growth history using a cracked lap shear specimen.

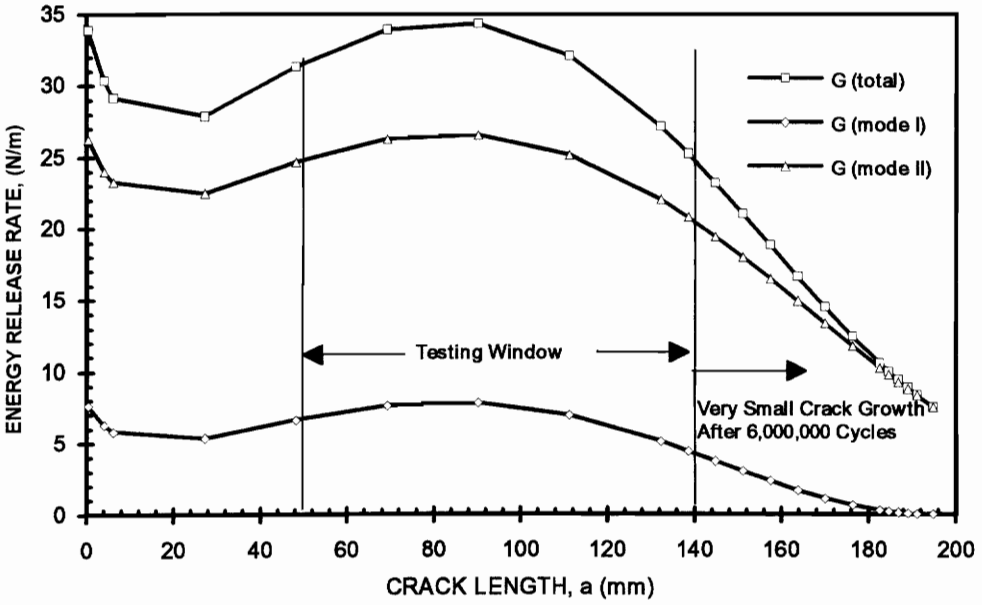

Figure 6.12 Energy release rate versus crack length for the specimen discussed in Fig. 6.11.

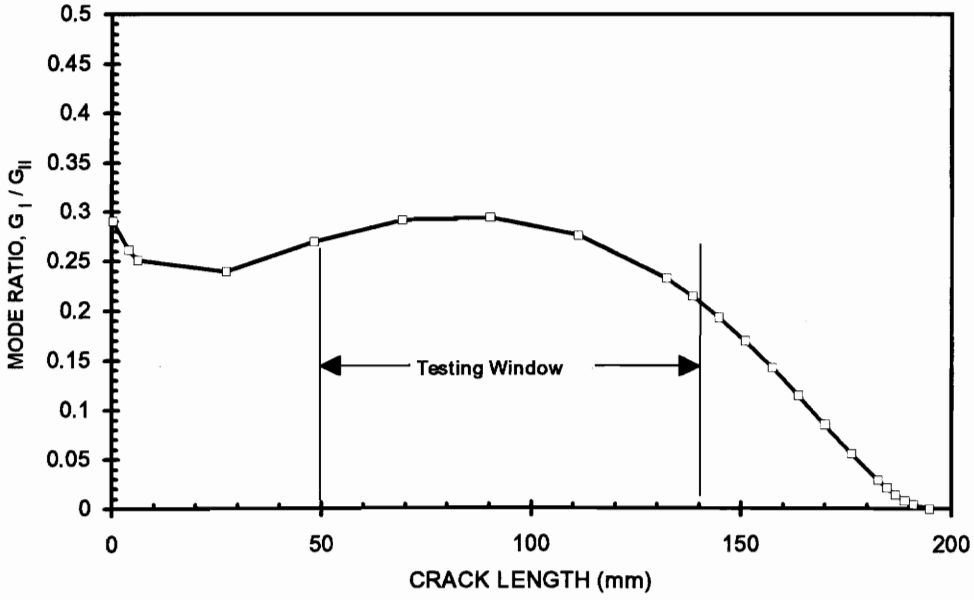

Figure 6.13 Mode ratio versus crack length for the specimen discussed in Fig. 6.11.

Chapter 7. Experimental Implementation of the Peninsula Blister Test

7.1 Introduction

Over the years, a variety of experimental techniques have been developed to determine energy release rates using various blister test geometries. One technique may require more or less information than another depending on the analysis method for that test geometry. Dannenberg measured the pressure/volume relationship and the debond area during the loading/debonding/unloading process and used the energy balance equation, Eq. (2.16), to obtain the critical energy release rate. The only major requirement was that the coating remains within the elastic range. The energy release rates obtained by this method did not have errors due to assumptions made in the derivation of the mathematical model for the test geometry. The material properties and specimen dimensions were also not needed. One major reason why this technique could be used was because of the constant energy release rate feature in Dannenberg's test geometry.

Gent and Lewandowski (1987) measured the critical pressure at debond initiation and the deflection at the center of the standard blister, and then used a membrane solution to obtain the critical energy release rate. The measurement of the deflection at the center of the blister was used to verify the validity of the mathematical model and also eliminated the need to measure the material properties, specimen dimensions, and debond area. Dillard and Chang (1987) and Chang et al. (1989) measured the applied pressure, constraint height, debond radius and the radius of the contact region in the constrained blister test and used an approximate solution to obtain the energy release rates. The material properties and specimen thickness are not needed using this solution. Unlike

Gent and Lewandowski's technique which is valid only for membrane specimens since the analytical solution is for the pressurized circular membrane problem, Dillard's method could be used for very thin to moderately thick specimens. Allen and Senturia (1987, 1988) measured the critical pressure, island radius, and perimeter dimension, and then used a dominant prestress membrane solution to determine the energy release rate in the island blister test. The method relies on the validity of the analytical solutions and also requires the knowledge of prestress, specimen dimensions, and initial debond area. The method may induce large errors if the solution is not valid for particular material systems or specimen sizes.

In this chapter, the experimental techniques needed to determine the energy release rates will be investigated using the peninsula blister geometry. Two different analysis methods for the peninsula blister will be used to determine the energy release rates and compared with each other. One is to measure the debond pressure and then use the analytical solution to determine the applied energy release rate. The analysis method is similar to the one used in the island blister study by Allen and Senturia (1987, 1989). The other is to record the pressure/volume curves during the loading/debonding/unloading process and to measure the debond area, then use the energy balance equation to determine the energy release rate. The method is similar to the one used in Dannenberg's blister test study.

7.2 Experimental Apparatus and Testing Procedure

The experimental apparatus and the testing procedure of the peninsula blister test will be described briefly in this section. More detailed information can be found in the Appendix E.

7.2.1 Experimental Apparatus

The experimental apparatus for the peninsula blister test should fulfill two major requirements: capability for recording the applied pressure and blister volume during the loading (pressurization), debonding, and unloading (depressurization) process and capability for recording the debond length during the debonding process. The experimental setup shown in Fig. 7.1 was designed to satisfy these two requirements. The setup consists of a pressure source, two mass flow meters, a control valve, a needle valve, a safety valve, a pressure transducer, a pressure/flow controller, a peninsula blister fixture, a video camera, a video cassette recorder, and a computer data acquisition system. The pressure source consists of a nitrogen gas tank. The peninsula blister fixture is shown in Fig. 7.2 which is made of aluminum and may have various dimensional designs. Typically, the outer perimeter of the fixture has a dimension of 113mm by 20.3mm and the peninsula has a dimension of 87mm by 1.59mm. The nitrogen gas tank has a pressure regulator of 138 kPa (20 psi) capacity. The flow meters are MKS 258C mass flow meters from MKS Instruments, Inc. The designed range of flow measurable with this mass flow meter is 0 to 10 standard cubic centimeters per minute. The signal from the meter is sent back to the controller as a 0 to 5 volt DC output. Pressure in the system is measured using either an MKS 122A absolute pressure transducer with a capacity of 666.42kPa (96.680 psia) or an MKS 122 gauge pressure transducer with a capacity of 133.28 kPa (19.336 psig). Both pressure transducers have an output signal of 0 to 10 volts. The flow input to the system is regulated by an MKS 248A electro-magnetic control valve. The valve seat is lifted away from the flow orifice as current is supplied to the valve. The current can be controlled from an MKS 250C pressure/flow controller. To release pressure in the system, a needle valve is installed following the second flow meter. To connect between various components, stainless steel tubing of 0.25" outer diameter and Swagelock connectors are used. The signals from the transducers are recorded using a Macintosh computer. An analog/digital (A/D) board, model number NB-MIO-16X by National

Instruments, Inc., is used to interface between the transducers and the computer. A computer program based on the LabView (version 2.2, by National Instruments, Inc.) is used to coordinated the data-acquisition process. Recorded data are then imported into a spreadsheet file for further analysis. To eliminate noises, the signals are averaged at a specific number of readings at specific time periods. Typically, the average was at the rate of one thousand readings per one twentieth of a second. The video camera and video cassette recorder were used to record the images of the debonding process for further analysis.

7.2.2 Testing Procedure

The peninsula blister specimens could be prepared either by bonding the film directly onto the peninsula and the perimeter of the fixture or by mounting the prefabricated sample with suspended membrane on the substrate. After the sample was mounted onto the fixture, the perimeter was then clamped to prevent debond into the perimeter. In the current experiment, after the adhesive tape was bonded onto the peninsula blister fixture, the pressure regulator on the nitrogen gas tank was then set at a constant pressure and the control valve was opened to begin the loading process. Before the control valve was opened, the data acquisition program was run to take data as the initial values for flow rates and pressures. The control valve could be controlled at three different modes: flow rate control, pressure control, or manual control. The manual control mode was used in the study of the adhesive tape. When debonding occurred, a constant pressure was maintained by opening or closing the control valve. When the debond front reached a desired position, the pressure was then reduced until the pressure in the blister fixture was zero. During the loading/debonding/unloading process, the pressure and flow rate versus time were recorded at set time intervals by a program written using the LabView software. The streams of data were then saved in a file for further analysis.

7.3 Determination of the Bond Fracture Strength using the Peninsula Blister Test

Two analysis methods, the analytical and compliance methods, can be used to determine the energy release rate in the peninsula blister test. The analytical method is based on the analytical solutions of energy release rates such as the ones obtained in Eqs. (3.17) and (3.19) for the membrane solutions or plate solutions by Dillard and Bao (1992). To use the analytical solutions to determine the energy release rate, one needs to know not only the testing conditions such as the peninsula width, the debond length, the width of the outer perimeter, and the film thickness but also the prestress and the material properties of the film such as Young's modulus and Poisson's ratio. To use the experimental compliance method, one needs to determine the debond area and energy released during the debonding process. This method was originally utilized in the blister test for measuring the adhesion of paints by Dannenberg (1961). The experimental compliance method will be described as follows.

During the debonding process, the energy released needed to create new fracture surface is equal to the product of the energy release rate and the increment of debond area and can be expressed as:

$$G\delta A = \delta W - \delta U - \delta Z. \tag{7.1}$$

where

δA is the change of the debond area,

δW is the change of the external work,

δU is the change of the strain energy,

and δZ is the plastic and viscoelastic energy dissipation during the debonding process.

If the energy dissipation due to plasticity and viscoelasticity, δZ is negligible and the pressure/volume curves can be represented by the curves, OA, AB and BA. in Fig.7.3(a). The variation of external work is equal to the area ABB'A'. The area can be easily

obtained using numerical integration. The variation of strain energy is equal to the difference between the area OBB'O and area OAA'O. Therefore the energy released during the debonding process is equal to the area OABO. The energy release rate can then be easily obtained by taking the ratio of the area OABO to debond area, δA.

It should be noted that if the film is plastically or viscoelastically deformed during the loading/debonding/unloading process, the pressure/volume behavior would be different and the term δZ in Eq. (7.1) can not be neglected. A typical pressure/volume relationship in this situation could be represented by the curves OCDE in Fig. 7.3(b). The unloading curve, DE, would not return to the origin O. Since plastic and viscoelastic energy dissipation can not be obtained from the pressure/volume curves, the energy release rate can not be determined from the compliance method used in Fig. 7.3(a).

7.4 Material Properties of the Peninsula Blister Sample

The material chosen for the current study is a pressure sensitive adhesive (PSA) tape supplied by 3M Corp. The PSA tape has a polyester backing and natural rubber adhesive. The thickness of the PSA tape is 0.102 mm (0.004 in). By cutting the tape into a strip of about 100mm by 25mm, tensile tests were performed on these strips using an Instron load frame. Since the PSA tape may not have the same material properties in both machine and cross directions, two types of strips were made. The machine direction is corresponding to the peninsula length direction when the tape is applied onto the peninsula fixture. Figure 7.4 illustrates a typical stress-strain curve for the PSA tape strips. The crosshead speed is 1 mm/min. The stress and strain have a relatively linear relationship when stress is smaller than 15 kPa and then the Young's modulus is taken from this region. Since both kinds of strips are loaded beyond the yielding point and then unloaded, the permanent deformation is seen for both curves. Although not shown in Fig. 7.4, it is found that if the specimen is loaded and unloaded before the yielding point is exceeded, no permanent deformation is observed. However, the unloading curve does not follow the same trace as

the loading curve. Instead, it forms a closed loop with the loading curve, which suggests that the PSA tape responds viscoelastically. The viscoelastic response can also be seen from Fig. 7.4 which has different loading and unloading slopes when stress is smaller than the yielding stress. The Young's moduli was found to be about 1.025 GPa and 921 MPa in the cross and machine directions, respectively. Using the 0.2% offset criterion, the yielding stresses were also found to be 15.7 MPa and 19.3 MPa.

7.5 Results and Discussions

Figure 7.5 illustrates typical debonding results of a pressure sensitive adhesive tape on an aluminum substrate with an acetone surface cleaning under different debonding pressures. Debonding rates can be determined from the slopes of the linear regression fits to each set of data. Relatively constant debonding rates can be seen for different pressures, suggesting that the applied energy release rates are constant at constant pressures. It is also seen that higher debonding rates are observed for the higher pressures and therefore, higher applied energy release rates, as would be expected.

Figure 7.6 illustrates the debonding rate versus applied energy release rate. To compare with these peninsula blister results, results from the 90° and 180° peel tests are also plotted. The peel tests were conducted for the same pressure sensitive adhesive tape on the aluminum substrate using a slip/peel tester (model 3M90 of Instrumentor, Inc.). A similar trend is seen between peel tests and peninsula blister test. Time dependent debonding behavior similar to that observed by Mostovoy and Ripling (1971) in a tapered double cantilever beam test is seen. The measured energy release rate ranges from 50 to 450 N/m. The debonding rate ranges from 0.00003 to 0.03 m/sec. Although the upper and lower bounds of energy release rate are not obtained in the experiment, the test does show the ability of measuring a wide range of energy release rate and debonding rate.

Before proceeding to discuss the results in Fig. 7.7, it is useful to use the normalized fracture efficiency parameter to estimate the maximum bond fracture strength that most

membrane peeling tests can measure without exceeding the yielding stress of the sample. Using Eq. (6.28) and the material properties described in Section 7.4, it is found that the estimated maximum bond fracture strength is about 6 N/m. Any measured bond fracture strength larger than 6 N/m suggests that gross yielding occurs and the measured value is in errors.

Figure 7.7 illustrates a series of loading/debonding/unloading processes for the PSA tape. The aluminum fixture is an aluminum fixture with a peninsula length of 80mm, a peninsula width of 1.59mm, a peripheral width of 19.05mm, and a peripheral length of 114.3mm. A series of loading/debonding/unloading curves are obtained for various pressures. Two numbers above each set of loading/debonding/unloading curve represent the energy release rates. The top number is obtained from the compliance method described in Section 7.3. The number inside the brackets is obtained from the analytical method, Eq. (3.19). It is found that all values obtained from both analysis methods greatly exceed 6.2 N/m, which suggests that inelastic deformation has occurred. The experimental observation of the residual blister volume for each loading/debonding/ unloading cycles further supports the evidence that gross yielding has occurred during the debonding process. Although the calculation of the membrane stress away from the debond front from Eqs. (3.11) and (3.5-4) shows that the membrane stress is well below the yielding stress, the permanent deformation suggests that only the stress near the debond front exceeds the yielding stress. Since the plastic deformation is confined only near the trace of the debond growth, the specimen does not curl up like it is commonly seen in a peeled PSA tape in the 180 degree peel test. However, it does not suggests that the peninsula blister specimen dissipates less energy for a given debond area. The curl-up in the peel test is because the yielding occurs across the whole width of the specimen. Since the yielding in the peninsula blister test occurs at a fraction of specimen width, this permanent deformation is not able to cause curl-up. Another observation made in this figure is that the loading curve does not follow the same path as the unloading curve in the previous loading/debonding/unloading cycle. The observation suggests that in addition to

the plastic energy dissipation in each cycle, there is also viscoelastic energy dissipation. Since viscoelastic energy dissipation depends on the loading/debonding/unloading rate of each cycle, which is very difficult to control using the compressible medium such as nitrogen gas, it may also explain why the deviation of the bond fracture strength obtained from the compliance method is relatively large.

The loading/unloading curves for the totally debonded specimens are seen in Fig. 7.8. In this test, the blister was not immediately depressurized after the pressure reached the maximum value, instead, there was a 30 seconds lag between the end of the pressurization process and the initiation of the depressurization process. It is seen that the creep volume is relatively significant. The loading and unloading curves form a hysteresis with a viscoelastic energy dissipation of 0.00059 J. Even without the 30 second delay, the viscoelastic energy dissipation is estimated to be about 0.00031 J, which is about 20% of the work input the system during the pressurization process. It should be noted that there is no residual volume after the pressure is completely released, which suggests that there is no plastic deformation and all the energy dissipation is due to the viscoelastic dissipation.

Although the plastic energy dissipation during the debonding process may be avoided by testing the PSA tapes with multi-layers, the viscoelastic energy dissipation may still not be avoided. To properly determine the amount of viscoelastic energy dissipation, the proposed technique in Appendix B may be used.

7.5 Summary

This chapter discussed the use of the peninsula blister test geometry to measure the bond fracture strength of a pressure sensitive adhesive (PSA) tape bonded to an aluminum substrate. Both analytical and experimental compliance methods were used to determine the bond fracture strength of the adhesive tape. Similar trends in the debond rates were seen between the energy release rate obtained from the peninsula blister test and peel tests. The debonding rate in the peninsula blister test is relatively constant for a given pressure.

The Time dependent debonding behavior of the PSA tape was observed. The normalized fracture efficiency parameter suggested that the maximum bond fracture strength that could be measured from the peninsula blister test for the single-layer PSA tape without gross yielding was about 6 N/m. However, the measured energy dissipation per unit debonding area was at least 30 times of that value, which suggested that significant energy had been dissipated due to plastic and viscoelastic effect.

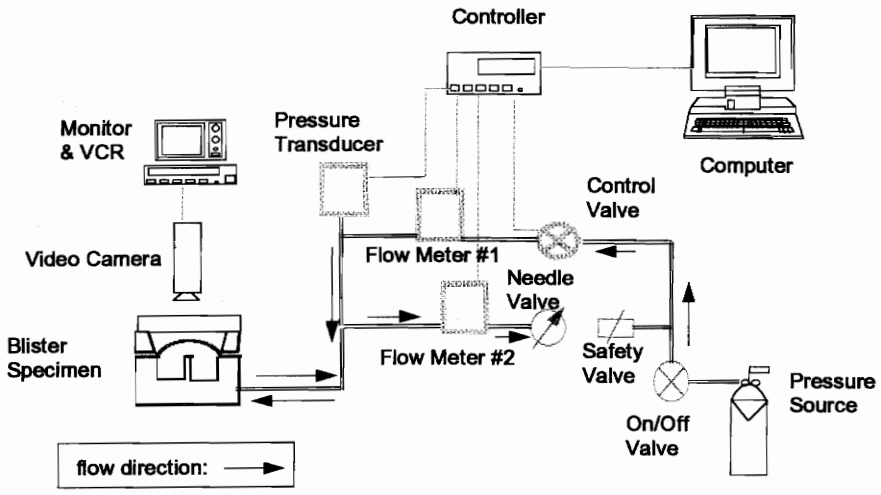

Figure 7.1 Experimental setup of the blister test.

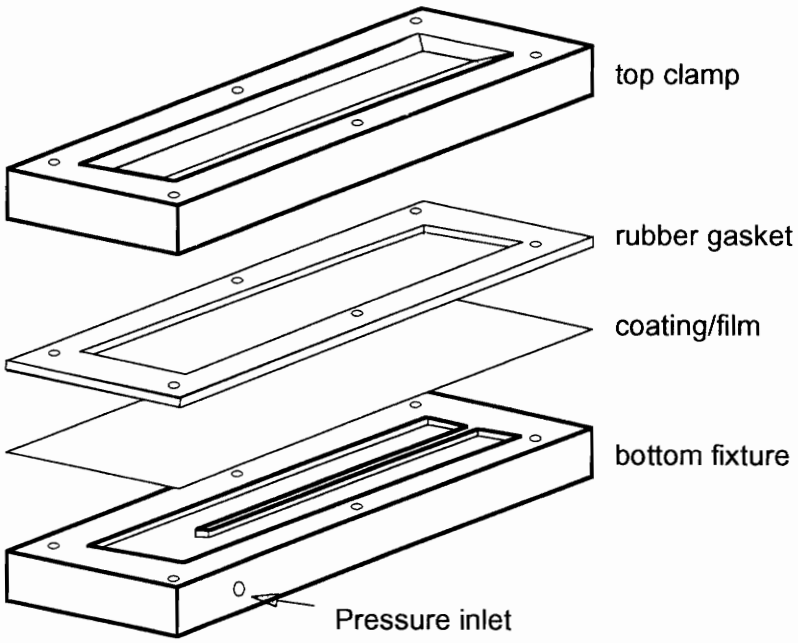

Figure 7.2 Peninsula blister fixture with a specimen.

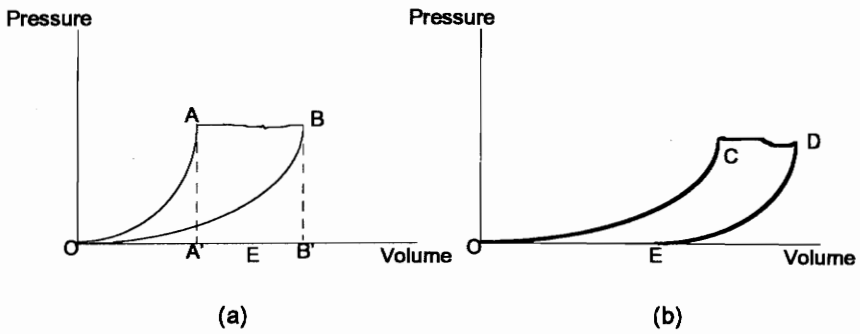

Figure 7.3 Typical pressure/volume curves in a peninsula blister test. (a) Elastic response. (b) Inelastic response.

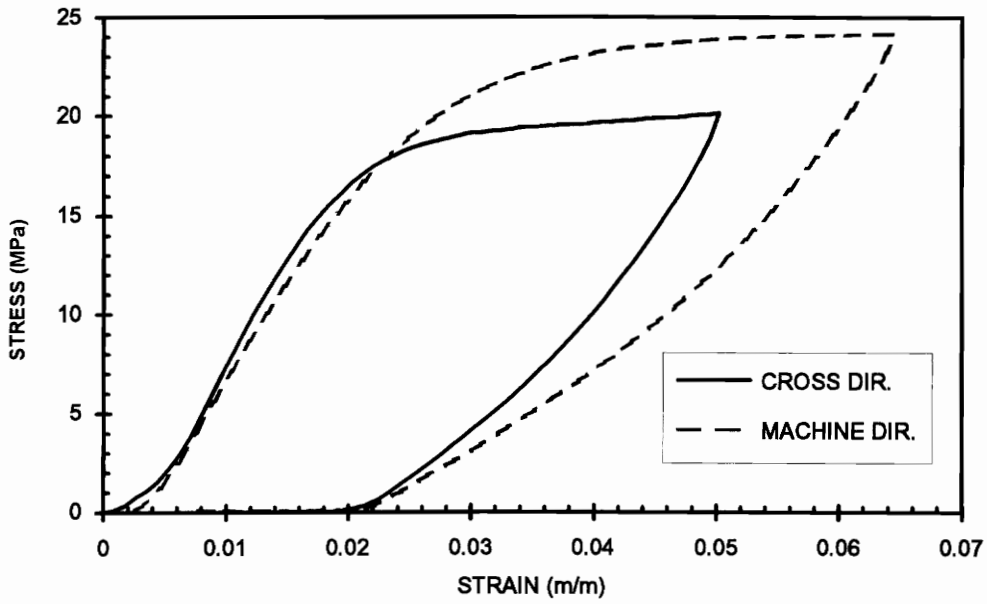

Figure 7.4 Stress-strain relationship for a pressure sensitive adhesive tape.

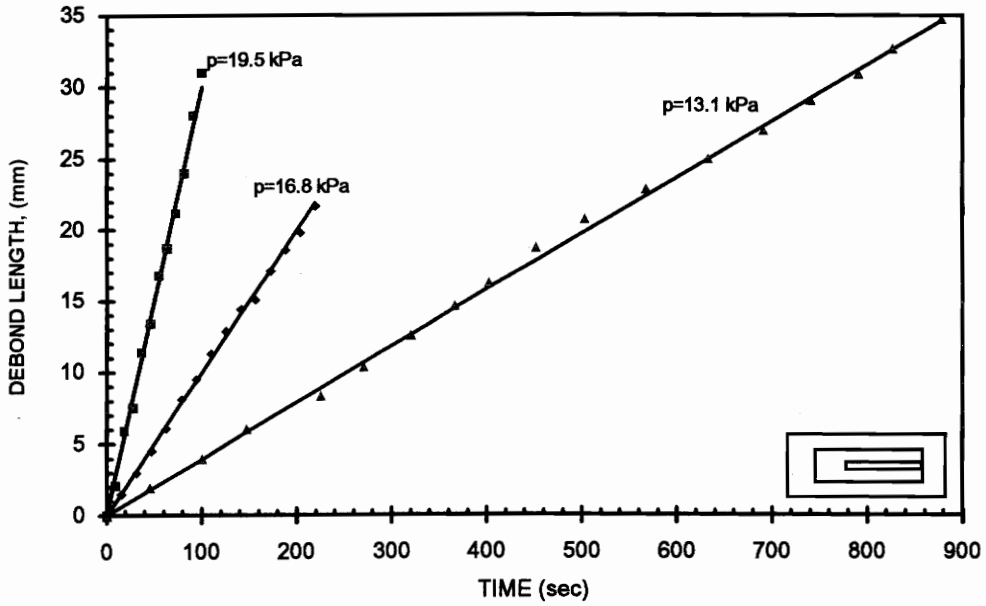

Figure 7.5 Typical debond length versus time of a pressure sensitive adhesive tape in a peninsula blister test.

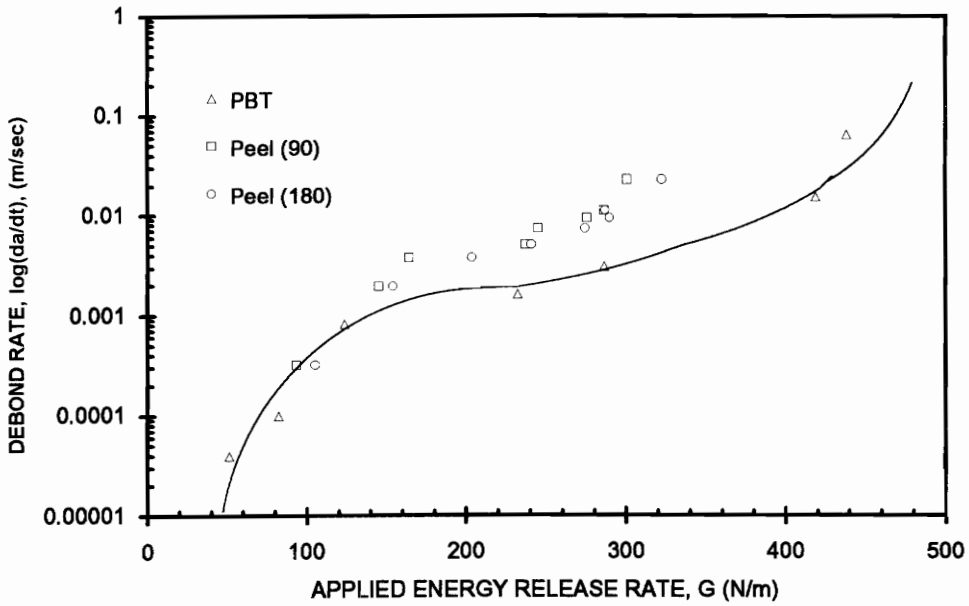

Figure 7.6 Debonding rate versus applied energy release rate of a PSA tape on an aluminum substrate in peninsula blister tests and peel tests.

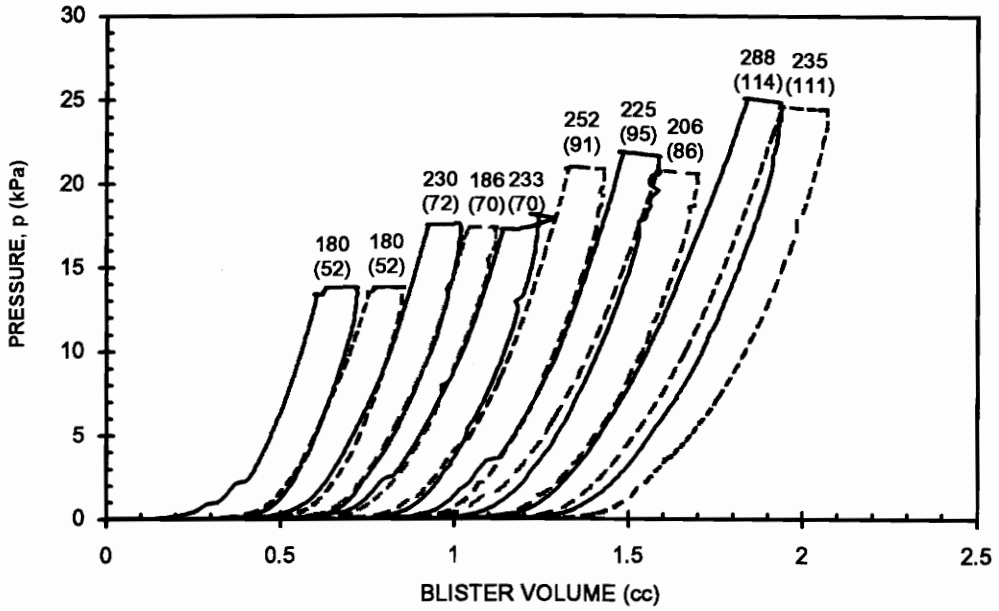

Figure 7.7 Typical pressure/volume curves of a pressure sensitive adhesive tape on an aluminum substrate in a peninsula blister test.

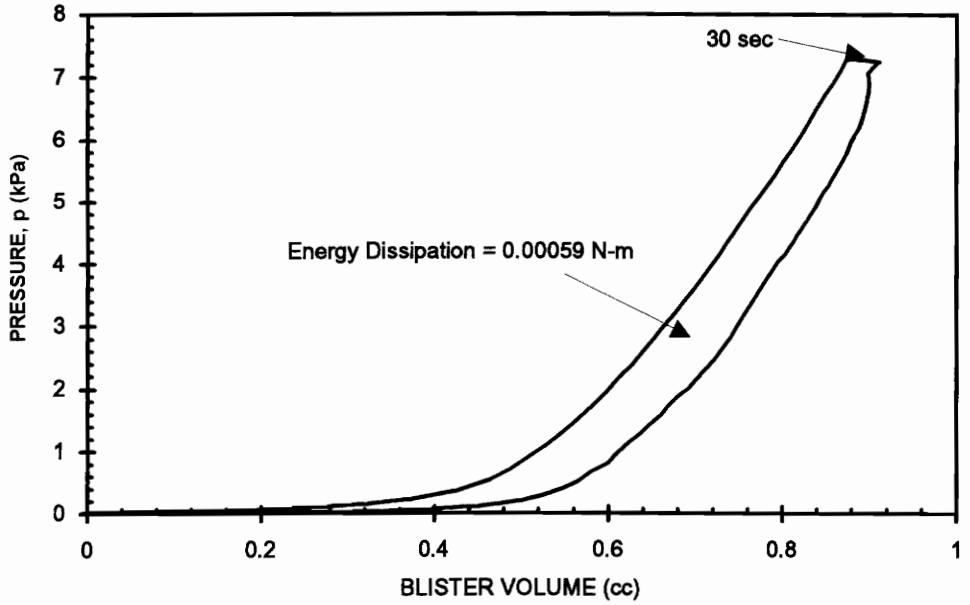

Figure 7.8 Loading/unloading curves of a totally debonded PSA samples in the peninsula blister test.

Chapter 8 Conclusions

A novel concept, the fracture efficiency, was proposed in this dissertation to evaluate the performance of fracture specimen designs for adhesive bonds. The study of fracture efficiency led to the new analysis of many existing fracture test geometries. The results from the study of fracture efficiency and these new analyses provide useful tools to determine specimen designs and to gain a better understanding of how these test geometries behave.

In this dissertation, the membrane solutions and most importantly, the energy release rates, for the standard blister, island blister, and one-dimensional blister tests with an arbitrary magnitude of prestress in the membranes have been obtained. The energy release rate for the peninsula blister test was also derived. Based on these solutions, the range of the prestress in which the two commonly used limiting solutions, no-prestress and dominant prestress solutions, were applicable was identified. It was shown that the improper use of limiting solutions could cause gross errors in determining energy release rates.

Because high energy release rates could be obtained at low pressures in the island and peninsula blister tests, as was also shown in this dissertation, there was a misconception by many that these so called "high energy release rate" tests could be used to debond films without exceeding their tensile strength limits. Although high energy release rates could be obtained in the island blister test, a high stress concentration near the debond front was also found. Both the energy release rate and the stress concentration increased significantly as the island radius decreased for a given pressure, which suggested that the island blister test could still exceed the tensile limits of the films no matter how the island size was reduced.

Compared with the peel test near the debond front, it was found that blister tests were special cases of the peel test despite the obvious difference in the test geometries and

loading conditions. The search for the true criterion of the "high energy release rate" test led to the proposal and investigation of a simple parameter - the fracture efficiency parameter. Defined as the ratio between the energy release rate and the square of the maximum non-singular stress, the fracture efficiency parameter is an index of how much crack driving force a certain test geometry or specimen dimension can produce along the bondline for a given maximum stress in the adherends. The fracture efficiency parameter can be used to evaluate the fracture efficiency, or the performance, of a certain specimen design. This dissertation demonstrated that the concept of fracture efficiency can be applied to design the optimal fracture test so the test would be more likely to debond the specimen without causing yield/failure in the adherends or films.

In this dissertation, it was shown that the development of membrane peeling tests of high fracture efficiency for films and coatings is unlikely. The use of membrane peeling tests on many films and coatings with relatively strong adhesion is very likely to cause unavoidable gross inelastic energy dissipation or rupture. Therefore, the commonly used analysis method based on the assumption that materials behave elastically is likely to give gross errors in determining the bond fracture strength. This prediction was supported by evidence found in the literature and by tests conducted on a pressure sensitive adhesive tape using the peninsula blister test. To measure the film adhesion, the analysis in this dissertation demonstrated that the proper use of a backing material could significantly increase the fracture efficiency and therefore, suggested that it might be preferable to measure the film adhesion with backings. To directly measure the film adhesion using membrane specimens with inelastic deformation, a new experimental technique based on the peninsula blister test was proposed. The proposed technique may allow one to measure the bond fracture strength by considering the gross inelastic effects. This technique takes advantage of some unique features of the peninsula blister geometry to separate the inelastic energy dissipation from the total energy dissipation during the debonding process and therefore allows the bond fracture strength to be measured.

The experimental setup, testing procedure, and data analysis methods for measuring material properties of films and coatings using the peninsula blister fixture have also been

presented. A pressure sensitive adhesive tape was used as a model sample to measure the bond fracture strength. The results from peel tests were obtained for comparison. The results demonstrated that the peninsula blister test was capable of testing specimens with time dependent debonding response in a wide range of debonding rate. However, the experimental results also suggested that the plastic and viscoelastic energy dissipation resulted in significant error, which was also predicted from the study of the fracture efficiency.

Although the study of film and coating test methods found little opportunity for improving the fracture efficiency of membrane peeling tests except if backing is added, the study of laminated beam specimens showed that significant improvement in the fracture efficiency could be achieved by using different test specimens or designing different specimen dimensions. Particularly, the cracked lap shear specimen was investigated in greater details. A nondimensional closed form solution for the cracked lap shear specimens based on a nonlinear beam-column approach was obtained. Excellent agreement of the energy release rates was shown between the closed form solution and geometrically nonlinear finite element analyses. The closed form solution was also used to explain the anomalous fatigue results in previous cracked lap shear tests.

Appendix A Coefficients for the Cracked Lap Shear Solution

The unknown constants in Eqs. (7.4) can be easily solved by linear algebra. After careful examination, it is found that all the parameter in chapter 7 can be expressed by the following five nondimensional quantities:

$$\text{nondimensional applied load: } \hat{P} = \sqrt{\frac{P}{\hat{E}_1(h+H)}}, \tag{A.1}$$

$$\text{nondimensional crack tip position: } q = \frac{\ell_1}{L}, \tag{A.2}$$

$$\text{nondimensional strap thickness: } \kappa = \frac{h}{L}, \tag{A.3}$$

$$\text{adherend thickness ratio: } \eta = \frac{h}{H}, \tag{A.4}$$

and

$$\text{adherend modulus ratio: } \Sigma = \frac{\hat{E}_1}{\hat{E}_2} \tag{A.5}$$

To simplify the expressions of the unknown constants, the following nondimensional notations are introduced.

$$a_1 = \sinh(\lambda_1 \ell_1) = \sinh\left(\frac{q}{\kappa}\hat{P}\sqrt{12(1+1/\eta)}\right), \tag{A.6}$$

$$a_2 = \frac{\lambda_1}{\lambda_0} = 2\sqrt{3I/\Sigma}, \tag{A.7}$$

$$a_3 = \cosh(\lambda_1 \ell_1) = \cosh\left(\frac{q}{\kappa}\hat{P}\sqrt{12(1+1/\eta)}\right), \tag{A.8}$$

$$a_4 = \sinh(\lambda_0 \ell_0) = \sinh\left(\frac{(1-q)}{\kappa}\hat{P}\sqrt{12(1+1/\eta)}\right), \tag{A.9}$$

$$a_5 = \cosh(\lambda_0 \ell_0) = \cosh\left(\frac{(1-q)}{\kappa}\hat{P}\sqrt{12(1+1/\eta)}\right), \tag{A.10}$$

$$a_6 = \frac{1}{L\lambda_1} = \frac{q}{\lambda_1 \ell_1} = \frac{q}{\left(\frac{(1-q)}{\kappa}\hat{P}\sqrt{12(1+1/\eta)}\right)}, \tag{A.11}$$

and $$a_7 = \frac{\lambda_0}{\lambda_1} = \frac{1}{a_2} \tag{A.12}$$

With the help of Mathematica™ (Wolfram S., 1993), the unknown constants can be easily obtained and listed as follows.

Case A. Roller-Roller Configuration

$$A_1 = 0, \tag{A.13}$$

$$B_1 = \frac{-\alpha_n a_5}{a_1 a_5 + a_2 a_3 a_4}, \tag{A.14}$$

$$A_2 = B_1 a_2 a_3, \tag{A.15}$$

and $$B_2 = B_1 a_1 + \alpha_n \tag{A.16}$$

Case B. Roller-Clamped Configuration

$$\hat{R}_1 = (-(\alpha_n a_3 a_5^2) + \alpha_n a_2 a_3 a_4 a_6 + \alpha_n a_1 a_5 a_6 + \alpha_n a_2 a_3 a_4^2 a_7)/(a_3 a_5 - a_2 a_3 a_4 a_6 - a_1 a_5 a_6 + a_1 a_4 a_7) \tag{A.17}$$

$$A_1 = 0 \tag{A.18}$$

$$B_1 = (\alpha_n a_6 - \alpha_n a_5 a_6 + \alpha_n a_4 a_7)/(-(a_3 a_5) + a_2 a_3 a_4 a_6 + a_1 a_5 a_6 - a_1 a_4 a_7) \tag{A.19}$$

$$A_2 = (-(\alpha_n a_3 a_5) + \alpha_n a_1 a_6 + \alpha_n a_2 a_3 a_4 a_6)/(-(a_3 a_5) + a_2 a_3 a_4 a_6 + a_1 a_5 a_6 - a_1 a_4 a_7) \tag{A.20}$$

$$B_2 = B_1 a_2 a_3 \tag{A.21}$$

Case C. Clamped-Clamped Ends

$$\hat{m}_1 = (-(\alpha_n a_6 a_7) + \alpha_n a_3 a_4^2 a_6 a_7 + \alpha_n a_5 a_6 a_7 + \alpha_n a_3 a_5 a_6 a_7 - \alpha_n a_3 a_5^2 a_6 a_7 - \alpha_n a_4 a_7^2 + \alpha_n a_1 a_4 a_6 a_7^2) / (a_1 a_4 a_6 - a_1 a_5 a_7 - a_6 a_7 - a_1^2 a_4^2 a_6 a_7 + a_3^2 a_4^2 a_6 a_7 + 2 a_3 a_5 a_6 a_7 + a_1^2 a_5^2 a_6 a_7 - a_3^2 a_5^2 a_6 a_7 - a_3 a_4 a_7^2 + a_1 a_4 a_6 a_7^2) \quad (A.22)$$

$$\hat{R}_1 = (\alpha_n a_1 a_4 a_6 + \alpha_n a_1 a_4^2 a_7 - \alpha_n a_1 a_5^2 a_7 - \alpha_n a_6 a_7 - \alpha_n a_1^2 a_4^2 a_6 a_7 + \alpha_n a_3^2 a_4^2 a_6 a_7 + 2\alpha_n a_3 a_5 a_6 a_7 + \alpha_n a_1^2 a_5^2 a_6 a_7 - \alpha_n a_3^2 a_5^2 a_6 a_7 - \alpha_n a_4 a_7^2 + \alpha_n a_1 a_4 a_6 a_7^2)/(-(a_1 a_4 a_6) + a_1 a_5 a_7 + a_6 a_7 + a_1^2 a_4^2 a_6 a_7 - a_3^2 a_4^2 a_6 a_7 - 2 a_3 a_5 a_6 a_7 - a_1^2 a_5^2 a_6 a_7 + a_3^2 a_5^2 a_6 a_7 + a_3 a_4 a_7^2 - a_1 a_4 a_6 a_7^2) \quad (A.23)$$

$$A_1 = -\hat{m}_1 \quad (A.24)$$

$$A_2 = (-(\alpha_n a_1 a_4 a_6) + \alpha_n a_1 a_5 a_7 + \alpha_n a_6 a_7 - \alpha_n a_3 a_6 a_7 - \alpha_n a_1^2 a_5 a_6 a_7 - \alpha_n a_3 a_5 a_6 a_7 + \alpha_n a_3^2 a_5 a_6 a_7)/(-(a_1 a_4 a_6) + a_1 a_5 a_7 + a_6 a_7 + a_1^2 a_4^2 a_6 a_7 - a_3^2 a_4^2 a_6 a_7 - 2 a_3 a_5 a_6 a_7 - a_1^2 a_5^2 a_6 a_7 + a_3^2 a_5^2 a_6 a_7 + a_3 a_4 a_7^2 - a_1 a_4 a_6 a_7^2) \quad (A.25)$$

$$B_1 = -(a_n + \hat{R}_1) / a_6 \quad (A.26)$$

$$B_2 = (\alpha_n a_1 a_6 - \alpha_n a_1 a_5 a_6 + \alpha_n a_1 a_4 a_7 - \alpha_n a_1^2 a_4 a_6 a_7 - \alpha_n a_3 a_4 a_6 a_7 + \alpha_n a_3^2 a_4 a_6 a_7)/(a_1 a_4 a_6 - a_1 a_5 a_7 - a_6 a_7 - a_1^2 a_4^2 a_6 a_7 + a_3^2 a_4^2 a_6 a_7 + 2 a_3 a_5 a_6 a_7 + a_1^2 a_5^2 a_6 a_7 - a_3^2 a_5^2 a_6 a_7 - a_3 a_4 a_7^2 + a_1 a_4 a_6 a_7^2) \quad (A.27)$$

Appendix B The Parameters Used in the Finite Element Analysis for the Cracked Lap Shear Problems in the Literature

The following results are adapted from the literature on cracked lap shear specimens.

Case I (Johnson, (1987))

	Young's modulus	Poisson's ratio	Thickness	Length
Strap (Aluminum)	72.45 GPa	0.33	3.18 mm	305 mm
Lap (Aluminum)	72.45 GPa	0.33	6.35 mm	254 mm
Adhesive	1.932 GPa	0.40	0.13 mm	

This finite element analysis was performed by Dattaguru B. and Mangalgiri P.D. using GAMNAS program for the Round Robin compiled by Johnson (1987). Two dimensional, plane strain, and geometrical nonlinear options were used. The boundary conditions were equivalent to the roller-clamped case for the closed form solution. The mode I, mode II, and total energy release rates were calculated based on a virtual crack extension method. The crack was assumed to lie at the center of the bondline.

Case II (Johnson, (1987))

	Young's modulus	Poisson's ratio	Thickness	Length
Strap (Aluminum)	72.45 GPa	0.33	3.18 mm	305 mm
Lap (Aluminum)	72.45 GPa	0.33	6.35 mm	254 mm
Adhesive	1.932 GPa	0.40	0.13 mm	

The method used in this case is the same as that in the Case 1.

Case III (Dattaguru *et al.*, (1984))

	Young's modulus	Poisson's ratio	Thickness	Length
Strap (Aluminum)	71.02 GPa	0.33	3.2 mm	254 mm
Lap (Graphite/Epoxy)	130.93 GPa	0.0188	1.6 mm	203 mm
Adhesive	4.14 GPa	0.40	N/A	

This finite element analysis was performed using GAMNAS program. Two dimensional, plane stress, and geometrical nonlinear options were used. The boundary conditions were equivalent to the roller-clamped case for the analytical solutions. The mode I, mode II, and total energy release rates were calculated based on a virtual crack extension method. The crack was assumed to lie at the center of the bondline.

Case IV (Mall and Yun, (1987)

	Modulus	Poisson's ratio	Thickness	Length
Strap (Graphite/Epoxy)	131* GPa	0.34*	2.0 mm	241.3 mm
Lap (Graphite/Epoxy)	131* GPa	0.34*	2.0 mm	203.2 mm
Adhesive	4.14** GPa	N/A	0.2 mm	

* Not listed in the paper, an estimated value for an unidirectional Graphite/Epoxy composite.

** Shear modulus.

How the finite element analysis was performed is not available in the paper. However, plane strain analysis was assumed in the analytical solutions to compare with the results in this paper. The roller-clamped boundary conditions was used. The crack was assumed to located at the center of the bondline.

Case V (Edde and Verreman, (1992))

	Young's modulus	Poisson's ratio	Thickness	Length
Strap (Aluminum)	72 GPa	0.33	3.2 mm	250 mm
Lap (Aluminum)	72 GPa	0.33	3.2 mm	200 mm
Adhesive	3.1 GPa	0.41	0.3 mm	

This finite element analysis was performed using the ABAQUS program. Two dimensional, quadrilateral, plane strain elements, and geometrical nonlinear options were used. The boundary conditions were equivalent to the clamped-clamped case for the analytical solutions. The mode I, mode II, and total energy release rates were calculated based on a modified virtual crack extension method. The crack was assumed to located at the adhesive/strap interface.

Appendix C A Proposed Technique to Measure the Bond Fracture Strength of Films and Coatings Considering Gross Inelastic Energy Dissipation

C.1 Introduction

The study of the fracture efficiency parameter of membrane peeling tests for films and coatings in Chapter 7 suggests that current techniques all have similar fracture efficiency despite the significant differences in testing geometry and loading conditions. This study also suggests that to develop high fracture efficiency tests for films and coatings are unlikely. Furthermore, plastic and viscoelastic deformation may not be avoidable. It is necessary to develop new experimental or analytical techniques to account for the energy dissipation due to plasticity and viscoelasticity. The most recent works on the film adhesion problem considering the plastic deformation were done by Kim *et al.* (1988a, 1988b, 1989) and Aravas *et al.* (1989) who studied the thin metal film adhesion using peel tests by considering behavior elastic-plastic effect. This method is limited to elastic-plastic materials and peel tests and have not be extended to be used in the viscoelastic materials or other membrane peeling tests. Furthermore, determining the elastic-plastic material properties may not be a trivial job especially for thin polymeric films.

In this appendix, an experimental technique based on the peninsula blister will be proposed to determine the bond fracture strength by considering plastic and viscoelastic energy dissipation.

C.2 A Proposed Experimental Technique to Measure the Bond Fracture Strength by Considering the Plastic and Viscoelastic Energy Dissipation

To determine the bond fracture strength of films with gross plastic and viscoelastic energy dissipation in adherends, one needs to separate the amount of inelastic energy dissipation from the total energy dissipation in a debonding process. There are two possible methods to achieve this goal. The first one is to use a mathematical model which considers different inelastic effects and to solve this mathematical model according to the experimental conditions in the selected test. To use the finite element analysis, one needs to determine both the elastic and inelastic material properties of the films, which is often difficult task, especially to include biaxial, time dependence, etc. Furthermore, solving the problem of an thin membrane problem using finite element method considering plastic, viscoelastic, large strain, and large displacement effects which would be found in the experiment for this kind of material may be beyond the capability of today's finite element programs. The other possible method is to experimentally determine the inelastic energy dissipation during the debonding process. The proposed technique in this appendix belongs to the latter category and will be described below. It should be noted that the proposed technique may not be applicable when the fracture energy dissipation is of the same order as the experimental scatter in determining the inelastic energy dissipation.

The basic idea of the proposed technique is to separate the inelastic energy dissipation from the total energy dissipation during the debonding process by performing one test on a bonded specimen to obtain the total energy dissipation and then another test on a unbonded specimen to determine the inelastic energy dissipation. The difference of the two energy dissipation quantities is the energy required to create the new surfaces. With this energy quantity and the debond area which could be easily measured, the energy release rate can then be determined.

There are two major requirements to use this proposed technique. One is that the test of the unbonded specimen must be able to simulate all the testing conditions of the

bonded specimen. Since the energy is dissipated over a certain debond area in a period of time, the energy release rate will be an averaged quantity. To minimize the error due to the averaging process, a constant energy release rate test geometry is required. A potential test that may easily fulfill these two requirements is the peninsula blister test. In addition to the features that can fulfill the two requirements, the peninsula blister geometry also has the advantage of inducing relatively low stress away from the debond front which will reduce the amount of energy dissipation other than from the debond front.

Figure C.1 illustrates the experimental procedure for the proposed technique, which can be divided into three steps:

Step (1): Perform a peninsula blister test on a bonded specimen. The total energy dissipation is determined from the pressure/volume diagram. The debonding rate can also be determined. It should be noted that if the bulk viscoelastic effect is significant, the debonding rate at a constant pressure may not be constant. The phenomena has been observed by Chang, *et al.* (1989) in a constrained blister test for a vinyl adhesive tape.

Step (2): Perform a peninsula blister test on a unbonded specimen. To simulate the membrane bonded to the peninsula, use a plate with the same thickness as the peninsula width and press the membrane onto the peninsula as seen in Fig. C.2. The same loading rate will be applied to this specimen until the debonding pressure observed in the test in Step (1) is reached. The plate pressed on top of the peninsula will then be slid toward the end of the peninsula for the same distance as the debond front moved in the first test by a stepping motor programmed with the debonding rate obtained from the first test. To preventing the gouging of the membrane, Teflon plate may be used and/or lubrication may be needed. The energy dissipation in this process can then be determined from the pressure/volume diagram. If the plastic effect is negligible and the material could be totally relaxed so the pressure/volume curve return to origin such as in a viscoelastic solid material, the specimen used in the Step (1) can be re-used in Step (2).

Step (3): Calculate the difference between the energy released in Steps (1) and (2) and then divide the difference by the debond area. The value obtained is the bond fracture strength.

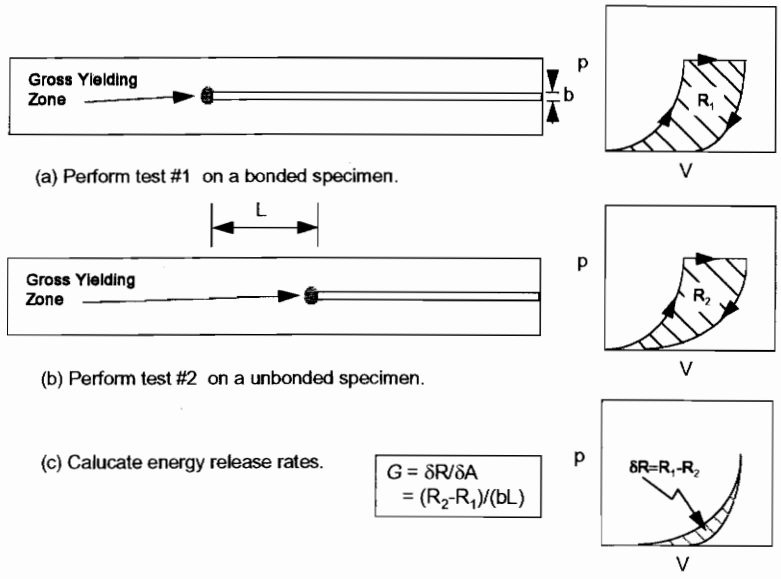

Figure D.1 Experimental procedure for the proposed technique to separate inelastic energy dissipation from the total energy dissipation in a debond process.

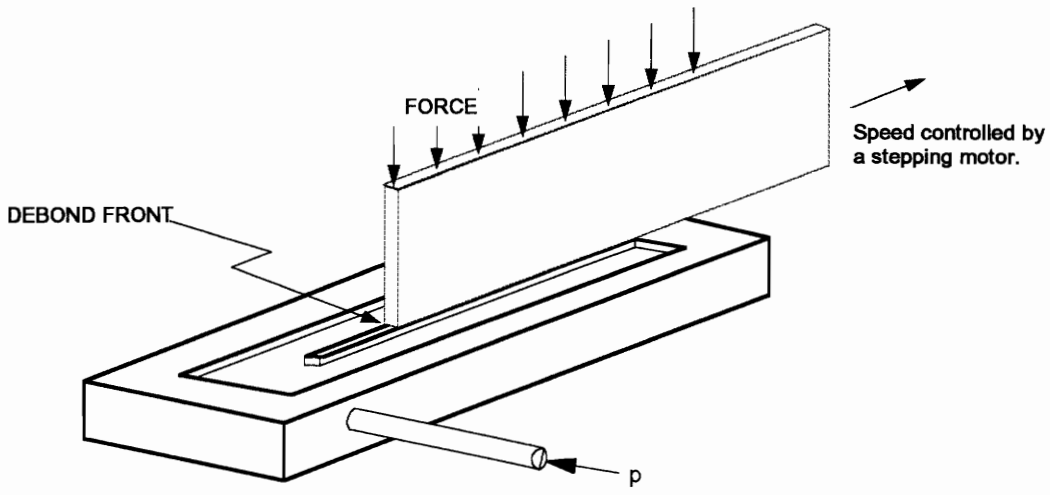

Figure D.2 Illustration of the control mechanism to simulate the debond rate.

Appendix D A Proposed Technique to Fabricate a Suspended Membrane for Film Adhesion Measurement

D.1 Introduction

Although blister tests have been used to measure the bond fracture strength of films and coatings, one of the most common challenges is the fabrication of specimens with suspended membrane as the initial debond where the pressure can be applied. Hinkley (1983) succeeded in fabricating a suspended polymer membrane on a silicon wafer and forming the initial debond for a standard blister test by using an etching solution of hydrofluoric acid (HF) and Nitric acid (HNO_3) mixture. Allen and Senturia (1988, 1989) used a photolighographic etching technique to fabricate island blister specimen for polyimide films on silicon wafer substrates. These etching techniques are routinely used in the electronic packaging industry for other applications. In some other industries such as the packaging industry, although the measurement of bond fracture strength between polymeric coatings and aluminum substrates is very important, there are no techniques to fabricate specimens with suspended membranes so the bond fracture strength of polymeric coatings on aluminum substrates can be measured using a membrane peeling test.

In this appendix, a procedure to fabricate specimens with suspended membrane for testing polymeric coatings to thin aluminum substrates will also be proposed.

D.2 Future Work to Measure the Bond Fracture Strength of Thin Polymeric Coatings on Aluminum Substrates

One of the most difficult problems encountered in testing this type of thin polymeric coatings on aluminum substrates using the blister tests is the fabrication of specimens with suspended membrane. A technique called "metal polishing" has been used to fabricate specimens with some success. Since the specimens are not yet tested, it is still unknown how well the specimens have been fabricated. In the following section, the fabrication of the specimens and the future testing plan will be described in details.

Figure D.1 illustrates the procedure to fabricate peninsula blister specimens of polymeric coatings on aluminum substrates.

(a) Cut the coated aluminum sheet into rectangular shape of desired size and use sandpaper to remove the protective coating on the side that will be polished.

(b) Cut a strip of adhesive tape (Scotch™ tape, or any other tape that does not leave adhesive on aluminum after peeling) into a U-shape to serve as a mask on the surface to be polished. This is to make sure the surface to be polished does not receive a protective coating.

(c) Apply lacquer (e.g., Microshield™ by Tolber) to the rest of the aluminum surface. This is the protective coating.

(d) Remove the adhesive tape to expose the surface to be polished.

(e) Immerse the aluminum sample in a sodium hydroxide (NaOH) solution (15%wt) for approximately 120 minutes for the thickness of the currently received samples or until all undesired aluminum is gone. Keep the beaker which contains NaOH solution in a bucket full of ice water. Since the NaOH-Al reaction is exothermic and spontaneous, the ice water keeps the reaction under control. (One may shorten the reaction time without using ice water. However, the polishing process needs to be

monitored at all time to prevent over polishing.) The solution needs to be stirred while the sample is being polished.

(f) Remove the sample and rinse it well. Remove the lacquer using acetone (optional). Mount the polished specimen on the blister fixture and bond the peninsula of the sample on the peninsula of the fixture using epoxy or Cyanoacrylate (Super Glue) adhesive. To reinforce the coatings, a layer of adhesive tape may be applied on the top of the sample.

It should be noted that other metal polishing solutions may be used to polish the aluminum. Two examples: (1) A solution of 70ml H_3PO_4, 3 HNO_3, 12ml acetic acid, and 15ml distilled water. (2) A solution of 25ml Sulfuric acid, 70ml Orthophosphoric acid, and 5ml Nitric acid. The advantages of using these two solutions are that the edges of the peninsula may be more defined and the reaction is easier to control due to the endothermic reactions.

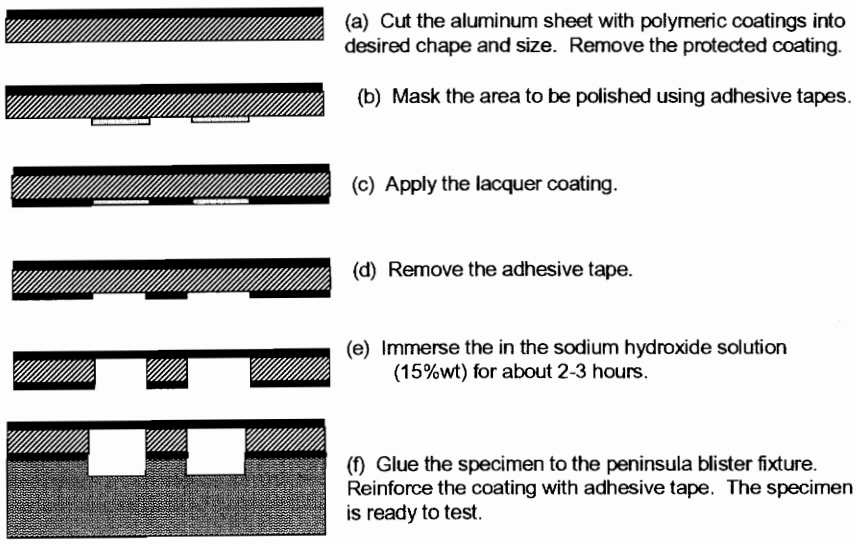

Figure E.1 Illustration of the procedure to fabricate the peninsula blister specimens of polymeric coatings on aluminum substrates.

Appendix E Detailed Description of the Experimental Apparatus and Testing Procedure of the Peninsula Blister Test

E.1 Experimental Apparatus

The experimental apparatus for the peninsula blister test should fulfill two major requirements: the capability for recording of the applied pressure and the blister volume during the loading (pressurization) and unloading (depressurization) process and the capability for recording of the debond length of specimens during the debonding process. The setup shown in Fig. E.1 consists of a pressure source, two mass flow meters, a control valve, a needle valve, a safety valve, a pressure transducer, a pressure/flow controller, a peninsula blister fixture, a video camera, a video cassette recorder, and a data acquisition system.

In the current study, the pressure source was a nitrogen gas tank. The pressure regulator on the nitrogen gas tank had a capacity of 138 kPa (20 psi). The peninsula blister fixture was the one shown in Fig. E.2 which was made of aluminum with various dimensional designs. Typically, the outer perimeter inside the groove of the fixture had a dimension of 113mm in length and 20.3mm in width and the peninsula has a dimension of 87mm in length and 1.6mm in width.

The flow rate was measured using a MKS 258C mass flow meter from MKS instruments, Inc (Andover, MA). The mass flow meter measures the mass flow rate of gas in a laminar flow. Upon entering the flow meter, the gas stream is divided into two parallel paths; the first is directed through a sensor tube, the second through a bypass tube. The mass flow rates are determined by measuring the heat required to maintain an elevated temperature profile along the laminar flow sensor tube. The mass flow rate in the sensor

tube is proportional to the voltage of the resistance heaters wound around the sensor tube necessary to maintain a designated temperature profile. The range of flows measurable with this mass flow meter is 0 to 10 standard cubic centimeters per minute. The accuracy of the flow rate is ± 0.8% of the full scale. The error of the pressure coefficient for the MKS 258C is 0.005% of reading per psi. The signal from the meter is sent out as a 0 to 5 volt DC output.

Pressure in the system was measured using either an MKS 122A absolute pressure transducer or an MKS 122 gauge pressure transducer. The MKS 122A has a maximum capacity of 666.42kPa (96.680 psi). The MKS 122 has a maximum capacity of 133.29 kPa (19.336 psi) capacity. In both types of pressure gauge, as the pressure of a gas is applied to one side of a diaphragm the deflection is detected by electrodes. The change in capacitance between the electrodes is then converted to 0-10 volt DC signal which is sent out to for further processing.

To control the gas flow, an MKS 248A electro-magnetic control valve was used. The valve seat of the MKS 248A control valve is lifted away from the flow orifice as current is supplied to the valve. The current was controlled from an MKS 250C pressure/flow controller.

The MKS 250C pressure/flow controller adjusts the MKS 248A control valve based on the set-point chosen by the user and the signal received by either the pressure transducer or the flow meter. The controller compares the output signal from one of the transducers with the desired set-point. If there is a difference, a signal is sent to the control valve to open or close the flow orifice to bring the measured variable close to the desired set point. In this manner the flow of gas is controlled to a set pressure or mass flow rate. One limitation of the MKS 250C controller is that the rear panel can only accept one input jack. Since one may need to control the flow based on pressure or mass flow rate, a switch was constructed so it allowed one to determine which transducer signal was to be sent to the controller. Also, the controller can only supply power to one

transducer at a time. A 15 VDC power source was constructed to supply power to the pressure transducer. A switching board with three 14-pin connectors for three transducers and a 9-pin connector for the controller was also constructed. The 15 VDC power source was wired to the two flow meters on this board, and the output signals were routed to a switch mounted on the front panel of the main box. Both transducer signals were also sent to the front panel where they could be easily accessed for further data processing.

In order to house the blister setup and the controller, a main box was constructed. The dimensions of the box are 20.25 x 16 x 15 inches. The front panel was divided into two sections as shown in Fig. E.3. The controller and output signal outlets were housed in the top section and the transducers, valves, and tubing were housed in the lower section for easy access and control.

To connect between various components, stainless steel tubing of 0.25" outer diameter and Swagelock connectors were used. It was found that copper tubing was easily deformed if too much force was applied to lock the Swagelok connectors and caused leaks at the connections. After replaced with stainless steel tubing, the leaking problems were solved.

The signals from the transducers were recorded using a Macintosh IIx computer (Apple Computer, Inc). An analog/digital (A/D) board, model NB-MIO-16X by National Instruments, Inc., was used to interface between the output of the transducers and the input of the computer. A computer program based on LabView (version 2.2, by National Instruments, Inc.) was used to coordinate the data-acquisition process Recorded data were then imported into a spreadsheet file for further analysis. Frequency analysis showed that the noise of the signals from the flow meter and pressure transducer was primarily random. To eliminate the noise, the signals were averaged at a specific number of readings in a specific time period. Typically, it was averaged at the rate of one thousand readings per 0.05 second. A video camera and video cassette recorder were used to record the images of the debonding process for further analysis.

After the setup was constructed, it was calibrated so the pressure/volume relationship in the blister fixture, connectors, and the tubing during the pressurization and depressurization could be determined. With this information, the blister volume was obtained by subtracting the volume in the blister fixture and tubing from the total gas volume passed through the flow meter. A typical pressure/volume curve is seen in Fig. E.4 and the pressure/volume relationship during the pressurization and depressurization process are:

$$\overline{V} = C_{FM1} p_g \quad \text{(for pressurization process)} \tag{E.1-1}$$

and

$$\overline{V} = C_{FM2} p_g \quad \text{(for depressurization process)} \tag{E.1-2}$$

where $C_{FM1} = 0.42154$ and $C_{FM2} = 0.42102$.

The units of the volume and pressure are liters and Pascals, respectively. It should be noted that whenever a new fixture is used or a new component is added, the calibration procedure should be properly repeated.

The volume of the blister can be calculated from the following equations,

for pressurization process

$$\overline{V}_b = \left(\int_0^t f_1 d\tau - C_{FM1} \times p_g \right) \frac{p_a}{p_g}, \qquad 0 \le t \le t_1; \tag{E.2-1}$$

and for pressurization process

$$\overline{V}_b = \left[\int_0^{t_1} f_1 d\tau + (C_{FM2} - C_{FM1}) p_g(t_1) - \int_{t_1}^t f_2 d\tau - C_{FM2} \times p_g \right] \frac{p_a}{p_g}, \qquad t_1 \le t \le t_2; \tag{E.2-2}$$

where $\overline{V}_b$ is the blister volume,

f_1 is the flow rate of the flow meter #1,

f_2 is the flow rate of the flow meter #2,

p_g is the gauge pressure in the blister,

p_a is the absolute pressure in the blister,

t_1 is the time of the initiation of the depressurization process,

t_2 is the time of the end of the test.

It should be noted that in the current calibration, the averaged deviation of the C_{FM1} and C_{FM2} are 0.3% and 0.75%, respectively. In the case when blister volume is 20% of the total input volume, which is typical in the results of Fig. 7.7, the error in the blister volume due to the calibration error can be 1.5% and 3.75%, respectively. The increase in the error suggests that the ratio between the blister volume and the input volume should be as large as possible. Possible ways are to increase the size of the specimen, decrease the inner diameter of the tubing, and decrease the depth of the groove in the blister fixture.

E.2 Testing Procedure

The peninsula blister specimens can be prepared either by bonding the film directly onto the peninsula and the perimeter of the fixture or by mounting the prefabricated sample with suspended film on the substrate. After the sample is mounted onto the fixture, the perimeter is then clamped to prevent debonding at the perimeter. In the current experiment, after the adhesive tape was bonded onto the peninsula blister fixture, the pressure regulator on the nitrogen gas tank was then set at a constant pressure and the control valve was opened to begin the loading process. Before the control valve was opened, the data acquisition program was run to take data as the initial flow rates and pressures. The control valve could be controlled in three different modes: flow rate control, pressure control, or manual control. The manual control mode was used in the study of the adhesive tape. When debonding occurred, a constant pressure was maintained by opening or closing the control valve. When the debond front reached a desired position, the pressure was then reduced until the gauge pressure in the blister fixture reached zero. During the loading/debond/unloading process, the pressure and flow

rate versus time were recorded at set time intervals by a program written using the LabView software package. The streams of data were then saved in a file for further analysis. The images of the debonding process were also recorded using a video camera, video cassette recorder and a timer so the debonding rate could be obtained.

Since the debond of the adhesive tape was time dependent and the debond might initiate before the pressure reached a desired value, a simple mechanism to control when and where the debond occurred was used. The controlling mechanism took advantage of a unique feature of the peninsula blister geometry - debond on the narrow peninsula. As seen in Fig. E.5, a rectangular plate (called the debond stopper) with the same thickness as the width of the peninsula width was used to slightly press the part of the adhesive tape that was still bonded on the peninsula of the fixture before the pressure reached the desired pressure, In this way, premature debond could be prevented. When the pressure reached a desired value, the debond stopper was then lifted to allow the debond to occur. When the debond front reached a specific position, the debond stopper was again pressed ahead the debond front to prevent further debond. With the use of the debond stopper, the debond length could be easily controlled even at a high pressure.

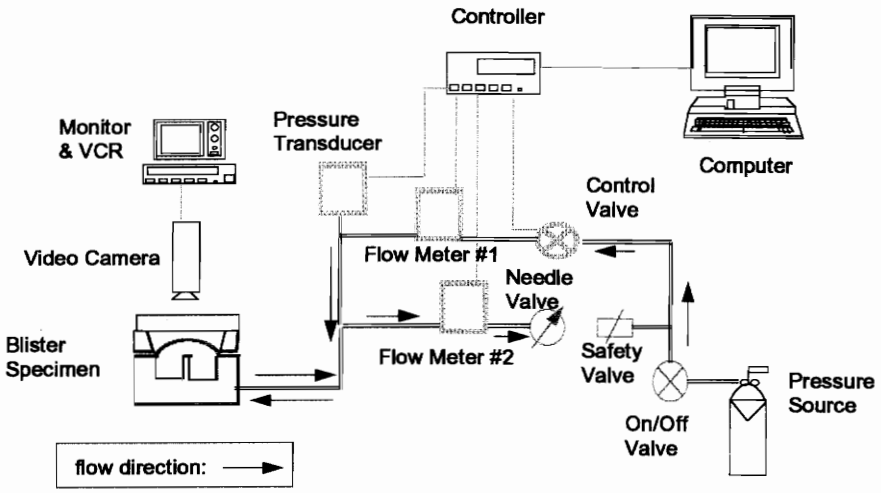

Figure E.1 Experimental setup of blister tests.

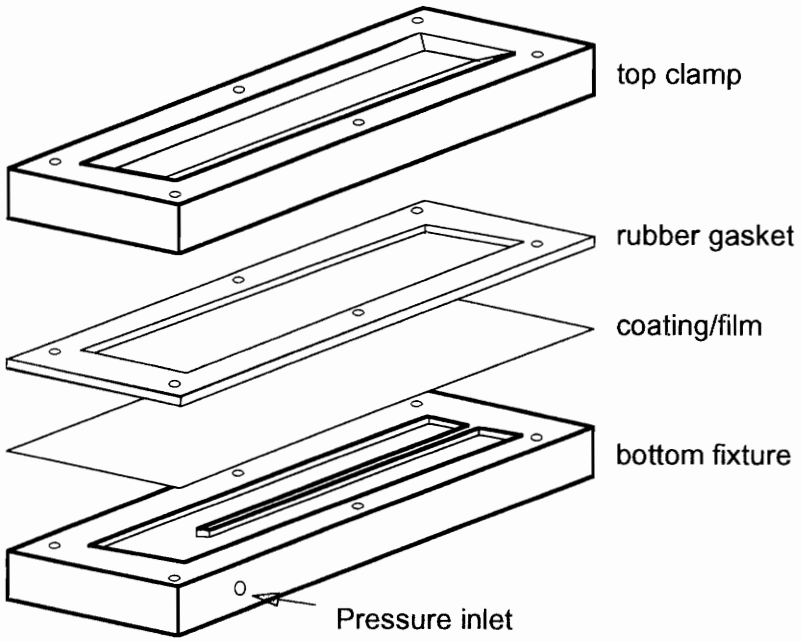

Figure E.2 Peninsula blister fixture with a specimen.

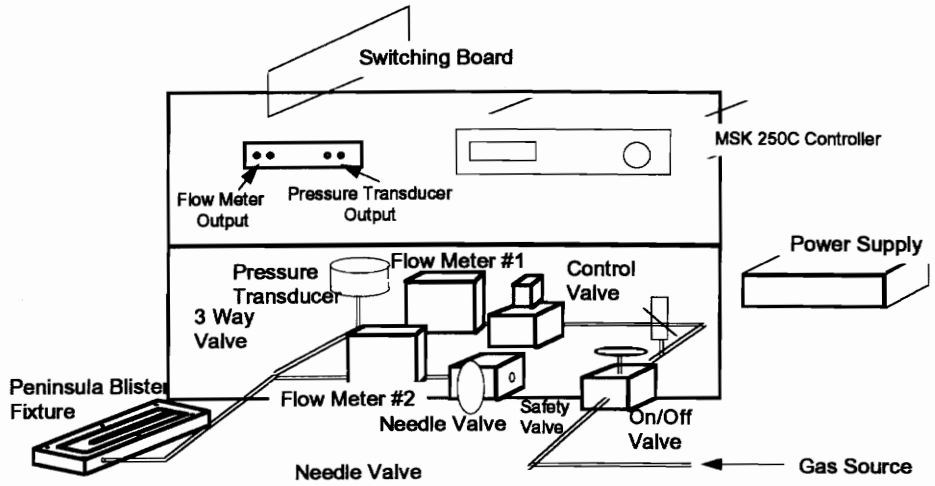

Figure E.3 The front panel of the instrument box for blister setup.

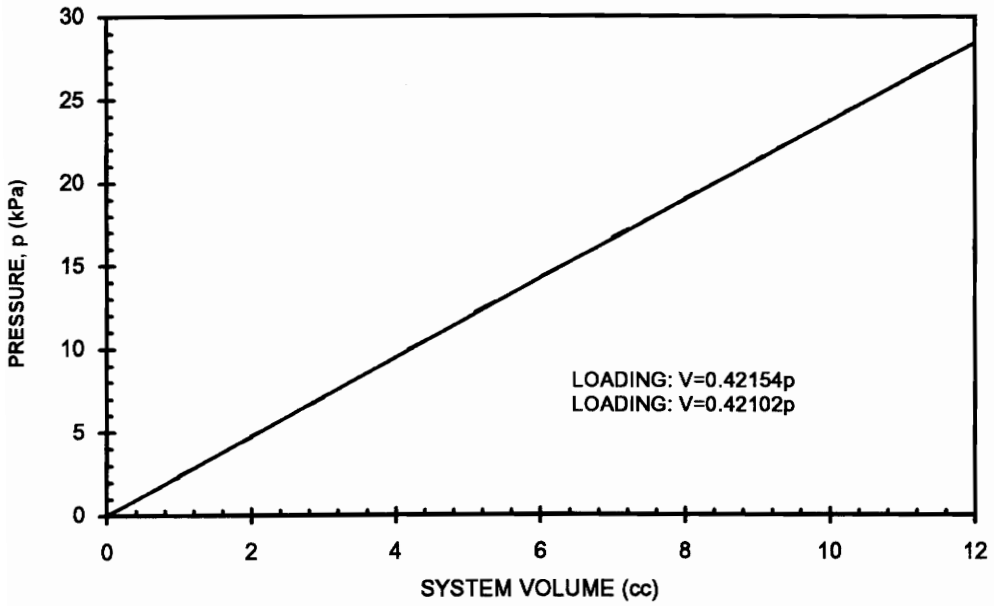

Figure E.4 Typical pressure/volume curves for blister setup calibration.

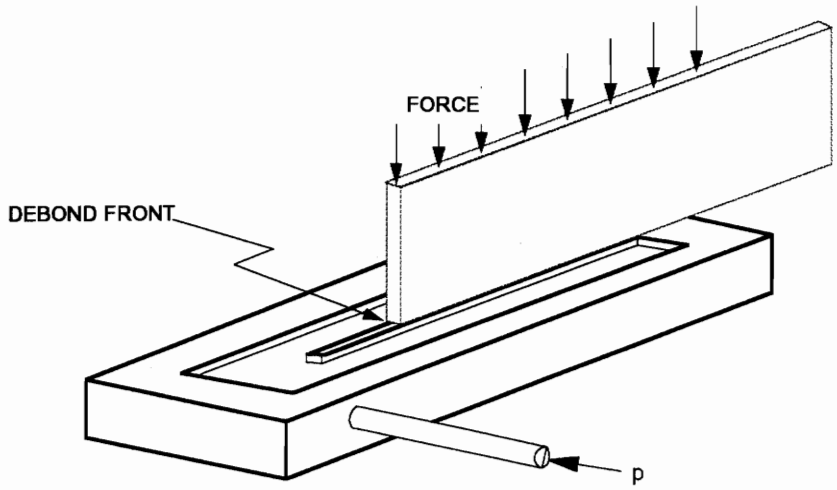

Figure E.5 Illustration of the debond stopping plate.

Appendix F Determination of Material Properties Using the Peninsula Blister Fixture

F.1 Introduction

The material properties of the films and coatings such as Young's modulus and prestress are needed for many applications. One conventional method of prestress measurement involves depositing the film of interest on a substrate and measuring the resulting substrate curvature (Hoffman, 1976). This method has been used to find the residual stress, however, the deflection of the substrate resulting from the film residual stress is very small, which makes the measurement difficult, especially on rigid substrates such as silica. Other conventional method to determine prestress and biaxial Young's modulus (defined as the uni-axial Young's modulus E divided by the quantity $(1-\nu)$, where ν is the in-plane Poisson's ratio of the film) involves the standard blister test (Beams, 1959). The solution used is based on the small deflection assumption and is applicable to very stiff films. With advances in micromachining technology, measuring material properties of films was made possible. Previous work in this field involves structures sensitive to buckling which can be used to measure compressive film stress (Guckel *et al.*, 1985, Borden, 1980, Lin, 1972), asymmetric structures which deform in response to tensile film stress (Mehregany *et al.*, 1987), and suspended membranes for measurement of Young's modulus and tensile stress (Bromley *et al.*, 1983, Allen *et al.*, 1987). More recently, Maseeh *et al.* (1988, 1989) used a standard blister test and a tensile test to obtain the prestress, Young's Modulus, and Poisson's ratio for thin polyimide films. The peninsula blister geometry was used to determine the Young's modulus of polyimide films by Bao (1992) who derived a relationship between the blister volume and applied pressure

for films without prestress and initial slack. In Bao's equation, the pressure is proportional to the third power of the blister volume.

In this appendix, a simple procedure is proposed to determine the Young's modulus and prestress in the membrane sample using the peninsula blister fixture.

F.2 Determining Young's Modulus and Prestress of the Membrane Specimen Using the Peninsula Blister Fixture

After the blister specimen is fully debonded and if it has not been subjected to grossly inelastic deformation, the material properties of the specimen can then be determined from the loading or unloading curves using the same specimen and blister fixture. The procedures are described below.

From Eq. (3.10), the relationship between B and C_1 is given by

$$c_1 = -\frac{3}{2}B. \tag{F.2}$$

Substituting the above equation into Eq. (3.8), we can obtain the following equation for the nondimensional prestress:

$$\sigma_0 = \frac{2}{3B} - \frac{3}{8}\frac{B^2}{1-\nu^2}. \tag{F.3}$$

From Eqs. (3.5-3) and (3.12-1), we have:

$$\sigma_0 = \frac{\bar{\sigma}_0}{E}\left(\frac{pR}{Eh}\right)^{-2/3}, \tag{F.4}$$

and

$$B = \frac{\bar{V}}{R^2 L}\left(\frac{pR}{Eh}\right)^{-1/3}, \tag{F.5}$$

and then substitute into Eq. (F.3) to obtain:

$$p = \left(\bar{\sigma}_0 + \frac{3}{8} \frac{\bar{V}^2}{R^4 L^2} E^* \right) \frac{3}{2} \frac{\bar{V} h}{R^3 L}. \tag{F.6}$$

where

$$E^* = \frac{E}{1 - \nu^2} \tag{F.7}$$

Theoretically, by performing a one-dimensional blister test and then curve fitting the pressure/volume data using Eq.(F.6), one may obtain $\bar{\sigma}_0$ and E^*. In practice, the one-dimensional blister test is not available and the peninsula blister test can be used instead as long as the length of the peninsula blister fixture is much larger than the width.

Although one does not obtain ν using the one-dimensional blister test, however, a reasonable estimation of Poisson's ratio should give a Young's modulus within reasonable accuracy. To support the previous argument, we may study the deviation of Young's modulus due to the error in estimating Poisson's ratio which is given by

$$\Delta E \approx 2\nu E^* \Delta\nu, \tag{F.8}$$

or by

$$\Delta E \approx \left(\frac{2\nu^2}{1 - \nu^2} \frac{\Delta\nu}{\nu} \right) E. \tag{F.9}$$

Typically, an error of 0.05 in estimating Poisson's ratio induces 3.3%, 4.8%, and 6.7% errors in Young's modulii for materials with Poisson's ratios of 0.3, 0.4 and 0.5, respectively. Since most metals have Poisson's ratios in the range 0.25 to 0.35 and polymers in the range 0.3 to 0.5, an error smaller than 0.05 in estimating the Poisson's ratio should be reasonable which would then result in a reasonable estimation of Young's modulus.

It should be noted that the technique described in this section is similar to that of Bao's (1992) except that the prestress is considered in the current study but not in Bao's.

References

Allen, M. G. and Senturia, S. D. (1988). "Analysis of Critical Debonding Pressures of Stressed Thin Film in the Blister Test", *Journal of Adhesion*, Vol. 25, pp. 303-315.

Allen, M. G., and Senturia, S. D. (1989). "Application of the Island Blister Test for Thin Film Adhesion Measurement", *Journal of Adhesion* , Vol. 9, pp. 219-231.

Allen, M. G., Mehregany, M., Howe, R. T., and Senturia, S. D. (1987). "Microfabricated Structures for the in-situ Measurement of Residual Stress, Young's Modulus, and Ultimate Strain in Thin Films", *Applied Physics letters*, Vol. 51, p. 241-243.

Anandarajah A. and Vardy, A.E. (1984). "Mode I and II Fracture of Adhesive Joints", *Journal of Strain Analysis*, Vol. 19, pp. 173-183.

Anderson, G. P., DeVries, K. L. and Williams, M. L. (1974). "Mixed Mode Stress Field Effect in Adhesive Fracture", *International Journal of Fracture*, Vol. 10, No. 4, pp.565-583.

Anderson G. P., Bennett, S. J., and DeVries, K. L. (1977). *Analysis and Testing of Adhesive Bonds*, Academic Press, New York.

Arah, C.O., McNamara, D.K., Hand, H.M., and Mecklenburg, M.F. (1989). "Techniques for Screening Adhesives for Structural Applications", *Journal of Adhesion Science and Technology*, Vol.3, pp. 261-269.

Aravas, N., Kim, K. S., and Loukis, M. J. (1989). "On the Mechanics of Adhesion Testing of Flexible Films", *Material Science and Engineering*, Vol. A107, pp. 159-168.

Bao, Y. (1992) *The Development of the Peninsula Blister Fracture Test for Adhesively Bonded Joints*, master thesis, Department of Engineering Science and Mechanics, Virginia Polytechnic Institute and State University, 1992.

Beams, J.W. (1959). "Mechanical Properties of Thin Films of Gold and Silver", in *Structure and Properties of Thin Films*, ed. C.A. Neugebauer, pp. 183-192.

Bikerman, J. J. (1957). "Theory of Peeling Through a Hookean Solid", *Journal Applied Physics*, Vol. 28, pp. 1484-1485.

Borden, P. G. (1980). "A Simple Technique for Determining the Stress at the Si/SiO_2 Interface", *Applied Physics Letters*, Vol. 36, pp. 829-831.

Breitling, S.M., Williams, M. L. and Colwell, R. (1978). "Adhesive Fracture of Bonded Plate or Membrane Strip", *Journal of Adhesion*, Vol. 9, pp. 141-144.

Brinson, H. L. (1990) *Adhesives and Sealants, Engineered Materials Handbook*, Vol. 3, H. F. Brinson, Technical Chairman, ASM International.

Brodland, G. W. (1986). "Nonlinear Deformation of Uniformly Loaded Circular Plates", *SM Archives*, Vol. 11, No. 4, pp. 219-256.

Broek, D. (1982) *Elementary Engineering Fracture Mechancis*, Martinus Nijhoff Publishers, The Hague.

Bromley, E. I., Randall, J. N., Flanders, D. C., and Mountain, R. W. (1983). "A Technique for the Determination of Stress in Thin Films", *Journal of Vaccum Science and Technology Bulletin*, Vol.1, pp. 1364-1366.

Brussat, T.R. and Chiu, S.T. (1978). "Fatigue Crack Growth of Bondline Cracks in Structural Bonded Joints", *Journal of Enginnering Materials and Technology, (Trans. ASME)*, Vol. 100, pp. 39-45.

Brussat, T.R. and Chiu, S.T., and Mostovoy, S. (1977). "Fracture Mechanics for Structural Adhesive Bonds", AFNL-TR-77-163, Air Force Materials Laboratory, Wright-Patterson AFB, Ohio.

Chai, H. (1988). "Shear Fracture", *International Journal of Fracture*, Vol. 37, pp. 137-159.

Chai, H. and Mall, S. (1988). "Design Aspect of the End-Notched Adhesive Joint Specimen", *International Journal of Fracture*, Vol. 36, pp. R3-R6.

Chang, Y.S., Lai, Y.H. and Dillard, D.A. (1987). "The Constrained Blister - A Nearly Constant Strain Energy Release Rate Test for Adhesives", CASS/ESM-87-8, Virginia Polytechnic Institute, Blacksburg, Virginia, U.S.A. Sept.

Chang, Y.S. Lai, Y.H. and Dillard, D.A. (1989). "The Constrained Blister - A Nearly Constant Strain Energy Release Rate Test for Adhesives", *Journal of Adhesion*, Vol. 27, pp. 197-221.

Chang M.D., DeVries, K.L., and Williams, M.L. (1972). "The Effects of Plasticity in Adheisve Fracture", *Journal of Adhesion*, Vol. 4, pp. 221-231.

Charalambides, P.G., Lund, J., Evans, A.G., and McMeeking, R.M. (1989). "A Test Specimen for Determining the Fracture Resistance of Bimaterial Interfaces", *Journal of Applied Mechanics, (Trans. ASME)*, Vol. 56, pp. 77-82.

Chen, W. T. and Flavin, T. F. (1972). "Mechanics of Film Adhesion: Elastic and Elastic-Plastic Behavior", *I.B.M. Journal of Research and Development*, Vol. 16, pp. 203-213.

Cho, K. and Gent, A.N. (1985)., *International Journal of Fracture*, Vol. 28, pp. 239-244.

Chu, Y. Z. and During, C. J. (1992). "Application of the Blister Test to the Study of Polymer-Polymer Adhesion", *Journal of Applied Polymer Science*, Vol. 45, pp.1151-1164.

Crocombe, A. D. and Adams, R. D. (1981). "Peel Analysis Using the Finite Element Method", *Journal of Adhesion*, Vol. 12, pp.127-139.

Crocombe, A. D. and Adams, R. D. (1982). "An Elasto-Plastic Investigation of the Peel Test", *Journal of Adhesion*, Vol. 13, pp. 241-267.

Dannenberg, H. (1961). "Measurement of Adhesion by a Blister Method", *Journal of Applied Polymer Science*. Vol. 5, pp. 125-134.

Dattaguru, B., Everett, R.A., Jr., Whitcomb, and J.D., Johnson, W.S. (1984). "Geometrically Nonlinear Analysis of Adhesively Bonded Joints", *Journal of Engineering Materials and Technology*, Vol. 106, pp. 59-65.

Dillard, D. A. and Bao, Y. (1991). "The Peninsula Blister Test: A High and Constant Strain energy Release Rate Fracture Specimen for Adhesives", *Journal of Adhesion*, Vol. 3, pp. 253-271.

Dillard, D. A., and Chang, Y.S. (1987). "The Constrained Blister - A Novel Constant Strain Energy Release Rate Test for Adhesives", Virginia Polytechnic Institute Report #VPI-E-87-24, Blacksburg, VA.

Dillard, D. A., Lai, Y. H., Chang, Y. S., Corson, T., and Bao Y. (1990). "Alternate Blister Geometries for Measuring the Fracture Toughness of Adhesive Bonds", Proceedings of the 1990 Society for Experimental Mechanics Conference on Experimental Mechanics, Albuquerque, June 1990, pp. 575-582.

Dillard, D. A., Liechti, K. M., Lefebvre, D. R., Lin, C., Thornton, J. S., and Brinson, H.F. (1988) in *Adhesively Bonded Joints: Testing, Analysis and Design*, STP 981, Johnson, W. S., Ed., American Society for Testing and Materials, p. 83.

Dillard, D. A., Wang, J. Z., and Parvatareddy, H. (1993). "A Simple Constant Strain Energy Release Rate Loading Method for Double Cantilever Beam Specimens", *Journal of Adhesion*, Vol. 41, pp. 35-50.

Edde, F. and Verreman, Y. (1992). "On the Fracture Parameter in a Clamped Cracked Lap Shear Adhesive Joint", *Internation Journal of Adhesion and Adhesives*, Vol. 12, No. 1, pp. 43-48.

Everett, R.A. and Johnson, W.S. (1985). "Repeatability of Mixed-Mode Adhesive Bonding", in *Delamination and Debonding of Materials*, W.S. Johnson, Ed., STP 876, American Society for Testing and Materials, pp. 267-281.

Farris, R. J. and Goldfarb, J. (1992). "An Experimental Partitioning of the Energy Expended During Peel Testing", Proceeding of International Symposium on Adhesion Measurement of Films and Coatings, Boston.

Fernando M. and Kinloch, A. J. (1990). "Use of the 'Inverted-Blister' Test to Study the Adhesion of Photopolymers", *International Journal of Adhesion and Adhesives*, Vol. 10, No. 2, pp. 69-76.

Fleck, N. A., Hutchinson, J. W., and Suo, Z. (1991). "Crack Path Selection in a Brittle Adhesive Layer", *International Journal of Solids and Structures*, Vol. 27, No. 13, pp. 1683-1703.

Gardon, J. L. (1963). "Peel Adhesion. II. A theoretical Analysis", *Journal of Applied Polymer Science*, Vol. 7, pp.643-665.

Gent, A.N. (1987). "New and Improved Tests for Adhesion", *Journal of Adhesion*, Vol. 23, pp. 115-122.

Gent, A. N. and Hamed, G. R. (1975a). "Peel Mechanics", *Journal of Adhesion*, Vol. 7, pp .91-95.

Gent, A.N. and Hamed, G.R. (1977). "Peel Mechanics for an Elastic-Plalstic Adherend", *Journal of Applied Polymier Science*, Vol.21, pp. 2817-2831.

Gent, A.N. and Kaang, S.Y. (1986). "Pull-Off Forces for Adhesive Tapes", *Journal of Applied Polymier Science*, Vol. 32, pp. 4689-4700.

Gent, A. N. and Lewandowski, L. H. (1987). "Blow-off Pressures for Adhering Layers", *Journal of Applied Polymer Science*, Vol. 33, pp. 1567-1577.

Goland, M., and Reissner, E. (1944). "The Stresses in Cemented Joints", *Journal of Applied Mechanics*, Vol.66, pp. A-17 - A-27.

Goldfarb, J. L. and Farris, R. J. (1991). "Calorimetric Measurements of The Heat Generated by The Peel Adhesion Test", *Journal of Adhesion*, Vol. 35, pp. 233-244.

Griffith, A. A. (1921), Philosophical Transaction of the Royal Society. London A221, 163-197.

Griffith, A. A. (1924), Proceeding of the 1st International Congress of Applied Mechanics, Biezeno and Burgers Ed., Waltman Publishing Corp. pp. 55-63.

Guckel, H., Randazzo, T, and Burns, D.W. (1985). "A Simple Technique for the Determination of Mechanical Strain in Thin Films with Application to Polysilicon", *Journal of Applied Physics*, Vol. 57, pp. 1671-1675.

Hibbitt, Carlsson and Sorenson, Inc., ABAQUS User Manual, Version,4-7-1, Providence, RI.

Hinkley, J. A. (1983). "A Blister Test for Adhesion of Polymer Films to SiO_2", *Journal of Adhesion*, Vol.16, pp. 115-126.

Hoffman, R.W. (1976). "Mechanical Properties of Nonmetallic Thin Films", in *Physics of Nonmetallic Thin Films*, ed. C.H.S. Dupey and A. Cachard, NATO Advanced Study Institutes, vol, B-14, Plenum, pp. 273-353.

Hohnson, W.S. and Mall, S. (1985). "A Fracture Mechanics Approach for Designing Adhesively Bonded Joints", in *Delamination and Debonding of Materials*, W.S. Johnson, Ed., STP 876 American Society for Testing and Materials, pp. 189-199.

Hutchinson, J. W. and Sue, Z. (1990). "Mixed Mode Cracking in Layered Materials", in *Advances in Applied Mechanics*, Vol. 29, J. W. Hutchinson and T. Y. Wu, Eds, (Acadmic Press, San Diego, CA) pp. 64-191.

Jensen, H. M. (1991). "The Blister Test for Interface Toughness Measurement", *Engineering Fracture Mechanics*, Vol. 40, No. 3, pp. 475-486.

Jeong, Hyo-Soo, Chu, Y. Z., During, C. J., and White, R. C. (1992). "Adhesion Study of Polyimide to Si Surfaces", *Surface and Interface Analysis*, Vol. 18, pp. 289-293.

Jiang, K. R. and Penn, L. S. (1990)"Use of the Blister Test to Study the Adhesion of Brittle Materials", *Journal of Adhesion*, Vol. 32, No. 4, pp. 203-216.

Johnson, W.S. (1987). "Stress Analysis of the Cracked Lap Shear Specimen: An ASTM Round Robin", *ASTM Journal of Testing and Evaluation*, Vol. 15, pp. 303-324.

Jouwersma C. (1960). "On the Theory of Peeling", *Journal of Polymer Science*, Vol. 45, p.253.

Kaeble, D. H. (1959). "Theory and Analysis of Peel Adhesions: Mechanisms and Mechanics", *Transaction of the Society of Rheology*, Vol.3, p. 161.

Kaeble, D. H. (1960). "Theory and Analysis of Peel Adhesions: Bond Stresses and Distributions", *Transactions of Society of Rheology*, Vol.4, pp. 45-73.

Kao, R. and Perrone, N. (1971). "Large Deflections of Axisymmetric Circular Membranes", *International Journal of Solids and Structures*, Vol. 7, pp. 1601-1612.

Kendall, K. (1973). "The Shapes of Peeling Solid Films", *Journal of Adhesion*, Vol. 5, pp. 105-117.

Kim, J., Kim, K. S., and Kim, Y. H. (1989). "Mechanical Effects in Peel Adhsion Test", *Journal of Adhesion Science and Technology*, Vol.3, No.3, pp. 175-187.

Kim, K. S., and Aravas, N. (1988a). "Elastoplastic Analysis of the Peel Test", *International Journal of Solids and Structures*, Vol. 24, No. 4, pp. 417-435.

Kim, K. S., and Kim, J. (1988b). "Elasto-Plastic Analysis of the Peel Test for Thin Film Adhesion", *Journal of Engineering Material and Technology*, Vol. 110, pp. 266-273.

Lai, Y. H. and Dillard, D. A. (1990a). "An Elementary Plate Theory Prediction for Strain Energy Release Rate of the Constrained Blister Test", *Journal of Adhesion*, Vol. 31, pp. 177-189.

Lai, Y. H., and Dillard, D. A. (1990b). "Numerical Analysis of the Constrained Blister Test", *Journal of Adhesion*, Vol. 33, pp. 63-74.

Lai, Y. H., and Dillard, D. A. (1994). "A Study of Fracture Efficiency Parameter of Blister Tests for Films and Coatings", *Journal of Adhesion Science and Technology*, (in Press).

Lai, Y.H. and Dillard, D.A. (1993). "Test Efficiency, A Simple Parameter for Comparing Fracture Tests for Adhesion Measurement", *Adhesives in Structural Bonding, 1993 International Symposium on Optical Applied Science and Engineering*, chaired by Kenneth M. Liechti, San Diego, CA, July, 1993.

Landau L.D. and Lifshitz, E.M. (1970), *Theory of Elasticity*, Pergamon, New York, pp. 61-62.

Liechti, K. M. and Liang, Y-M (1992). "The Interfacial Fracture Characteristics of Bimaterial and Sandwich Bliter Specimens", *International Journal of Fracture*, Vol. 55, pp. 95-114.

Lin, C. and Liechti, K.M. (1987). "Similarity Concepts in the Fatigue Fractureof Adhesively Bonded Joints", *Journal of Adhesion*, Vol. 21, pp. 1-24.

Lin, S.C.H. and Pugacz-Muraszkiewicz, I. (1972). "Local Stress Measurement in Thin Thermal SiO2 Films on Silicon Substrates", *Journal of Applied Physics*, Vol. 43, p.119.

Lotfipour, M., Packham, D. E., and Turner, D., M. (1991). "Interfacial Layers and Adhesion in the Moulding of Nitril Rubber", *Surface and Interface Analysis*, Vol. 17, pp. 516-518.

Mai Y.W. and Vipond, A.S. (1978). "On the Opening and Edge-Sliding Fracture Toughness of Aluminum-Epoxy Adhesive Joints", *Journal of Materials Science*, Vol.13, pp. 2290-2284.

Mall, S., and Johnson, W.S. (1986). "Characterization of Mode I and Mixed Mode Failure of Adhesive Bonds Between Composite Adherends", *Composite Materials: Testing and Design* (Seventh Conference), ASTM STP 893, J.M., Whitney, ed., American Society for Testing and Materials, Philadelphia, pp. 322-334.

Mall, S., Johnson, W.S., and Everett, R.A. Jr. (1984). "Cyclic Debonding of Adhesively Bonded Composites", in *Adhesive Joints: Their Formation Characteristics and Testing*, K.L. Mittal, Ed., Plenum Publishing, pp. 639-658.

Mall, S., Rezaizadeh, M.A., and Curumurthy, R. (1987). "Interaction of Mixed-Mode Loading on Cyclic Debonding in Adhesively Bonded Composite Joints", *Journal of Enginnering Materials and Technology*, (Trans. ASME), Vol. 109, pp. 17-21.

Mall, S. and Yun, K.T. (1987). "Effect of Adhesive Ductility on Cyclic Debond Mechanicsms in Composite to Compoiste Bonded Joints", *Journal of Adhesion*, Vol.23, pp. 215-231.

Mangalgiri, P.D., Johnson, W.S., and Everett R.A., Jr (1987). " Effect of Adherend Thickness and Mixed-Mode Loading on Debond Growth in Adhesively Bonded COmposite Joints", *Journal of Adhesion*, Vol. 23, pp. 263-288.

Maseeh, F. and Senturia, S. D. (1989). "Elastic Properties of Thin Polyimide Films", in Proceedings of the Third Annual Conference on Polyimides, Ellenville, New York, 1988, pp. 575-584.

Maseeh, F., Schmidt, M. A. Allen, M., and Senturia, S. D. (1988). "Calibrated Measurements of Elastic Limit, Modulus, and the Residual Stress of Thin Films Using Micromachined Suspended Structures", Proceedings of the IEEE Solid State Sensors Workshop, Hilton Head, S. C., pp. 84-87.

McMillan, J.C. (1981). "Durability Test Methods for Aerospace Bonding", *Developments in Adhesives*, 2, A.J. Kinloch Ed., Applied Science Publishers, pp. 243-278.

Mehregany, M., Howe, R. R., and Senturia, S. D. (1987). "Novel Microstructures for the Measurement of Mechanical Properties of Thin Films", *Journal of Applied Physics*, Vol. 62, n. 9, pp. 3579-3584.

Mittal, K. L. (1978). "Adhesion Measurement: Recent Progress, Unsolved Problems, and Prospects", *Adhsion Measurement of Thin Films, Thick Films and Bulk Coatings, ASTM STP 640*, K. L. Mittal, Ed. , ASTM, pp. 5-17.

Mossakovskii, V.I. and Rybka, M.R. (1964). "Generalization of the Griffith-Sneddon Criterion for the Case of a Nonhomogeneous Body", *PPM*, Vol.28, pp. 1061-1069.

Mostovoy, S. and Ripling, E. J. (1975). Final Report, "Fracturing Characteristics of Adhesive Joints", Contract No. N00019-74-0274, Material Lab., Glenwood, Illinois.

Moussiaux, E., Brinson, H.F., and Cardon, A.H. (1987). "Bending of a Bonded Beam as a Test Method for Adhesive Properties", Report CAS/ESM-87-2, Virginia Polytechnic Institute and State University, Center for Adheion Science.

Napolitano, J., Chudnovsky, A., and Moet, A. (1988). " The Constrained Blister Test for the Energy of Interfacial Adhesion", *Journal of Adhesion Science and Technology*, Vol. 2, pp. 311-323.

Nicholson, D. W. (1977). "Peel Mechanics with Large Bending", *International Journal of Fracture*, Vol. 13, pp. 279-287.

Osborne P.W. (1966). "Stead State Fracture Device", *Review of Scientific Instruments*, Vol.37, p. 664.

Outwater, J.O. and Gerry, D.J. (1969). "On the Fracture Energy, Rehealing Velocity and Refracture Energy of Epoxy Resin", *Journal of Adheison*, Vol. 1, pp. 290-295.

Perrone, N. and Kao, R. (1971). "A General Nonlinear Relaxation Iteration Technique for Solving Nonlinear Problems in Mechanics", *Journal of Applied Mechanics*, Vol.38, pp. 172-178.

Rice, J. R. (1967). "A Path Independent Integral and Approximate Analysis of Strain Concentrations by Notches and Cracks", *Journal of Applied Mechanics*, Vol. 34, pp. 379-386.

Ripling, E.J., Crosley, P.B., and Johnson, W.S. (1988), A Comparison of Pure Mode I and Mixed-Mde I-III Cracking of an Adhesive Conatining an Open Knit Cloth Carrier", in *Adhesively Bonded Joints: Testing, Analysis, and Design*, W.S. Johnson, Ed., STP 981, American Society for Testing and Materials, pp. 163-182.

Ripling, E.J., Mostovoy, S., and Corten, H.T. (1971). "Fracture Mechnanics: A Tool for Evaluating Structural Adhesives", *Journal of Adhesion*, Vol. 3, pp. 107-123.

Russell A.J. and Street, K.N. (1982). "Factors Affecting the Interlaminar Fracture Energy of Graphite/Epoxy Laminates", in *Progress in the Science and Engineering of Composites*, T. Hayashi, K.Kawata, and S. Unekawa, Ed., Pergamon Publishing, pp. 279-286.

Russell A.J. and Street, K.N. (1985). "Moisture and Temperature Effects on the Mixed Mode Delamination Fracture of Unidirectional Graphite/Epoxy", in *Delamination and Debonding of Materials*, W.S. Johnson, Ed., STP 876, Smerican Society for Testing and Materials, pp. 349-370.

Russell A.J. and Street, K.N. (1987). "The Effect of Matrix Toughness on Delamination: Static and Fatique Fracture of Unidirectional Graphite/Epoxy in Toughnened Composites, in *Toughened Composites*, N.J. Johnston, Ed., STP 937, American Society for Testing and Materials, pp. 275-294.

Saubestre, E. B., Durney, L. J., Haidu, J. and Bastenbeck, E. (1965). "The Adhesion of Electrodeposits to Plastics", *Plating*, Vol. 52, p.982-1000.

Schmueser, D.W. and Johnson, N.L. (1990). "Effect of Bondline Thickness on Mixed-Mode Debonding of Adhesive Joints to Electroprimed Steel Surfaces", *Journal of Adhesion*, Vol. 32, pp. 171-191.

Sears, F. W., Zemansky, M. W., and Young, H. D. (1976), *University Physics.* Addison Wesley Publishing Company, Inc.

Spies G. J. (1953). "The Peeling Test on Redux Bonded Joints", *Journal of Aircraft Engineering*, Vol. 25, pp. 64-70.

Suo, Z. and Hutchinson, J. W. (1990). "Interface Crack Between Two Elastic Layers", *International Journal of Fracture*, Vol. 43, pp. 1-18.

Suo, Z. and Hutchinson, J. W. (1989). "Sandwich Test Specimens for Measuring Interface Crack Toughness", *Materials Science and Engineering*, Vol. A107, pp. 135-143.

Thouless, M. D. and Jensen, H. M. (1992). "Elastic Fracture Mechanics of the Peel-Test Geometry", *Journal of Adhesion*, Vol. 38, pp. 185-197.

Turvey, G. J. (1978). "Large Delection of Tapered Annular Plates by Dynamic Relaxation", *Journal of the Engineering Mechanics Division*, ASCE, Vol. 104, EM2, pp. 351-366.

Updike, D. P. (1976). "Effect of Adhesive Layer Elasticity on the Fracture Mechanics of a Blister Test Specimen", *International Journal of Fracture*, Vol. 12, pp. 815-827.

Wang, J.-S. and Suo, Z (1990). "Experimental Determination of Interfacial Toughness Curves Using Brazil-Nut-Sanwiches", *Acta. Metallic Materials*, Vol.38, No.7, pp. 1279-1290.

Weissberg, V. and Arcan, M (1992). "Invariability of Singular Stress Fields in Adhesive Bonded Joints", International Journal of Fracture, Vol. 56, pp.52-83.

Williams, M. L. (1955). "Large Deflection Analysis for a Plate Strip Subjected to Normal Pressure and Heating", *Journal of Applied Mechanics*, Vol. 22, No. 4, pp. 458-464.

Williams, M. L. (1958). "Further Large Deflection Analysis for a Plate Strip Subjected to Normal Pressure and Heating", *Journal of Applied Mechanics*, Vol. 25, No. 2, pp. 251-258.

Williams, M. L. (1970). "The Fracture Threshold for an Adhesive Interlayer", *Journal of Applied Polymer Science*, Vol. 14, pp. 1121-1126.

Williams, M. L. (1972). "The Relation of Continuum Mechanics to Adhesive Fracture", *Journal of Adhesion*, Vol. 4, pp. 307-332.

Williams M. L. (1969). "The Continuum Interpretation for Fracture and Adhesion", *Journal of Applied Polymer Science*, Vol. 13, pp. 29-40.

Wolfram S. (1993), Mathematica, version 2.2.

Yurenka, S. (1962). "Peeling Testing of Adhesive Bonded Metal", *Journal of Applied Polymer Science*, Vol. 6, pp.136-144.

Zywicz E. and Parks D.M. (1989). "Elastic Yield Zone Around an Interfacial Crack Tip", *Journal of Applied Mechanics*, Vol. 56, pp. 577-584.

Vita

Yeh-Hung Lai

Yeh-Hung Lai was born in Taichung, Taiwan on March 3, 1962. He received his general education, 1st through 12th grade, in Taichung, Taiwan. After he graduated from the First Senior High School of Taichung, he attended National Cheng Kung University in Tainan. He obtained a B.S. degree in Civil Engineering in 1984. He served as a civil engineering officer in the R.O.C. army for two years. In 1989, with Dr. David Dillard as advisor, he obtained his M. S. degree in Engineering Mechanics and began his doctoral study at Virginia Polytechnic Institute and State University. His current research interests are in the areas of adhesion science and technology, especially in characterizing the mechanical behavior of adhesively bonded joints using fracture mechanics, finite element method, viscoelasticity, and experimental mechanics.